SYNTHESIS AND BIOLOGICAL EVALUATION OF AURISTATIN-F RECOMBINANT ANTIBODY-DRUG CONJUGATES FOR CANCER THERAPY

Dissertation presented for the degree of Master of Science in the Department of Chemistry, University of Cape Town

By

Allan Martin Huysamen

Supervisors: Professor Roger Hunter &

Professor Stefan Barth

Submitted in December 2019

University of Cape Town, Faculty of Science

Department of Chemistry

Rondebosch, 7700

South Africa

Declaration

I, **Allan Martin Huysamen**, declare the work presented in this thesis my own. I know the meaning of plagiarism and have properly acknowledged ideas and findings which were not my own. I grant the University of Cape Town free licence to reproduce either all or part of the contents in any manner.

Signed: Signed by candidate Date: 12/12/2019

Acknowledgements

To my supervisors, Professor Roger Hunter and Professor Stefan Barth, I thank you for your guidance and teaching in this expedition into the unknown. I appreciate the passion and drive you both share and the opportunities for growth you have provided me with.

Many thanks to Dr Fleury Augustin Nsole Biteghe and Ms Neelakshi Mungra for undertaking the biotechnology aspect of this research. I have gained invaluable knowledge through this collaboration, which has stimulated my interest in working at the interface of chemistry and medical biotechnology.

I extend my greatest appreciation to the Hunter academic group for creating a laboratory environment that is inclusive, enjoyable and focused. Special thanks to Olaolu Fadeyi for showing me the ropes when I arrived in the lab and for being by my side and offering support along the journey. I would also like to thank my MSc colleagues and the rest of the UCT Chemistry department for their contribution to making the department a constructive space and one which has been a pleasure to conduct research in.

Finally, I would like to thank my close friends and family for providing support and for ensuring I did not become completely engulfed in in the research process!

Abstract

This study serves as a contribution to the emerging field of antibody-drug conjugate (ADC) therapeutics, in which novel ADCs were generated and biologically evaluated for therapeutic potential and specificity towards cancer cells. SNAP-tag site-directed conjugation was employed in order to overcome the current challenges of heterogeneous ADC combination products resulting from standard conjugation methods.

The SNAP-tag fusion proteins were generated using recombinant DNA technology, and incorporated antibody single-chain variable fragments (scFvs) exhibiting specificity towards the epidermal growth factor receptor (EGFR), chondroitin sulfate proteoglycan receptor (CSPG4) and CD44 receptors more highly expressed in various cancer types. The design and successful synthesis of two BG-linkers was followed by coupling to auristatin-F, a powerful microtubule poison, using both Cu(I)-catalysed cycloaddition and amide coupling chemistry. The BG-linkers each incorporated a non-cleavable polyethylene glycol spacer, one of which included a dansyl fluorescent tag in order to aid in purification and characterisation. Ultimately, this study succeeded in producing two novel BG-modified ADC-precursors and various ADCs by virtue of SNAP-tag conjugation, three of which exhibited therapeutic potential following *in vitro* cytotoxicity assays.

Cytotoxicity assays were undertaken by treating A431, SK-Mel-28, MDA-MB468, Hs578T and A2058 cell lines with ADCs generated from various scFv-SNAP fusion proteins, in which selectivity towards target receptor positive cell lines was demonstrated. Quantification of the efficacy of generated ADCs was afforded by IC_{50} values, resulting from dose-response curves, which ranged from 44 nM – 180 nM.

Collectively, insights were gained into the subtleties governing the interface of molecular and macromolecular chemistry that will facilitate further research into the development of ADC cancer therapeutics.

Table of Contents

List of Figures

List of Schemes

List of Abbreviations

4-HMBA	4-Hydroxymethylbenzoic acid
ACN	Acetonitrile
ADC	Antibody-drug conjugate
AGT	O^6-Alkylguanine-DNA alkyltransferase
ALL	Acute lymphoblastic leukemia
ATP	Adenosine triphosphate
BCE	Before common era
BG	O^6-Benzylguanine
Boc	*tert*-Butyloxycarbonyl
Boc_2O	Di-*tert*-butyl decarbonate
CDK	Cyclin-dependant kinase
CSPG4	Chondroitin sulfate proteoglycan 4
CTLA-4	Cytotoxic T-lymphocyte–associated antigen 4
CuAAC	Copper(I)-catalysed azide-alkyne cycloaddition
DAR	Drug-antibody ratio
Dansyl	5-(Dimethylamino)naphthalene-1-sulfonyl
DCC	Dicyclohexylcarbodiimide
DCM	Dichloromethane
DCU	Dicyclohexylurea
DIAD	Diisopropyl azodicarboxylate
DIPEA	*N,N'*-Diisopropylethylamine
DMAP	Dimethylaminopyridine
DMF	Dimethylformamide
DMSO	Dimethyl sulfoxide
DNA	Deoxyribonucleic acid
EDC	1-Ethyl-3-(3-dimethylaminopropyl)carbodiimide
EGFR	Epidermal growth factor receptor
ERK	Extracellular signal-regulated kinase
ESI	Electrospray ionisation

EtOAc	Ethyl acetate
Fab	Fragment antigen-binding domain
Fc	Fragment crystallisable domain
G_0	Quiescent phase of the cell cycle
G_1	First gap phase of the cell cycle
G_2	Second gap phase of the cell cycle
GFP	Green fluorescent protein
GTP	Guanosine triphosphate
HOBt	Hydroxybenzotriazole
HPLC	High-performance liquid chromatography
HRMS	High-resolution mass spectrometry
IMAC	Immobalised metal affinity chromatogtaphy
IR	Infrared
kDa	Kilodaltons
LC-MS	Liquid chromatography - mass spectrometry
M	Mitotic phase of the cell cycle
mAb	Monoclonal antibody
MAPK	Mitogen-activated protein kinase
MDM2	Murine double minute 2
MEK	MAPK/ERK kinase
MeOH	Methanol
MMAE	Monomethyl auristatin-E
MMAF	Monomethyl auristatin-F
MS	Mass spectrometry
MWCO	Molecular weight cut-off
NHS	*N*-Hydroxysuccinimide
NMR	Nuclear magnetic resonance
ORF	Open reading frame
PABC	*p*-Aminobenzyloxycarbonyl
Pd/C	Palladium-on-carbon

PDT	Photodynamic therapy
PEG	Polyethylene glycol
PIT	Photoimmunotherapy
ROS	Reactive oxygen species
S	DNA synthesis phase of the cell cycle
scFv	Single-chain variable fragment
SDS	Sodium dodecyl sulfate
SDS-PAGE	SDS-polyacrylamide gel electrophoresis
SMCC	Succinimidyl trans-4-(maleimidylmethyl)cyclohexane-1-carboxylate
t-BuOK	Potassium *tert*-butoxide
TBAF/TBAI	Tetra-n-butylammonium fluoride/iodide
TBSCl	*tert*-Butyldimethylsilyl chloride
TFA	Trifluoroacetic acid
THF	Tetrahydrofuran
THPTA	Tris(benzyltriazolylmethyl)amine
TLC	Thin-layer chromatography
VEGF	Vascular endothelial growth factor
WHO	World Health Organisation
XTT	Cell Proliferation Kit II

Chapter One: Introduction and Literature Review

1.1 Cancer

1.1.1 Background

The first record of the mention of cancer reaches back to ancient Egypt, some five thousand years ago, around 3000 BCE. This record exists in a script termed the Edwin Smith Papyrus, which was named after an American collector who acquired the script while living in Egypt in 1862.[1] Mention was made, for the first time, of breast cancer and concluded that it is of untreatable nature. Years later, a Greek physician by the name of Hippocrates (460–375 BCE) described cancer as reminiscent of a crab, leading to the Greek term *carcinos*. This describes the roots of the term we use today, which is Latin for crab, coined by a Greek residing in Rome by the name of Aulus Cornealius Celsus when he used Latin as the language of medicine for the first time.[2] Many types of cancer were reported in these times along with various treatment options, including herbal remedies, surgery, cauterisation and even pastes with metal content such as mercury.[3]

Scientific endeavour in cancer research has come a remarkably long way in the modern era and yet we are still faced with cancer as a pressing threat to health in our society. In a 2004 report by the World Health Organisation (WHO), cancer was statistically regarded as the leading cause of death in developed countries and the follow up contributor in developing countries. In 2008 alone, 12.7 million new cancer cases were estimated to have surfaced and cancer related deaths tallied at an immense number of 7.6 million people.[4] Vast numbers of distinct cancer types are documented, with 27 major types accounting for almost all incidences and mortalities worldwide, according to the International Agency for Research on Cancer. The distribution of these cancers is complex and varies within the sexes as well as when comparing developed and developing countries.[5] Lung and breast cancer show the highest incidence and mortality values in males and females respectively, each with values ranging between 10% and 23% of all cancer cases. Following these are the colorectum, stomach, liver and prostate cancers, each with incidence and mortality values accounting for over 5% of cancer types.[4,5] Although these rates are currently decreasing in developed countries, it is projected that the global values will increase to an annual 26 million incidences and 17 million deaths by 2030, due to among other factors the aging of populations.[6–8] Looking at how cancer has persisted through human history and development and the destruction it has caused, it is imperative for modern science to be in pursuit of causes, targets and novel therapeutics to aid in its demise.

1.1.2 Causes

Medical understanding of the causes of cancer has improved since the likes of Hippocrates, who believed the cause was solely due to an imbalance of the four humors: blood, phlegm, yellow bile and black bile.[2] We are now aware that the causes of cancer originate from within a complex system, morphing along with the environment and the resulting stresses of a developing life on earth. However, the main contributors are thought to include poor diet, the use of tobacco and alcohol, physical inactivity, geophysical and genetic factors, reproductive behaviour, infection and occupational exposure to carcinogens, amongst others.[9–12] Tobacco smoking is well known to cause cancer, and accounts for the majority of lung cancer cases of up to 91% in men and 89% in women.[13,14] The carcinogenic effects of tobacco use are also largely responsible for cancers of the oesophagus, larynx and mouth and contribute to those of the bladder, pancreas, kidney and stomach.[11] Although it is difficult to relate cancer incidence directly to diet, studies in humans as well as animals have shown that an increase in fruit and vegetable intake is inversely related to cancer risk.[15] This effect can be attributed to the vast number of beneficial chemical components found in fruits and vegetables. Among these are carotenoids, ascorbic acid, folic acid, dithiolthiones, coumarins and allium compounds.[16] A link between cancer incidence and obesity, a condition largely due to poor diet and physical inactivity, was found by a study surveying the Swedish population over 29 years, which reported a 33% excess cancer occurrence in obese people.[17] Apart from behavioural causes, systemic factors such as chronic inflammation are tightly associated with tumour progression, in which malignant cells develop a relationship with the immune system - often as a result of infection.[18,19] Perhaps the most important of all the causes lie in the genetic information held in each one of our cells, encoding our cellular products and processes. Here, extensive research effort is being focused on understanding genetic predispositions and gene mutations in the development of the cancer phenotype.[12,20]

On a cellular level it is possible to gain greater insight into the origins of cancerous cells and their development into neoplasms. A simplified view can be achieved by classifying cancer as cells that display continual proliferation and do not respond to regulation signals acting on the cell cycle.[21] A schematic of the eukaryotic cell cycle, comprising phases G_1, S, G_2 and M, can be seen in **Figure 1**. The G_1, S and G_2 phases can be grouped and termed the interphase, signifying the cellular events in preparation for mitosis (M phase). In G_1, S and G_2, the cell prepares for DNA replication, undergoes DNA replication and prepares for mitotic division of the cell, respectively.[22]

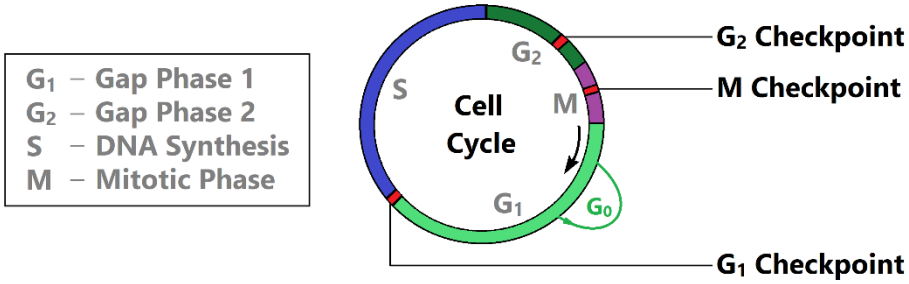

Figure 1: *A cell cycle diagram depicting the various phases and checkpoints leading up to mitosis in eukaryotic cells.*

The movement through these phases is largely controlled by the interactions of proteins termed cyclins and cyclin-dependant kinases (CDKs), which exist in various forms specific for certain stages of the cycle. The CDK proteins are responsible for activating their targets via phosphorylation but are inactive themselves unless bound by the appropriate cyclin.[23] For example, the induction of DNA synthesis is brought about in the beginning of the S phase by a complexation of cyclin E and CDK2, due to high cellular concentrations of cyclin E at the G_1/S boundary.[24] The concentration of specific cyclins is controlled throughout the cell cycle, in which only those required for the current phase are present in high numbers to initiate their respective CDK.[25] Should DNA damage occur in a cell, it is important that these complexes are inactivated to allow for a halt in the cycle for DNA repair. Whilst transference of multiple mutations could lead to malignancy over time, the mutation of a single proto-oncogene would facilitate tumorigenesis if not successfully repaired before cell division.[26] This cell cycle cessation is achieved by cell cycle checkpoints, described by a series of extremely complex protein interactions, making use of sensor, transducer and effector proteins which are able to chemically modify their targets to regulate the cycle. The sensor proteins are able to detect DNA damage and swiftly activate the transducer proteins, which are usually kinases, resulting in signal amplification by the phosphorylation of appropriate effector proteins.[27]

Various checkpoints are instated among the phases and are responsible for arresting the cycle should certain criteria not be met. The G_1 checkpoint is reached at the G_1/S transition before DNA replication, this checkpoint ensures that the DNA is free of mutations and that cellular reserves are sufficient for the mass synthesis event.[28,29] Upon completion of DNA replication, the cells enter G_2 in preparation for mitosis at which point the second major checkpoint is encountered, the G_2 checkpoint. Here, the newly replicated DNA is assessed for damage and replication completeness before the chromosomes are organised for the division event.[27] The M phase begins with

alignment of the chromosomes, on the metaphase plate of the cell, by use of complex cytoskeletal networks comprising mainly microtubules. Before progressing to anaphase, at which point microtubule spindles attached to the chromosomes pull the DNA to opposite poles of the dividing cell, the M checkpoint ensures adequate connection of the spindles to the chromosomal DNA.[30] Most cancers described in the literature display defects in these checkpoint events, allowing for the cells to accumulate mutations, leading to severe malignancy.[29] This is well demonstrated by a protein termed p53, a tumour suppressor protein which is mutated in almost all forms of cancer.[31] In healthy cells, a DNA mutation recognised in the G_1 checkpoint will be conveyed by sensor proteins to transducers such as ATM, Chk1 and Chk2. These transducers then indirectly activate p53 which inhibits the previously mentioned CDK2-Cyclin E complex, resulting in the delay of S phase processes.[27] This protein, often termed "the guardian of the genome", is also responsible for activating apoptotic pathways, leading to cell death, if the cell is unable to repair the damage.[29,32] One can easily extrapolate the negative effects of a mutation in any of the genes coding for proteins involved in these cascades, particularly p53.

Many cells remain in what is known as the quiescent (G_0) phase, which is a state describing cells not actively progressing in the cell cycle but able to re-enter G_1 upon presentation of specific signals. This state is maintained by various signalling pathways and the downregulation of genes involved in DNA replication and progression in the cell cycle.[33] The entry into the quiescent state or the maintenance thereof is due to the absence of growth factors. When present, these factors bind to cell surface receptors, resulting in the activation of proteins that facilitate the processes of the active cell cycle.[34] One of the fundamental traits of cancer cells is their inability to be regulated by the absence of growth factors or their ability to supply themselves with growth factors, thereby continuing with the cell cycle regardless of possible signalling cascades indicating unfavourable conditions for replication.[35]

Bypassing the quiescent state and negating checkpoint control are not the only cellular traits representative of cancer cells; instead, there are multiple characteristics attributed to these cells. Briefly, these cells also evade growth suppressors, resist cell death, are able to replicate many more times than normal cells in their lifetime, induce the formation of new vessels to supply nutrients to the cell mass and are able to metastasise to spread to other tissues in the body.[35] Understanding these traits and the associated pathways is important in identifying therapeutic targets in the fight against cancer.

1.1.3 Targets and therapeutics

Treatment of cancer throughout history was dominated by surgery until the idea of using chemicals as a method of treatment was first introduced by Paul Ehrlich, a German biochemist, at the end of the 19th century.[36] In the early 1900s, the advent of chemotherapy was paralleled by the introduction of radiation therapy, the ability to grow human cancer cell lines in tissue culture and the identification of rodent model systems.[36,37] Around 1950, the first promising chemotherapeutic agents were introduced, beginning with the synthesis of folic acid analogues aminopterin and amethopterin, and their success in achieving partial remission in children with leukemia.[38] This was followed by the discovery of several antitumour antibiotics as well as 5-fluorouracil, all which have achieved successful results in the treatment of malignancies.[37] Successes in chemotherapy fuelled investment into the industry and resulted in multiple establishments that focused on screening thousands of chemicals for activity.[39] With this came new active compounds and the notion of combination therapy, in which multiple drugs were used concurrently in treatment programs. Combination therapy proceeded to provide sustained remissions in the majority of patients with Hodgkin's disease and children with acute lymphoblastic leukemia (ALL), reinforcing the idea of a cure in chemotherapy.[40] Traditional chemotherapy acts generally on cells that divide rapidly, making use of compounds such as vincristine and chlorambucil (**Figure 2**), which interfere with DNA replication and microtubule polymerisation, respectively. However effective they may be against cancer cells, these agents also cause undesirable death of normal, rapidly proliferating tissues such as epithelial or hair cells.[41] In combatting this issue, a pivotal progression arose with the advent of targeted therapy - linking chemotherapy and molecular biology to allow for the tailoring of chemotherapeutics for specific cellular pathways.[37]

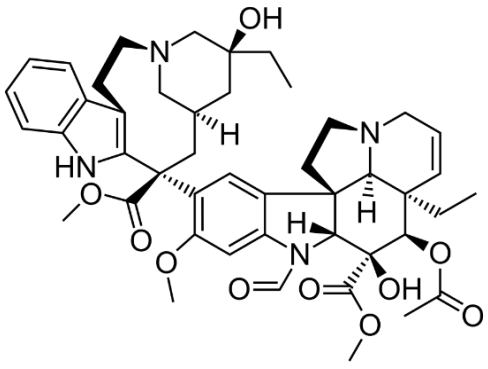

Vincristine

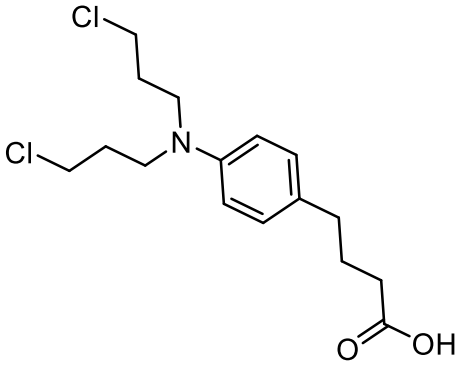

Chlorambucil

Figure 2: *Chemical structures of chemotherapy agents vincristine and chlorambucil, the latter being derived from the Madagascar periwinkle plant, catharanthus roseus.*

Classical targeted chemotherapy can be divided into two main subcategories, as those either making use of small molecule agents or employing monoclonal antibodies. The former usually interferes with cellular pathways by inactivating specific tyrosine kinase enzymes or initiating apoptosis, whereas the latter function by binding to specific antigens present on target cell surfaces in order to elicit their function.[41]

Important cellular pathways of focus in small molecule targeted therapy are those that act in controlling proliferative signalling. One such pathway is the mitogen-activated protein kinase (MAPK) pathway, which is tightly involved in multiple cellular processes including proliferation control.[42] When growth factors bind certain cell surface receptor tyrosine kinases, such as the epidermal growth factor receptor (EGFR), the MAPK pathway is activated through phosphorylation cascades, which ultimately facilitates the upregulation of genes that stimulate proliferation.[43] Many human cancers display mutations in the EGFR or the downstream kinases Ras, Raf, MAPK/ERK kinase (MEK) and the extracellular signal-regulated kinase (ERK), leading to uncontrolled cell growth.[34] The synthetic chemical compound ZD1839 (Iressa), a small molecule agent of the anilinoquinazoline class, functions by inhibiting EGFR phosphorylation ability. This has implications in downstream regulation, ultimately inhibiting CDK2 activity and resulting in G_1 arrest, which has proved successful in the treatment of patients with non-small cell lung cancer.[44] Flavopiridol, a flavonoid alkaloid, functions via competitively binding at the adenosine triphosphate (ATP) binding site of various CDK proteins and was the first of many direct CDK inhibitors of this class to enter clinical trials.[45] An indirect modulation of CDK activity can be found in the relationship between the aforementioned p53 protein and its negative regulator, murine double minute 2 (MDM2). In human tumours, MDM2 is frequently found to be overexpressed, which results in an elevated degradation of the p53 tumour suppressor.[46] The nutlins, a series of synthesised cis-imidazoline analogues, have been found to displace p53-complexed MDM2, which has stimulated research into finding a suitable therapeutic in this class.[47] Great success in hormonal breast cancer therapy has resulted from the adjuvant application of tamoxifen, a nonsteroidal triphenylethylene derivative, in which binding to cell surface oestrogen receptors on target cells results in the promotion of anti-proliferative pathways.[48] Therapeutics targeting apoptotic pathways are also in development, with major interest in those targeting the BCL-2 protein family. These proteins regulate an intrinsic apoptotic pathway, which results in the permeabilisation of the mitochondrial outer membrane and the release of apoptogenic factors into the cytosol.[49] Molecular structures of a few of the above mentioned small molecule agents are presented in **Figure 3**.

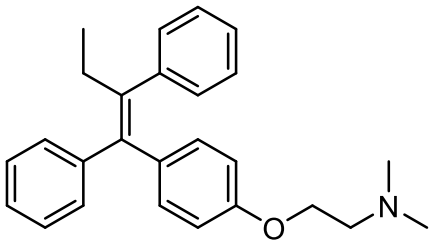

Tamoxifen

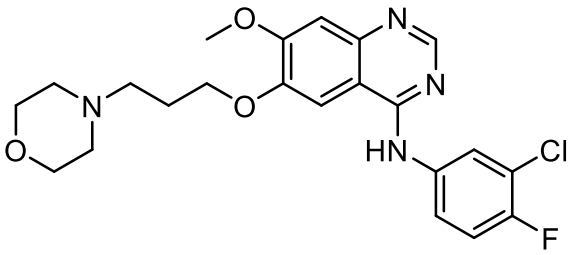

Iressa

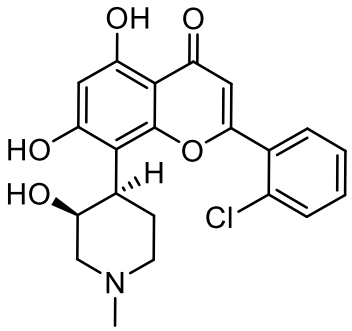

Flavopiridol

Figure 3: *Molecular structures of small molecule chemotherapy agents flavopiridol, tamoxifen and Iressa.*

By comparison, monoclonal antibody (mAb)-targeted therapy exploits the overexpression of cell surface proteins on various types of cancer cells, allowing for greater specificity towards these cells. The structure of antibodies can be conveyed simply by differentiating two main regions: the fragment crystallisable (Fc) domain as one that is recognised by the host system to elicit immune function, and the fragment antigen-binding (Fab) domain, which is specific for the binding to target proteins.[50] The first examples of mAbs were derived from murine systems, but most therapeutically relevant examples have employed either partially humanised (chimeric), humanised or fully human forms, allowing for minimised host immune clearance.[51] As with small molecule therapeutics though, the ability of mAbs to target growth and differentiation signalling in cancer cells has been well explored. One such example is the chimeric mAb Cetuximab, which binds the EGFR on target cell surfaces and has been approved for the treatment of colorectal cancer.[52] Immune-mediated tumour cell killing is achieved by the fully human mAb Ipilimumab, which has shown positive activity in patients with metastatic melanoma by eliciting T-cell immune-mediated cell death. It acts by binding to the cytotoxic T-lymphocyte–associated antigen 4 (CTLA-4) that is present on target cell surfaces, which downregulates T-cell activation pathways in its unbound state.[53] Activity in aggressive B-cell neoplasms, such as diffuse large B-cell lymphoma, has been achieved by the chimeric mAb

Rituximab, which binds to CD20 antigens resulting in antibody-dependent cell-mediated cytotoxicity.[54,55] Tumour angiogenesis is in part regulated by the overexpression of the vascular endothelial growth factor (VEGF) glycoprotein and progress in treating colorectal cancer has been achieved with Bevacizumab, a humanised mAb which inhibits angiogenesis by binding the VEGF epitope.[56]

The success of both small molecule and mAb targeted therapy in the treatment of cancer is evident, allowing for improved prognosis for patients faced with many types of cancer. A form of targeted therapy not yet discussed, and arguably the most sophisticated among targeted chemotherapy agents, makes use of a combination of the two, utilising the directing capabilities of antibodies with the potency of small molecule drugs. The therapeutics resulting from this approach are termed antibody-drug conjugates (ADCs), and the focus of this MSc study lies in the synthesis and biological evaluation of a novel ADC therapeutic for cancer chemotherapy.

1.2 Antibody-Drug Conjugates

1.2.1 History

The notion of ADCs began once again with Paul Ehrlich in the early twentieth century, who proposed the idea of using antibodies as delivery mechanisms for cytotoxic agents by covalently linking the two via a linker structure. Initially, the efficacy of these therapeutics were limited as polyclonal or fully murine monoclonal antibodies were the benchmark, displaying low serum half-life due to human immune response.[57] This problem was overcome as the field was developed further and antibodies incorporating a greater percentage of human antibody character were put to use.[58] The cytotoxic agents initially employed were those which already showed promise in treating cancer, and whose mechanisms of action were well established, such as chlorambucil and amethopterin.[59,60] This became a limitation in the sense that classical chemotherapeutics did not employ delivery mechanisms and had to exhibit low toxicity in order to be acceptable. Further research into ADCs resulted in toxins with greater potency being incorporated, which increased overall drug efficacy, thereby allowing for lower therapeutic doses.[61] Another shortfall of first-generation ADCs lay in the instability of the linker systems used, which included acid-labile hydrazone linkers, as well as ones making use of disulfide bonds. This is well demonstrated in the therapeutic Gemtuzumab ozogamicin (Mylotarg), one of the first commercial ADCs incorporating a hydrazone linker, which was withdrawn from the market due to serum instability and consequent off-target toxicity.[62] Modern linker strategies, including peptide and non-cleavable linkers, have allowed for the alleviation of this shortfall and

have been successfully incorporated in several novel ADCs in recent times.[63] Research into ADC therapeutics is relatively young, but their potential has been realised by the scientific community and constant advances in the field have allowed for the successful application of a few approved therapeutics, with many in the clinical trials' pipeline.

1.2.2 Structure and activity

The relatively recent and successful development of ADCs has set the stage for a new class of antineoplastic, chemotherapeutic drugs having the potential for increased specificity and toxicity and which can be tailored for a large range of cancer types.[64] The capability of ADC therapeutics in being effective for the treatment of cancer is largely dependent on their structural nuances, in which careful consideration of multiple factors that influence their activity is essential in the design process. The appeal of these drugs rests in their modifiable nature and their assembly relies on the cooperation of three main entities - the antibody, the cytotoxic agent and the linker, the latter being conscientiously designed to adequately bind the toxin to its delivery vehicle until the site of activity.[61]

Antibodies best suited for incorporation in ADC therapeutics are those that display minimal immunogenicity, a low clearance rate, high specificity and an optimal affinity for target antigens.[61] Displaying minimal immunogenicity and clearance is attributed to the avoidance of recognition by B lymphocytes which produce anti-therapeutic antibodies upon recognition of a foreign entity.[65] The progression from murine antibodies towards those with greater human composition in ADC therapeutics has mirrored that of mAb-targeted therapy and is a key consideration in the design process.[57,66] Antibodies displaying high specificity and affinity result in more effective therapeutics as these properties minimise off-target activity and reduce likelihood of dissociation before endocytosis, respectively. This is mostly related to the inherent properties of each antibody, and research in improving antibody-affinity by computational design is underway with positive results.[67] Another important factor is antibody size, in which smaller antibodies or fragments thereof have displayed increased therapeutic potential.[68] Reduced size has been shown to increase tumour penetration and overall potency when compared to ADCs incorporating full immunoglobulins such as IgG1.[69] Recent research suggests this can be achieved in part with the use of nanobodies or single-chain variable fragments (scFv), the latter defined as fusion proteins which comprise variable regions of the heavy and light chains of immunoglobulins connected by a short linker peptide.[70] Apart from the advantages afforded by reduced size, the scFv antibody format boasts versatility over full length monoclonal antibodies in that it is customisable for optimal affinity and specificity

through recombinant DNA technology and protein engineering.[71] This format also lacks the Fc domain, which acts to reduce immunogenicity and thus increase efficacy.

The cytotoxic agents that are generally employed are those with high potency, have a known mechanism of action, are amenable to modification for linker attachment and which are stable at physiological pH.[61,65] The two classes of toxins commonly incorporated are DNA-damaging agents and microtubule polymerisation inhibitors, both displaying activity in picomolar or nanomolar concentrations.[64]

DNA-damaging toxins include calicheamicin analogues, the duocarmycins and the anthracyclines. The calicheamicin toxins are a class of antibiotics with a cyclic enediyne functionality that bind the minor groove of the DNA helix. Upon binding they undergo a reaction with the DNA sugar backbone analogous to the Bergman cyclisation, in which a diradical species is formed that abstracts hydrogen atoms from the backbone, resulting in double strand breaks.[72,73] Similarly, duocarmycins bind the DNA minor groove, but their toxicity results from the *N*-alkylation of DNA adenine residues on cells in the G_2 or M phase, leading to apoptosis by the disruption of DNA processing proteins.[74–76] Anthracyclines, including doxorubicin, are antibiotic tetracyclic compounds incorporating an anthraquinone backbone and a sugar moiety. They exhibit toxicity by the intercalation of DNA, which interferes with transcription processes, leading to the activation of apoptotic pathways.[77]

The toxins inhibiting microtubule polymerisation include the maytansinoids, as well as a series of toxins termed the auristatins. Microtubules are imperative in many cellular processes and their disruption leads to signalling cascades that initiate apoptosis.[78] Structurally, microtubules exist in a hollow cylindrical form and are constructed from α- and β-tubulin heterodimers. These heterodimers associate in a helical fashion, displayed in **Figure 4**, and incorporate guanosine triphosphate (GTP) molecules which are essential in their elongation and degradation.[79]

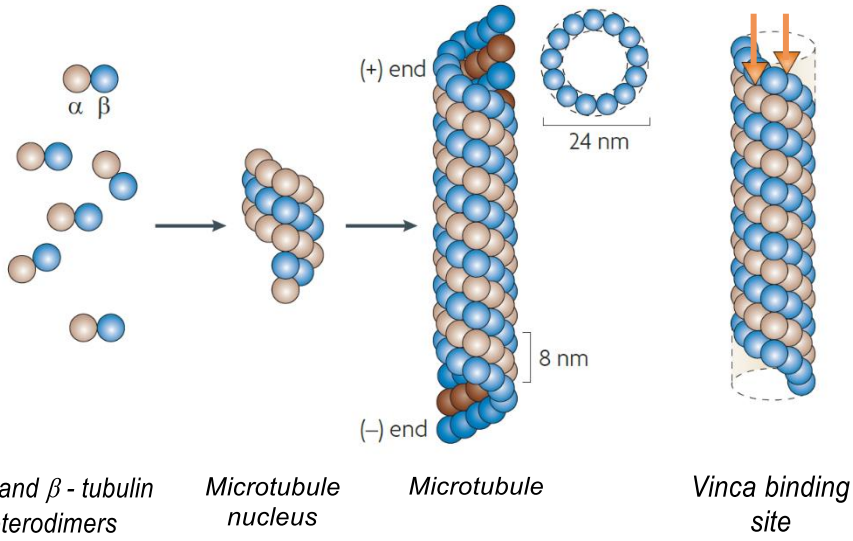

Figure 4: *A depiction of tubulin structure, in which cylindrical microtubules are synthesised from heterodimers of α- and β-tubulin. The vinca binding site is highlighted, where several microtubule-inhibiting toxins bind to inhibit strand elongation.*[80]

The strands are especially important in mitosis where they are required for chromosomal separation, elongating from centrosomes at opposite poles of the dividing cell to bind sister chromatids.[78] An example of the interruption of microtubule polymerisation lies in the maytansinoids, a series of polyketide, macrolide-containing ansa compounds which bind tubulin to elicit their apoptotic effect.[81] The auristatins are structurally derived from dolastatin 10 (**Figure 5**), a potent antineoplastic natural product.

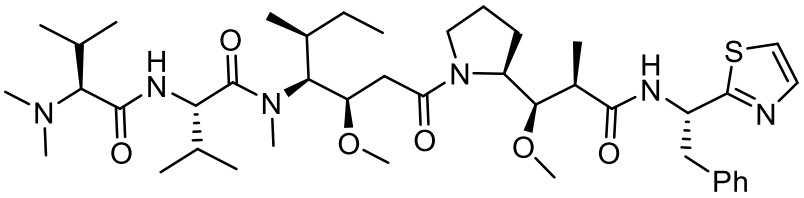

Dolastatin 10

Figure 5: *The chemical structure of dolastatin 10, a potent pentapeptide microtubule inhibitor toxin.*

This potent pentapeptide toxin was first isolated in 1987, from the sea hare *Dolabella auricularia*, and was recorded as the most active antineoplastic substance known to man.[82] Testament to its potency, dolastatin 10 is present in very low concentration in the sea hare, where one metric ton of wet animal mass is required to isolate 28.7 mg

of pure dolastatin 10. In spite of its potency, this toxin failed to achieve a status for the treatment of cancer owing to its significant toxicity at the maximum tolerated dose. The difficulty in harvesting this toxin, paired with its potent toxicity led to the production of synthetic analogues in an attempt to harness its power.[83]

It was found that the removal of one N-terminal methyl group did not largely affect cytotoxicity, which stimulated the idea that these toxins could be amenable to linker attachment and used in ADC therapeutics.[84,85] The first synthetic analogues displaying promise were auristatin-E and monomethyl auristatin-E (MMAE), in which the thiazole-containing C-terminal amino acid in dolastatin 10 (dolaphenine) was replaced by norephedrine. The newly found MMAE was subsequently incorporated into an ADC and the resultant therapeutic was found to be highly efficient in eliminating cancer cells.[86] This fuelled auristatin analogue research, which allowed for the development of various other novel auristatins, including auristatin-F. Monomethyl auristatin-F (MMAF), displayed in **Figure 6**, is the cytotoxic agent precursor employed in this MSc study for the generation of novel ADCs, and its cytotoxic properties are due to its binding at the vinca binding site of elongating microtubules.[80]

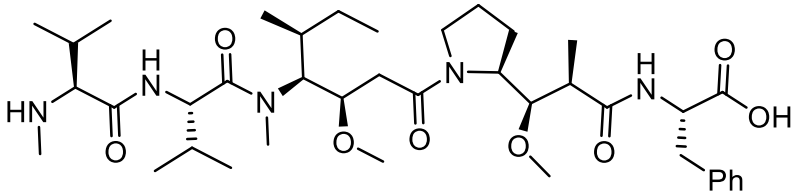

Monomethyl auristatin-F

Figure 6: *The chemical structure of MMAF, the cytotoxic agent employed in this study.*

In the case of MMAF, the dolaphenine amino acid is replaced by phenylalanine, which introduces a carboxyl group on the C-terminus, allowing for synthetic modifications not possible on other auristatins.[87] It has been reported that auristatin-F and MMAF in unbound states exhibit lower cytotoxicity than MMAE and its counterparts, which was stipulated to be due to the free carboxylic acid inhibiting cell permeability. For this reason, linkers bound to the carboxylic acid functional group are usually employed when incorporating this toxin into ADC therapeutics, and this is the strategy used in this study.[88]

Linker systems utilised in ADC therapeutic generation are required to facilitate the release of the cytotoxic agent once internalised by the target cell, to exhibit stability in circulation and to include functionality for conjugation to the antibody of choice once bound to the cytotoxic agent.[61,65] Linkers that have been developed are diverse, but

are generally grouped into two major classes: cleavable and non-cleavable linkers. Cleavable linkers can be segregated once again into three classes as pH-sensitive, those cleaved by higher concentrations of intracellular glutathione and those which are protease-sensitive.[89] Linker systems displaying pH-sensitivity usually incorporate hydrazone functionality, allowing for cleavage in acidic environments such as that of the cellular endosome and lysosome.[90] Those incorporating disulfide bonds are dependent on higher intracellular levels of glutathione and other reducing agents that result in reductive cleavage of the linker.[91] Finally, an important example of a protease-sensitive linker incorporated into many ADC therapeutics is the valine-citrulline dipeptide, which is sensitive to the Cathepsin B protease found intracellularly. This strategy usually incorporates a self-immolative *p*-aminobenzyloxycarbonyl (PABC) spacer moiety, which is responsible for allowing room for the protease to access the dipeptide and releases the bound agent subsequently in an unmodified state.[92] The mechanistic detail of the enzymatic cleavage of the valine-citrulline dipeptide and subsequent toxin liberation is displayed in **Figure 7**.

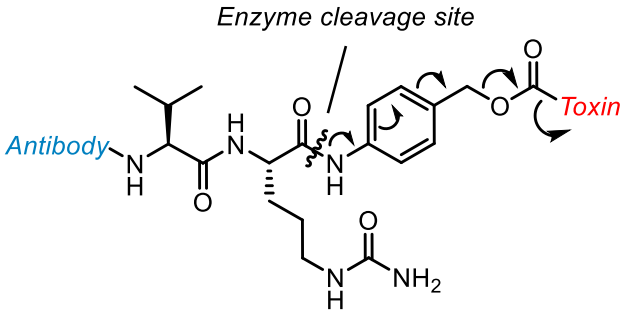

Figure 7: *The general structure of a valine-citrulline-PABC linker incorporated into an ADC, with mechanistic detail of the enzymatic cleavage process.*

By comparison, non-cleavable linkers are intended to remain bound to the toxin and antibody until complete proteolytic degradation of the ADC therapeutic by lysosomal proteins, following delivery to the cellular lysosomal compartment.[93] Those incorporating thioether linkages, for conjugation to either the toxin or antibody, are commonplace (**Figure 8**) - including maleimidocaproyl, mercaptoacetamidocaproyl and the bifunctional succinimidyl *trans*-4-(maleimidylmethyl)cyclohexane-1-carboxylate (SMCC) linker systems.[86]

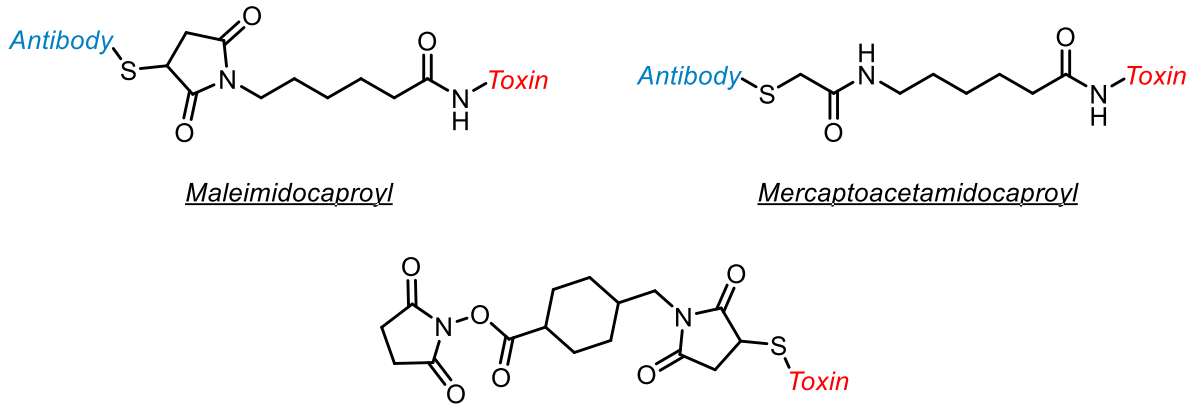

Figure 8: *The chemical structures of various non-cleavable linker systems.*

Cleavable linkers are appealing in that they are designed to release the toxin at a specific point following endocytosis of the ADC, without relying on transport to the lysosomal compartment for processing, and generally liberate the toxin in a largely unmodified form. However, these linker systems require substantially more synthesis effort and have an increased risk of premature cleavage due to their increased lability relative to non-cleavable linkers. Therapeutics containing non-cleavable linkers are advantageous in that they display extremely high serum stability, resulting in minimal off-target toxicity.[94] Furthermore, non-cleavable thioether linker systems incorporating polyethylene glycol (PEG) have been conjugated to maytansine analogues with no loss in efficacy in comparison to cleavable linkers.[95] The linker utilised in this study is a PEG-based non-cleavable linker (including functionality for self-labelling fusion protein conjugation) that is attached to the C-terminus of auristatin-F, which as mentioned previously is a convenient site for attachment.

1.2.3 Success of antibody-drug conjugates in modern therapeutics

Clinically approved ADC therapeutics in the last decade include Brentuximab vedotin, which has been successful in treating patients with relapsed Hodgkin lymphoma and systemic anaplastic large cell lymphoma, Trastuzumab emtansine for the treatment of HER2 positive metastatic breast cancer, and Inotuzumab ozogamicin for the treatment of refractory B-cell precursor ALL.[96–99] The structures of these therapeutics are displayed in **Figure 9**, in which each integral element of the respective therapeutics is highlighted in colour – the cytotoxic agent in red, the linker in green and the antibody in blue.

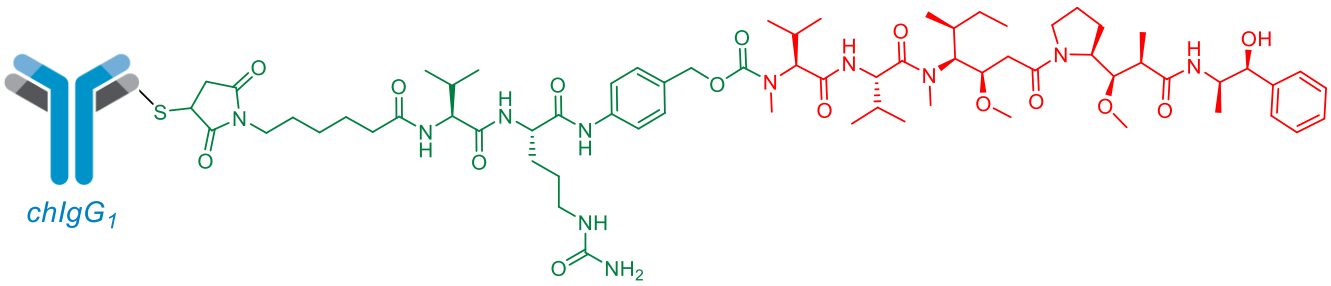

Brentuximab vedotin

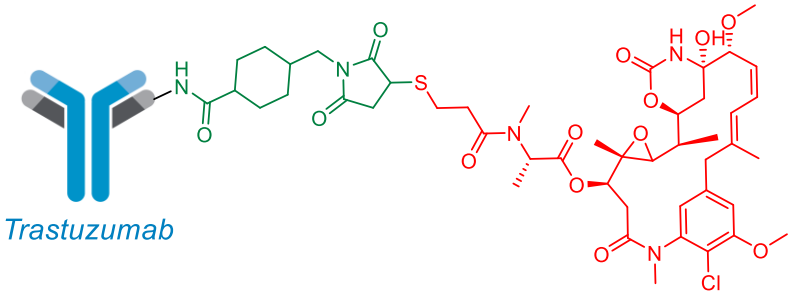

Trastuzumab emtansine

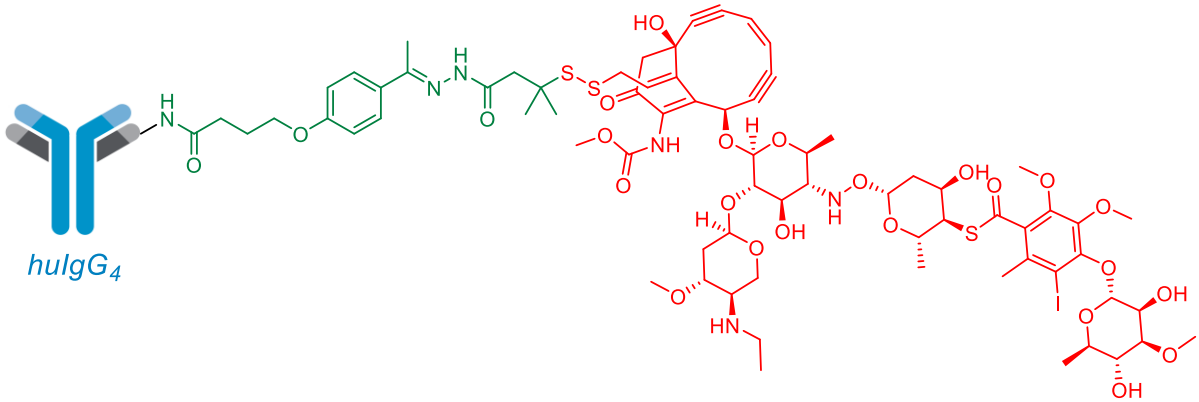

Inotuzumab ozogamicin

Figure 9: *Chemical structures of three ADC therapeutics in medical use, Brentuximab vedotin, Trastuzumab emtansine and Inotuzumab ozogamicin.*

Brentuximab vedotin, approved in 2011 under the name Adcetris, incorporates the powerful cytotoxic agent MMAE to trigger apoptotic pathways in the target cell.[97] This therapeutic integrates a valine-citrulline-PABC proteolytically cleavable dipeptide linker, allowing for liberation of the toxin once internalised by the target cell by internal proteases. It is conjugated to a cysteine thiol on the chIgG1 chimeric antibody, targeting the CD30 antigen, via a Michael addition reaction with a maleimide functional group present on the linker.[93,100] By comparison, Trastuzumab emtansine, approved in 2013 under the name Kadcyla, incorporates the humanised mAb trastuzumab, which targets the HER2 receptor present on certain breast cancer cell

lines. The integrated cytotoxic agent is termed mertansine, a thiol-containing derivative of the powerful microtubule inhibitor maytansine.[101] The unbound SMCC non-cleavable linker contains both maleimide and succinimidyl ester functionality. The maleimide is conjugated to the toxin via a Michael addition, whereas the succinimidyl ester is responsible for conjugation with a free amine on lysine antibody residues.[102] Finally, Inotuzumab ozogamicin, approved in 2017 under the name Besponsa, targets the CD22 antigen via an engineered huIgG4 antibody. It incorporates an acid-labile hydrazone linker that links to a calicheamicin toxin via a disulfide bond, which is susceptible to cleavage by intracellular reducing agents, and also conjugates via lysine residues on the antibody.[99]

The latest ADC therapeutics were approved for clinical use in June and December 2019, namely Polatuzumab vedotin and Trastuzumab deruxtecan.[103] The former, released under the name Polivy, is similar to Brentuximab vedotin in that it utilises the MMAE toxin, a valine-citrulline-PABC linker and the same maleimide moiety for antibody conjugation. This therapeutic differs only in that it is conjugated to a humanised IgG1 antibody, targeting the CD79b antigen, for use in relapsed diffuse large B-cell lymphoma patients.[104] Trastuzumab deruxtecan, released under the name Enhertu, targets the HER2 antigen, for use in HER2 positive metastatic breast cancer. It incorporates an exatecan derivative as the cytotoxic agent, a novel topoisomerase I inhibitor derived from camptothecin, and a proteolytically cleavable tetrapeptide linker. Conjugation to a cysteine thiol on a humanised IgG1 antibody is also afforded via the same maleimide-containing fragment, present in both Adcetris and Polivy.[103]

1.2.4 Conjugation methods

To date, most conjugation methods employed in ADC generation make use of the side chains of specific antibody residues as sites of conjugation with linker systems. These include the amino groups present on lysine residues as well as sulfhydryl groups on cysteine residues, the latter usually accessed by reducing interchain cysteine disulfide bonds.[86] Many unique chemistry alternatives are present for each of these approaches owing to the rich nature of existing nitrogen and sulfur chemistry. Conjugations with lysine residues include reaction with succinimidyl esters to form amide bonds, as well as the reaction with isothiocyanates to form thiourea linkages. Those with cysteine include the reaction with haloacetyl and maleimide functional groups to produce thioether linkages.[89] Although these conjugation techniques have been widely used, generally they result in products with heterogeneity, in which mixtures of products are produced with varying drug-antibody ratios (DARs).[105] Owing to the abundance of lysine residues on antibodies, conjugation techniques utilising this handle often result

in products with high DAR values. It has been shown that ADCs with high DAR values display accelerated serum clearance and are less tolerated than those with lower DAR values.[65] Another finding in this regard states that antibodies with high DAR ratios exhibit a relatively lower maximum tolerated dose, in which double the amount of an ADC with a DAR of four could be tolerably administered when compared to one of eight with similar *in vivo* potency.[62] In recent years, efforts have been dedicated to the employment of conjugation strategies that allow for both homogeneity and lower DARs. These strategies include cysteine engineering, the incorporation of unnatural amino acids and the use of enzymatic conjugation.[99] Cysteine engineering has been put to use by either replacing cysteine residues with serine to lower the number of reactive thiols, as well as the insertion of cysteine residues to obtain homogeneity, thereby allowing for more tolerable ADCs.[106] Methods incorporating non-natural amino acids have also been developed, such as acetylphenylalanine which provides a unique ketone handle on the antibody for conjugation.[107] An example of enzymatic conjugation lies in the use of bacterial transglutaminase, which catalyses the conjugation of a free amine on the toxin with glutamine side chains of a modified antibody.[108] This MSc study addresses this conjugation issue by studying the use of SNAP-tag conjugation, which eliminates DAR and heterogeneity issues by the incorporation of a self-labelling enzymatic domain into the antibody.

1.3 SNAP-Tag Conjugation

1.3.1 History and uses

The origins of SNAP-tag as a protein labelling tool lie in the exploitation of the human DNA repair enzyme *O*^{6}-alkylguanine-DNA alkyltransferase (hAGT), which functions by identifying and reversing alkylations on guanine base pairs in DNA.[109] An appealing property of this enzymatic transformation is the irreversibility of the reaction, in which the alkylated DNA adduct is permanently bound to the protein.[110] This technology is incorporated by the insertion of a modified hAGT gene at the N- or C-terminus of the gene sequence coding for the protein of interest. Upon translation of the resulting nucleic acid sequence, a SNAP-tag fusion protein is produced which retains the functionality of the original protein and includes the SNAP-tag domain for site-specific conjugation opportunities by recognition of *O*^{6}-benzylguanine (BG) functionality on target probes.[111] The BG moiety (**Figure 10**) mimics an alkylated guanine substrate for the SNAP-tag domain, in which the benzyl 4-position can be functionalised to include a payload of choice. During the conjugation reaction, the antibody is effectively covalently modified with the payload simultaneous with the elimination of guanine.

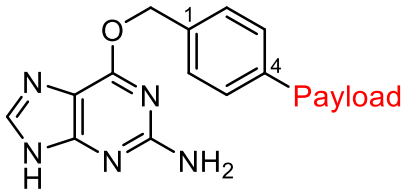

Figure 10: *Benzylguanine structure, in which the benzyl 4-position is functionalised with a payload.*

Owing to the irreversible nature of its function, native hAGT is rapidly degraded by the cell once it has repaired DNA, due to a change in conformation of the enzyme and subsequent ubiquitination for proteasomal degradation.[110] In order to circumvent this issue and result in a stable protein after alkyl transfer, initial modifications to hAGT were carried out in the form of point mutations and C-terminal deletions. Further evolution towards the SNAP-tag protein resulted in the removal of its DNA binding capability, and the introduction of mutations which ultimately allowed for an increase in BG reactivity by 52-fold.[112]

The SNAP-tag technology was initially employed in *in vivo* protein labelling, in which it served as an alternative to the insertion of intrinsically fluorescent proteins such as green fluorescent protein (GFP). This allowed for the covalent modification of proteins with chemical dyes or fluorophores, such as fluorescein. These display increased potential for chromatic diversity and can be introduced at specific points in time, rather than from the point of translation as with incorporation of GFP.[113] This technology has also been utilised in protein quantification studies, as well as those monitoring drug-protein interactions.[114,115] A common drawback in SNAP-tag protein labelling *in vivo* is the interference of endogenous AGT by conjugation with introduced probes, although this is not problematic in its use in ADCs, as the conjugation is performed prior to introduction into the biological system.[113]

1.3.2 Mechanism of conjugation

In its native state, the AGT enzyme interacts with DNA by the folding of the alkylated base pair into the enzyme active site, achieved by the cooperation of essential amino acid residues. Once stabilised in the active site, it comes into contact with a cysteine thiolate, which acts as the nucleophile in a nucleophilic substitution reaction of the S_N2 type at the carbon adjacent to the oxygen on the guanine 6-position (**Figure 11**).[110]

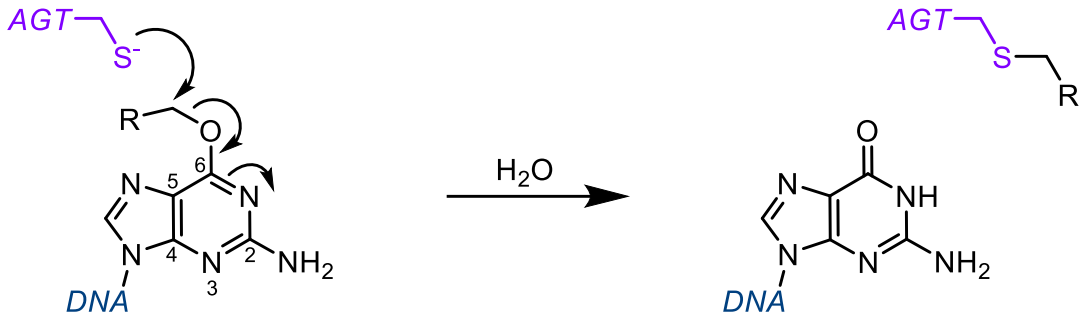

Figure 11: *Mechanistic details of AGT function in DNA alkylation repair.*

Crystal structures of the hAGT active site cocrystallised with guanine residues have been obtained, allowing for insight into the mechanism of action. The BG moiety is seen to be held in place by hydrogen bonding with tyrosine, valine and glutamic acid residues, which orientates the cysteine residue at optimal distance for reaction with the benzylic methylene.[112]

1.3.3 Development for antibody-drug conjugates

This S_N2-based mechanism can be exploited in ADC generation by the insertion of the SNAP-tag domain into antibodies and subsequent conjugation with a toxin bound to a linker system which contains BG functionality. This results in irreversible, covalent bond formation with the displacement of guanine, a mechanism of which can be seen in **Figure 12**.[116] This is analogous to the native AGT mechanism presented in **Figure 11**, in which the DNA alkyl adduct is effectively replaced by the linker-bound toxin.

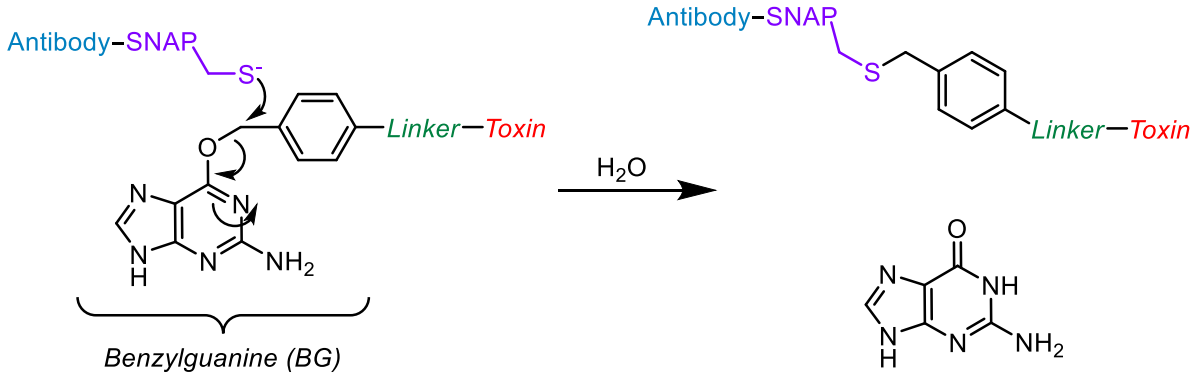

Figure 12: *Mechanistic details of SNAP-tag conjugation in ADC therapeutic generation.*

Research into the suitability of SNAP-tag conjugation in the generation of ADC therapeutics has been carried out by Barth and co-workers, in which several novel recombinant ADCs have been generated for targeting numerous forms of cancer.[117–121] For example, research was undertaken in the field of photodynamic therapy (PDT) using SNAP-tag to produce photoimmunoconjugate agents comprising a

photosensitiser linked to a scFv targeting EGFR. Here, a BG-modified chlorin e6 porphyrin molecule was conjugated to scFv-425, which displayed good selectivity and significant toxicity in target cancer cells upon activation by light.[122] Further research into photoimmunotherapy (PIT) has been carried out with BG-conjugated IR700, a highly conjugated dye molecule that releases apoptosis-inducing reactive oxygen species (ROS) into the cell upon irradiation with near-infrared light. Selective activity in skin cancer cells, known to express high levels of EGFR, was achieved by treatment with the SNAP-tag conjugation product of BG-IR700 with scFv-425 and subsequent irradiation.[120] These research efforts laid the foundation for the successful application of SNAP-tag conjugated ADC products for photoimmunotheranostic purposes in light-accessible cancers including skin, ovarian and breast.[119,121] BG-modified auristatin-F has also been successfully conjugated to scFv-SNAP fusion proteins targeting EGFR and HER2, which culminated in potent *in vitro* activity in breast cancer cell lines.[117,118]

1.3.4 Comparison with other conjugation techniques

The use of SNAP-tag conjugation in ADC therapeutic generation consistently provides a stable DAR with complete homogeneity, which results in a more stable and well tolerated ADC when compared to those produced by heterogenous conjugation methods.[119] However, the 1:1 stoichiometry achieved by this conjugation method naturally incorporates a lower number of toxins than those which yield products with DAR values closer to four, which has implications in potency that can be overcome by the use of extremely potent toxins such as auristatin-F.

1.4 Aim and Objectives

1.4.1 Aim

This study aimed to synthesise a novel ADC displaying therapeutic potential and specificity towards cancer cells by coupling the antimitotic agent auristatin-F, via a BG-containing linker system, to SNAP-tag fusion proteins.

1.4.2 Objectives

- Derivatisation of monomethyl auristatin-F to facilitate coupling with BG-linker systems.

- Synthesis of a BG-linker system incorporating functionality allowing for coupling with auristatin-F.

- BG-modification of auristatin-F, or derivative, to afford an ADC-precursor for SNAP-tag conjugation with scFv-SNAP fusion proteins.

- SNAP-tag conjugation of BG-modified auristatin-F with scFv-SNAP fusion proteins to produce novel ADCs.

- Biological evaluation of generated ADCs *in vitro* to assess efficacy and potential as therapeutics.

Chapter Two: Design Strategy and Synthesis of ADC-Precursors

2.1 General ADC-Precursor Design

In the design and synthesis of ADC-precursor constructs, it is important to consider the key features of an ADC, as discussed in **Chapter One**. These include the conjugation strategy, linker structure and the cytotoxic agent. Seeing as though SNAP-tag was chosen as the preferred conjugation strategy, a central aspect of the design process was the synthetic modification of the cytotoxic agent with a BG moiety. This would ultimately facilitate the conjugation reaction with a recombinant fusion protein containing a SNAP-tag domain, to result in 1:1 stoichiometry.

A general structure for the ADC-precursor synthetic targets in this study is displayed in **Figure 13**.

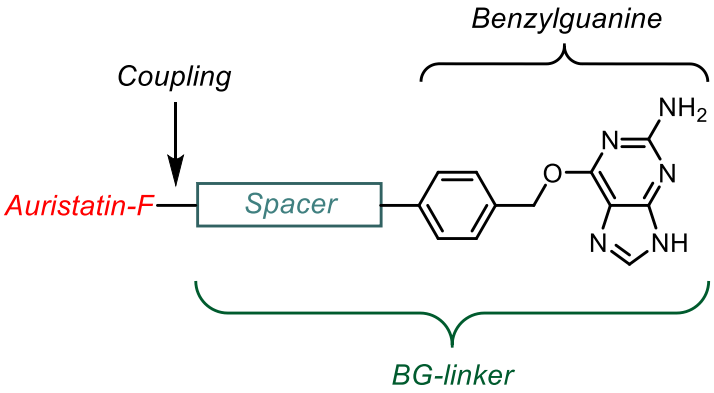

Figure 13: *A general ADC-precursor structure for this study, displaying the key features which require design input.*

Considering the coupling strategy with the BG-linker, two potential sites for modification were available on our cytotoxin precursor molecule, which is displayed in **Figure 14**.

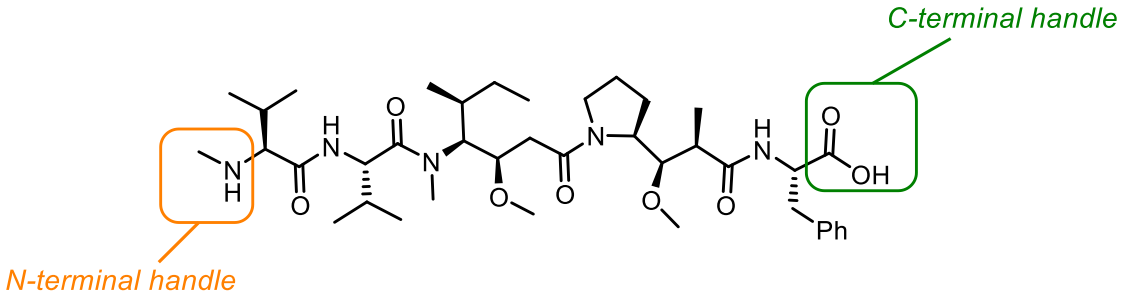

Figure 14: *Structure of MMAF, highlighting the N-terminal and C-terminal handles which are amenable to synthetic modification.*

As previously mentioned, the C-terminal carboxylic acid was most attractive for linker attachment and as a result it was necessary to restrict the reactivity of the N-terminus.

The literature is dominated by installing dimethyl character at the N-terminus of auristatins, likely owing to Dolastatin 10 displaying this structural feature. This was also the major strategy utilised in this study, although acylation of the N-terminus with Boc_2O was also performed.

The spacer, proposed to be derived from 4,7,10-trioxa-1,13-tridecaneamine (**Figure 15**), is required in order to distance the toxin from the BG moiety.

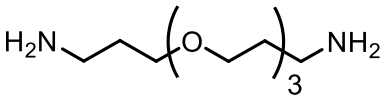

Figure 15: *Molecular structure of 4,7,10-trioxa-1,13-tridecaneamine, the acting spacer in the synthesis of BG-linker systems in this study.*

This PEG-based spacer was thought to be of an appropriate length to distance the toxin from the BG entity, while the terminal amine functional groups were attractive for derivatisation in terms of linker construction. Other contributing factors in support of this spacer included its accessibility, hydrophilic nature and relatively low cost. Furthermore, PEG chains have a presence in the scientific literature, in the fields of biochemistry, structural biology and medicine, confirming their compatibility with biological systems.[123] In the design aspect of this project it was realised that more sophisticated linker technologies are available, but this spacer was deemed suitable for incorporation as a proof of concept and to build a foundation and understanding for future research into the synthesis of ADC-precursors.

The most direct approach to achieving an auristatin-F ADC-precursor was deemed through amide coupling with the free carboxylic acid of the toxin. This would require having an amine functionality on the BG-linker, which led to conceptualisation of the first BG-linker target (**10**) in this study (**Figure 16**).

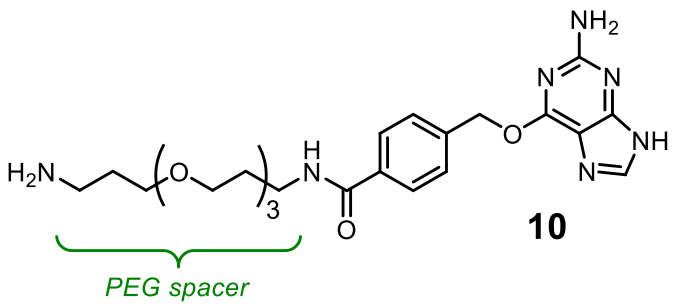

Figure 16: *Molecular structure of the first BG-linker target (**10**) in this study, incorporating a PEG spacer with terminal primary amine functionality.*

Our incorporation of a carbonyl group at the benzylic position of the BG moiety in compound **10** (**Figure 16**) allowed for greater versatility in linker design, as well as potentially activating the BG group for the S_N2 reaction during SNAP-tag conjugation. The latter being caused by increased electrophilicity of the benzylic position due to induction, in comparison to other reported BG-linkers with a methylene at this position. A simple BG-linker product from New England Biolabs, which lacks this carbonyl group, is presented in **Figure 17**, illustrating this subtle difference.

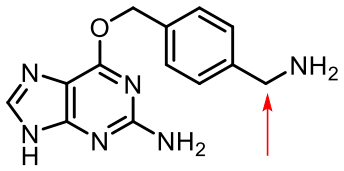

Figure 17: *The molecular structure of a simple BG-linker available from New England Biolabs.*

2.2 Synthesis of ADC-Precursors

2.2.1 Amide coupling strategy

Amide coupling in organic synthesis is necessitated by the presence of peptide (amide) functionalities in proteins, whereby amino and carboxy termini are condensed together. This reaction is widely incorporated in synthesis transformations, with a vast array of coupling agents having been developed to facilitate the fusion of reactants containing amine and carboxylic acid functionality.

Our first strategy to achieve the BG-linker (**10**) involved a Boc-protected precursor, which was synthesised in a linear sequence as outlined in **Scheme 1**.

In this synthesis, 4-hydroxymethylbenzoic acid (4-HMBA) was used as a bifunctional component of the BG-linker system, with its carboxylic acid functionality allowing for amide coupling with a mono-protected spacer, while the primary hydroxyl allowed for S_NAr reaction with an activated derivative of 2-amino-6-bromopurine.

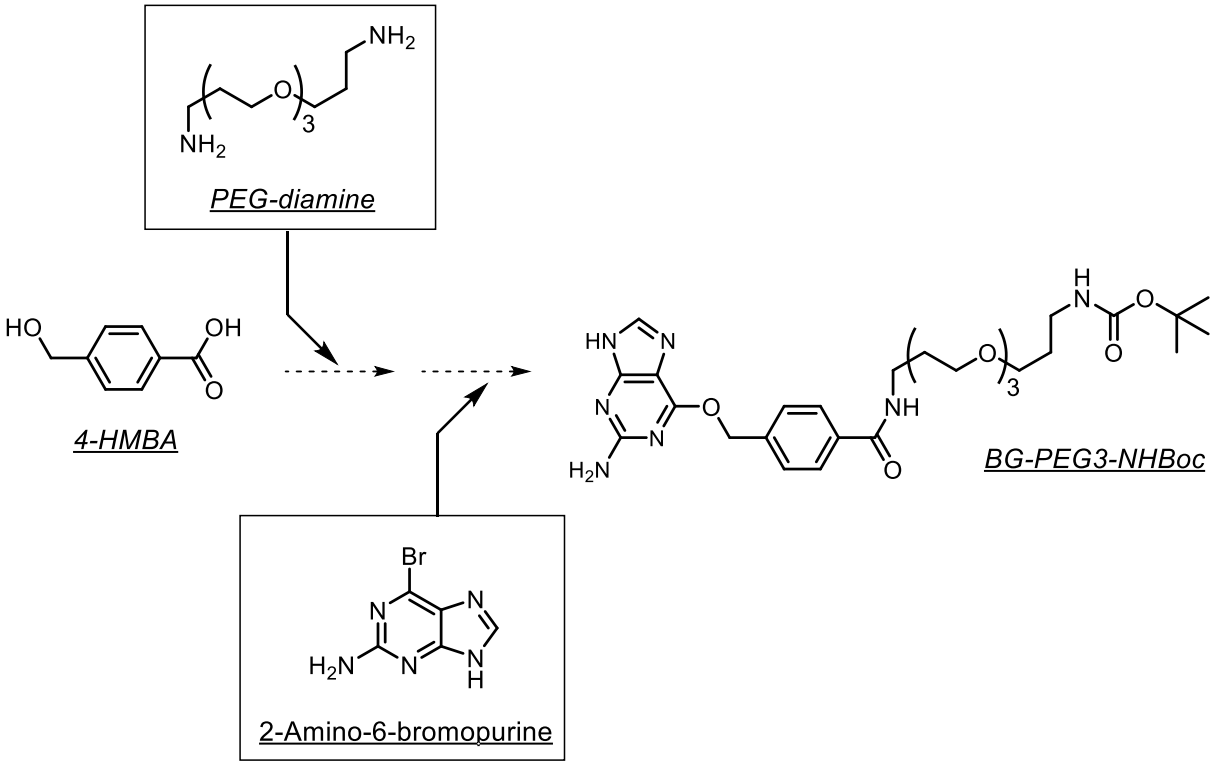

Scheme 1: *Synthetic scheme for the synthesis of a Boc-protected BG-linker precursor from starting materials 4-HMBA, PEG-diamine and 2-amino-6-bromopurine.*

The isolation of this Boc protected BG-linker was to be followed by its deprotection (**Scheme 2**), in order to yield a free amine for amide coupling with auristatin-F.

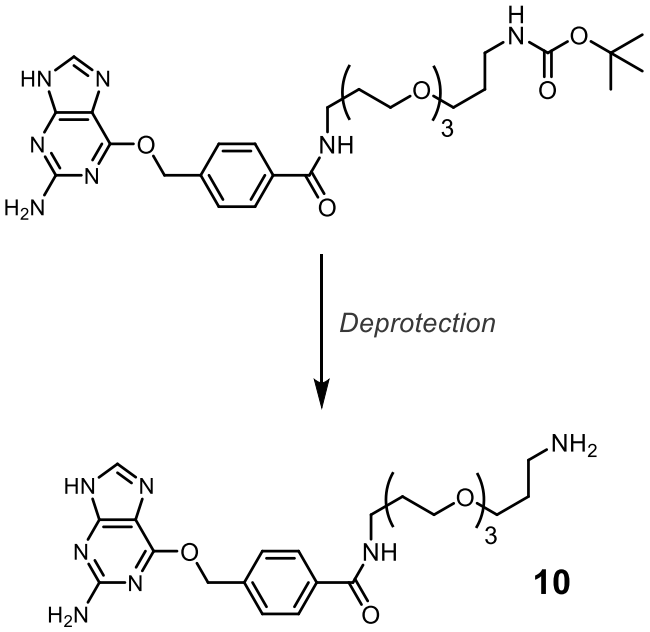

Scheme 2: *Final deprotection reaction to prepare for the amide coupling strategy for the BG-modification of auristatin-F from a Boc protected BG-linker.*

Unfortunately, Boc-deprotection failed to produce the required amine, in spite of exploring several methods such as standard TFA deprotection, HCl deprotection, the use of tetra-*n*-butylammonium fluoride (TBAF) and even thermal deprotection. In several of the experiments (at -20 °C) a single, more polar spot on TLC was produced and isolated, which upon characterisation by NMR spectroscopy indicated the loss of guanine functionality. Synthesis of the trifluoroacetamide equivalent of this linker system was also attempted, in order to pursue deprotection under mild basic conditions, but premature cleavage of this protecting group was observed early in the sequence.

These findings stimulated thoughts on a new strategy for coupling the BG-linker to auristatin-F, in which the introduction and usage of necessary functionality would be compatible with the BG group. This led to identifying an azide functionality in the spacer for use in a copper(I)-catalysed azide-alkyne cycloaddition (CuAAC) click reaction as a means for coupling the toxin. In addition, it was anticipated that the azide could be directly transformed into a primary amine (for achieving an amide coupling as before) via a Staudinger reduction reaction, which involves mild reductive conditions thought to be compatible with the BG group.

2.2.2 Click chemistry strategy

The term "click chemistry" has been defined by Sharpless and co-workers to encompass reactions which are modular, simple to perform, make use of benign solvent, do not create offensive by-products and are high yielding.[124] One such reaction that falls into this class is the Huisgen 1,3-dipolar cycloaddition, which produces 1,2,3-triazole ring systems from the reaction of alkyne and azide functional groups. This reaction was initially described to be performed under reflux, without catalysis, producing a 1:1 mixture of 1,4- (*anti)* and 1,5- (*syn*) regioisomers.[125] Developments in this reaction, especially by the application of copper(I)-catalysis, allowed for these reactions to be performed at ambient temperature, as well as for affording strictly *anti* products.[126] The latter has become known as CuAAC and is the form of click chemistry referred to in this study. **Scheme 3** depicts the two discussed variations, outlining the selectivity in product formation.

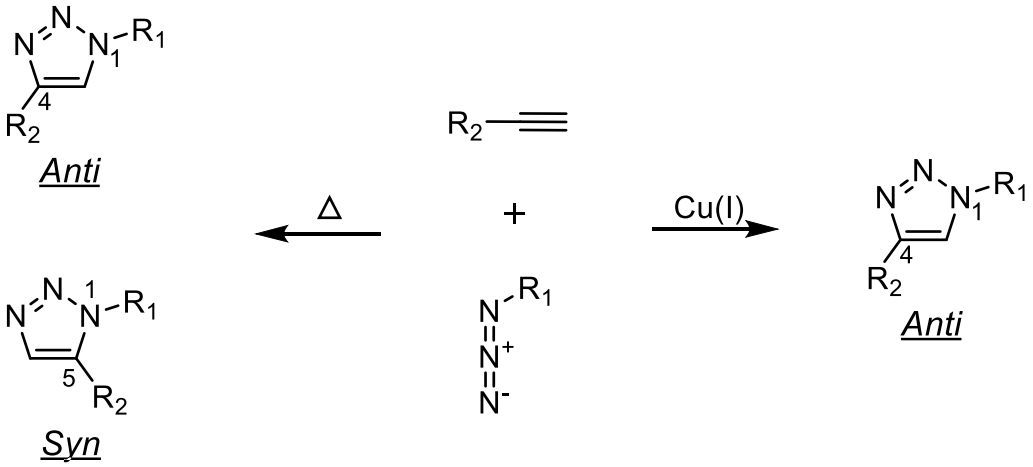

Scheme 3: *The comparison of triazole-forming click reactions of azides and alkynes via Cu(I) catalysis or heat, and the regioselective implications of each.*

CuAAC reactions have been utilised in many synthetic applications, including small molecule synthesis, macrocycle synthesis, diversification of natural products and in the synthesis of dendrimers and polymers.[127] Various methods exist for the introduction of Cu(I) into reaction environments and that used in this study was to introduce a catalytic Cu(II) species which was reduced to Cu(I) *in situ* by the addition of sodium ascorbate to the reaction mixture.

To enable click chemistry opportunities, it was necessary to redesign the BG-PEG3-NHBoc linker to incorporate either azide or alkyne functionality. Functionalisation of the spacer with azide character prior to its installation was considered to be the most efficient approach, as it would allow for the majority of the prior synthesis strategy to be conserved. The introduction of alkyne functionality to auristatin-F was also preferred over the azido alternative, as this was envisioned to be easily achievable by amide coupling with an alkynyl amine such as propargylamine. This would ultimately allow for a click reaction as the pinnacle transformation in affording an ADC-precursor, which would incorporate a triazole ring. The envisioned azido BG-linker synthesis target (**9**) is displayed in **Figure 18**.

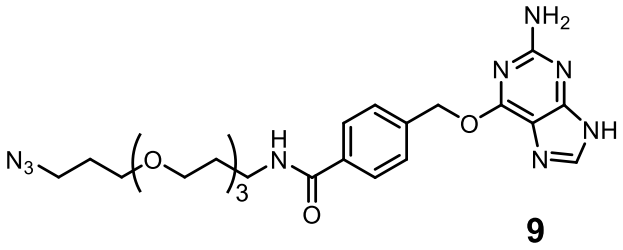

9

BG-PEG3-N_3

Figure 18: *The chemical structure of the azido BG-linker target to be used for CuAAC click chemistry convergence with an alkyne functionalised auristatin-F derivative.*

The synthesis to obtain the azido BG-linker commenced with silylation of the benzylic hydroxyl of commercially available 4-HMBA, as portrayed in **Scheme 4**.

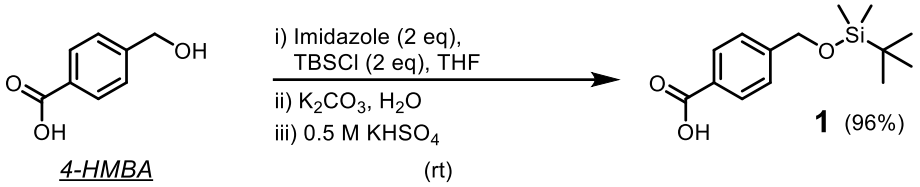

4-HMBA

Scheme 4: *Silyl ether protection of 4-HMBA to afford **1**.*

This reaction is postulated to proceed via imidazole acting as a silyl transfer agent by first reacting with *tert*-butyldimethylsilyl chloride (TBSCl) to form a quaternised and electrophilic *N*-silyl intermediate which rapidly transfers a silyl group to the primary alcohol oxygen. The addition of two equivalents of TBSCl was used to account for any silylation of the carboxyl group, thereby ensuring complete protection of the benzylic hydroxyl group. Once the complete conversion of starting material was observed by thin layer chromatography (TLC), the resulting imidazolium salts were removed by filtration and the reduced filtrate taken up in THF:H_2O to which potassium carbonate (K_2CO_3) was added in order to hydrolyse any TBS ester formed from the reaction of the acid hydroxyl. This was followed by the addition of potassium bisulfate ($KHSO_4$), resulting in an acidic environment to protonate the carboxylate ion formed from the base hydrolysis, without disturbing the acid-sensitive TBS group. The resulting reaction mixture was extracted with DCM and subjected to aqueous washings in order to remove any salts from the organic phase, which was dried and concentrated to yield the product **1** without the need for chromatography, as a colourless crystalline solid, in 96% yield. The spectroscopic data of **1** matched that presented in literature and a ^{1}H NMR spectrum generated in this study is displayed in **Figure 19**.[128]

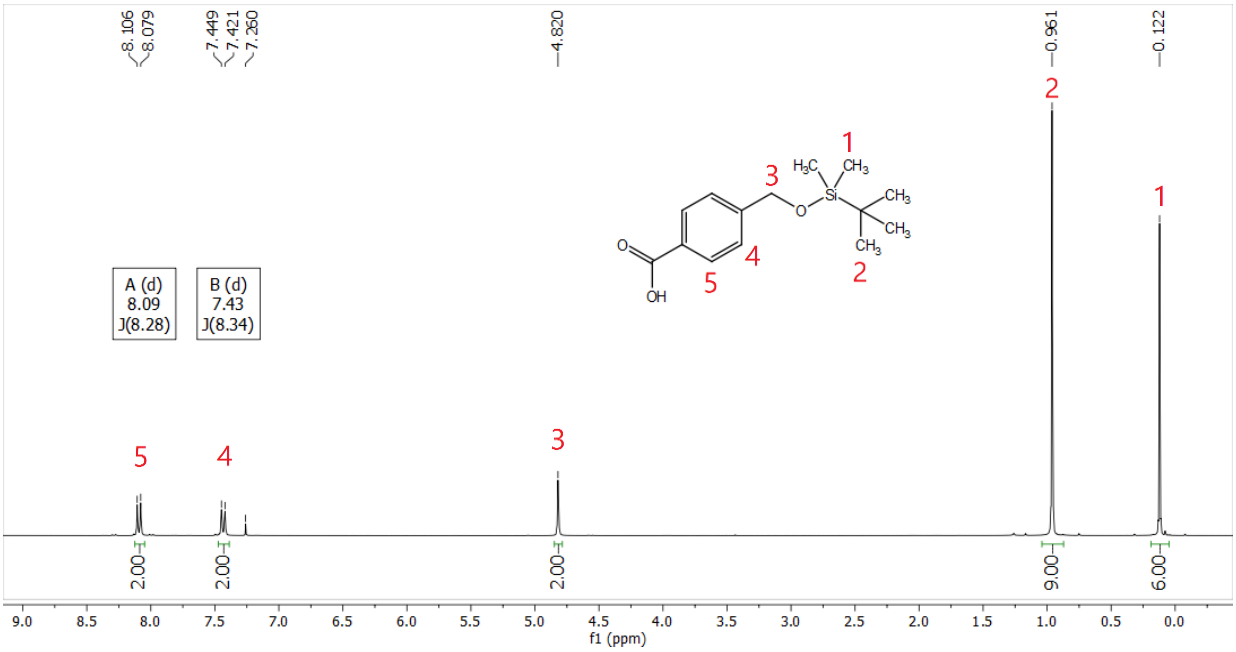

Figure 19: *^{1}H NMR spectrum of **1**, recorded in $CDCl_3$.*

It was important at this point to take note of key resonances that would be conserved throughout the synthesis, such as the benzylic methylene singlet at 4.82 ppm and the AB doublet pair at 7.43 and 8.09 ppm representing the aryl hydrogens. The ^{1}H NMR spectrum also displayed 9H and 6H singlet resonances at 0.12 and 0.96 ppm, respectively, representing the *t*-butyl and dimethyl protons of the TBS protecting group. The successful synthesis of **1** was further supported by its ^{13}C NMR spectrum, in which the nine carbon resonances expected on symmetry grounds were observed, of the 14 carbons in total. The chemoselectivity of the protection, in terms of preferential silylation of the alcohol hydroxyl group could not be confirmed spectroscopically, but was supported by a successful coupling in the next step, which was only mechanistically possible via the presence of a free carboxylic acid hydroxyl group.

The next step in the sequence involved converting **1** into its succinimidyl activated ester (**Scheme 5**), in order to prepare for amide coupling with the PEG-spacer, in which dicyclohexylcarbodiimide (DCC) was used as a coupling agent and 4-dimethylaminopyridine (DMAP) as an acyl transfer agent.

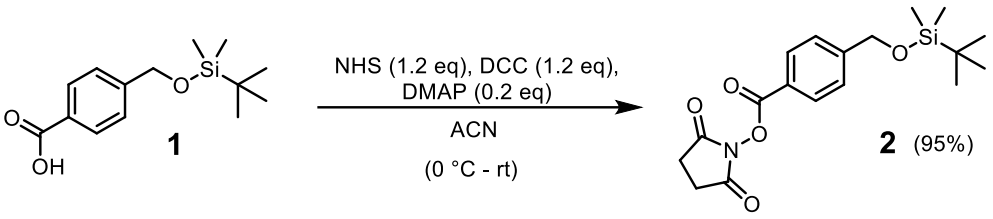

Scheme 5: *Activation of **1** by the formation of its succinimidyl ester derivative (**2**).*

A mechanistic view of this reaction can be seen in **Scheme 6**, in which *N*-hydroxysuccinimide (NHS) acts as the nucleophile. The reaction proceeds via an *O*-acylisourea intermediate, which is substituted by DMAP to offer an excellent leaving group in the S_NAc substitution with the NHS hydroxyl group.[129] The incorporation of DMAP also serves to restrict rearrangement of the *O*-acylisourea to a terminal *N*-acylurea by-product.

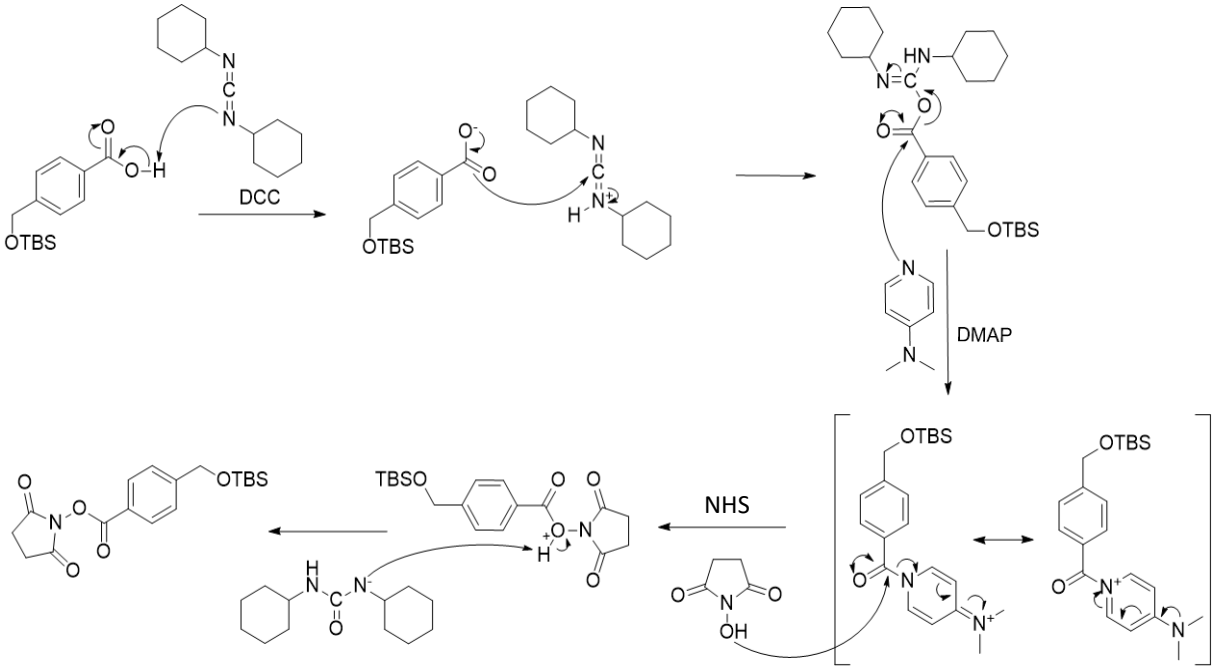

Scheme 6: *Mechanism for the reaction of **1** with NHS, DCC and DMAP.*

The reaction was carried out at room temperature and subsequently chilled at -20 °C for 3 hours, before filtering off the dicyclohexylurea (DCU) solid formed as a by-product in the reaction. The filtrate was concentrated and purified by column chromatography directly to yield 94% of **2**, as a pearly white crystalline material.

The ^{1}H NMR spectrum of **2** displayed a new singlet resonance at 2.90 ppm, with respect to that of **1**, integrating for four hydrogens and corresponding to the enantiotopic succinimide methylene protons. The presence of the succinimidyl ester was further confirmed by its ^{13}C NMR spectrum, which correctly displayed 11 distinct resonances, two more than for **2**, representing the additional unique carbonyl and methylene

carbon atoms of the succinimide ring. The IR spectrum also displayed a new absorption at 1741 cm^{-1}, typical of a carbonyl stretch for a cyclic imide, providing further evidence of a successful reaction.

Before introduction of the spacer could ensue, various derivatisations of the PEG3-diamine starting material were necessary. These transformations were initiated by the selective Boc-protection of one of the amine functional groups, as depicted in **Scheme 7**.

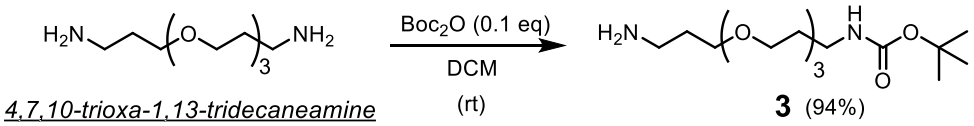

4,7,10-trioxa-1,13-tridecaneamine — **3** (94%)

Scheme 7: *Boc protection of 4,7,10-trioxa-1,13-tridecaneamine to form **3**.*

This reaction proceeded via a standard S_NAc reaction mechanism, whereby the nucleophilic amine reacted with the electrophilic carbonyl carbon of the Boc_2O thereby displacing CO_2 and *t*-butanol. The large excess of PEG3-diamine was used to minimise the probability of bis-protection, which would ultimately complicate purification and lead to a lower yield with respect to Boc_2O. After addition of Boc_2O, the reaction was complete within 3 hours as determined by the disappearance of Boc_2O and the formation of a less polar spot upon TLC analysis. Due to the lack of UV-chromophores, TLC plates used in reaction monitoring and purification were visualised with ninhydrin spray. The reaction mixture was reduced *in vacuo* and the residue purified directly by column chromatography, without an aqueous work-up, to afford **3** as an amber oil, in 94% yield.

The successful introduction of the Boc group was supported by an absorption at 1694 cm^{-1}, typical of a carbamate, in the IR spectrum of **3** (**Figure 20**).

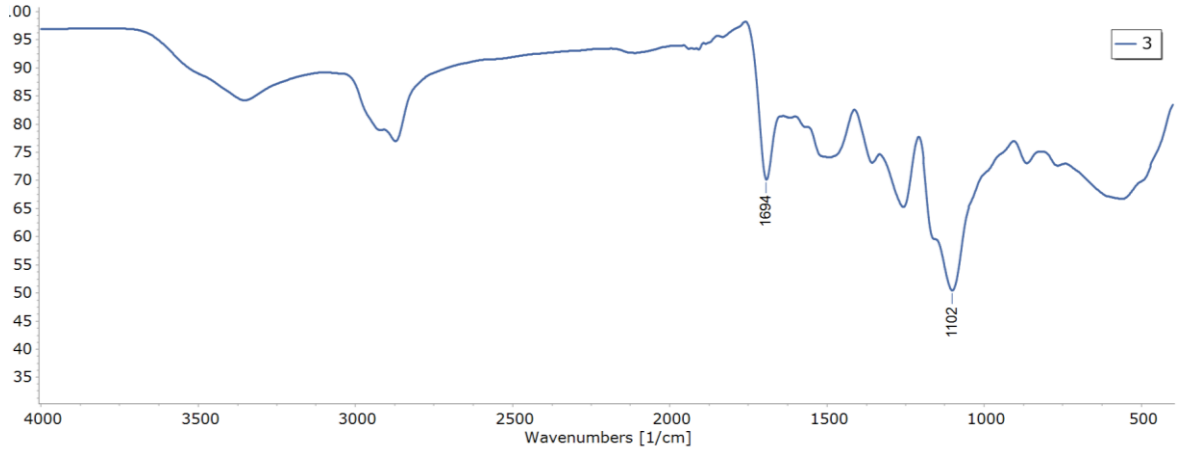

Figure 20: *IR Spectrum of **3**, with the main diagnostic absorptions highlighted.*

The ^{13}C and ^{1}H NMR spectral data also agreed with that reported in the literature, further corroborating the synthesis of **3.**[130] Once again it was important to take note of the characteristic ^{1}H NMR resonances of **3** for recognition purposes, in view of conservation of the spacer throughout the synthesis. For this purpose, an assigned ^{1}H NMR spectrum of **3** is displayed in **Figure 21**.

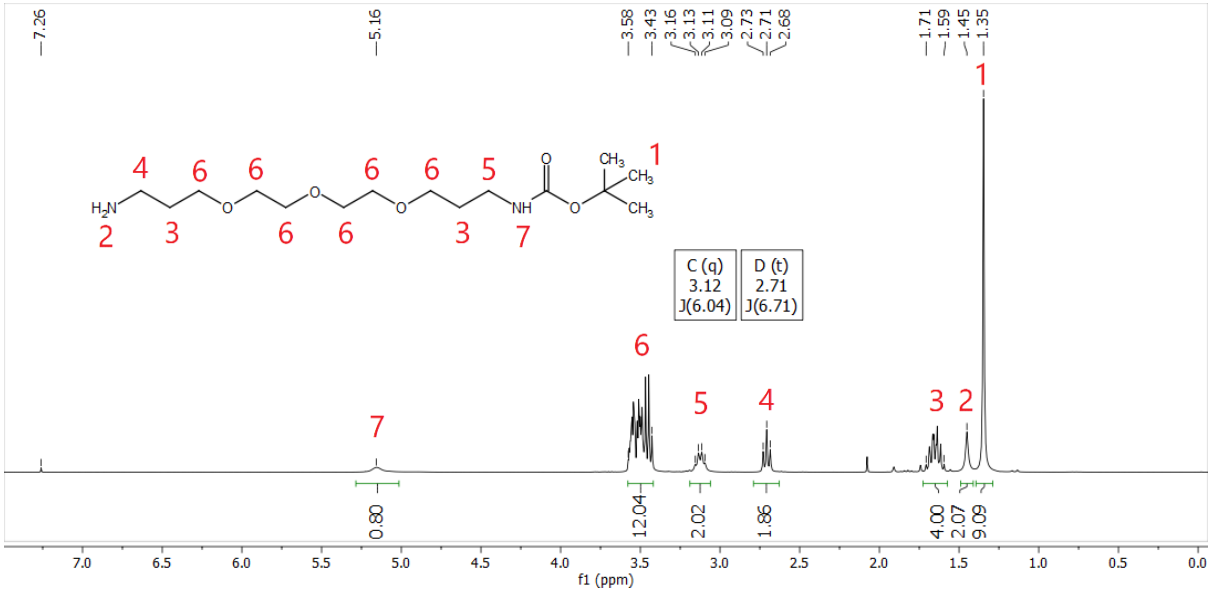

Figure 21: *^{1}H NMR spectrum of **3**, recorded in $CDCl_3$.*

The most significant signal confirming this successful transformation was the 9H singlet at 1.35 ppm, representing the Boc *t*-butyl hydrogens, with the integration value supporting a successful mono-protection. The broad 2H singlet observed at 1.45 ppm corresponded to the terminal primary amino group protons, while the broad 1H singlet at 5.16 ppm could be assigned as the carbamate NH proton. The PEG methylene hydrogens appeared as multiplets around 1.65 and 3.51 ppm as well as a triplet and an apparent quartet resonance with shifts of 2.71 and 3.12 ppm, respectively, for H-4 and H-5 adjacent to the nitrogen atoms. The ^{13}C NMR spectrum displayed only 12 distinct resonances of the expected 13, bearing in mind the magnetic equivalence of the *t*-butyl methyl carbons. The carbon atoms adjacent to the oxygen at the centre of the PEG spacer were not expected to be in vastly different magnetic environments and could likely have appeared as one signal, accounting for the 12 resonances.

The next transformation for converting the terminal amino group into an azide involved a diazo transfer reaction, which was achieved according to a literature procedure and is presented in **Scheme 8**.[131]

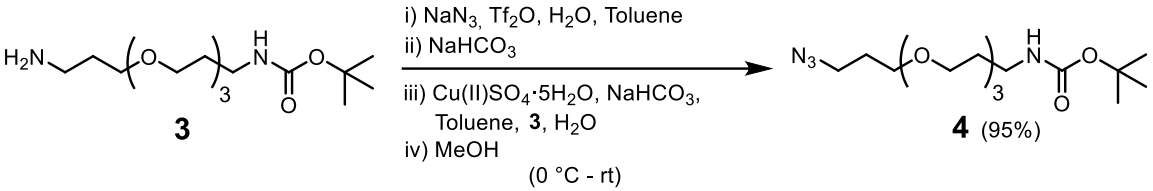

Scheme 8: *Diazo transfer reaction on* ***3****, to afford the azido-PEG3-Boc spacer (****4****).*

This reaction involved the *in situ* preparation of trifluoromethanesulfonyl (triflyl) azide as the diazo transfer reagent from the reaction of sodium azide (NaN_3) and triflic anhydride at 0 °C. Triflic anhydride has strong electrophilic character, allowing for a substitution reaction to occur at the sulfur centre by the nucleophilic attack of the azide anion, thereby liberating triflic acid and triflyl azide. Triflyl azide has been reported to cause explosions in the absence of solvent and when in contact with DCM, due to the formation of explosive substitution products, which is curbed in the literature by the use of toluene as the reaction solvent, in conjunction with low temperature conditions and quenching.[131] The triflic acid was neutralised to sodium triflate with sodium bicarbonate ($NaHCO_3$), which migrates to the aqueous layer, allowing for the reagent to be purified by extraction with toluene. The triflyl azide toluene extracts were added directly to an aqueous solution of **3**, $Cu(II)SO_4{\cdot}5H_2O$ and $NaHCO_3$, before the addition of MeOH to yield a homogenous solution. The mechanism of transition metal-catalysed diazo transfer reactions with triflyl azide is postulated to occur via amine complexation to the metal centre and subsequent nucleophilic attack of the amine on triflyl azide reagent, which upon deprotonation yields a tetrazine species able to undergo a reverse [3 + 2] cycloaddition to yield the target azide.[132] The resulting reaction mixture initially adopted a light blue colour which transitioned to green coinciding with the reaction completion as determined by TLC analysis. Compounds bearing azide functional groups were easily identified during TLC analysis by initially treating the plate with triphenylphosphine (PPh_3) in DCM and subsequent staining with ninhydrin to yield a deep red spot.[133] Once complete, the volatiles were removed *in vacuo* and the resulting aqueous solution extracted with DCM, before purification by column chromatography to yield **4** as a colourless oil, in 95% yield.

The ^{13}C and ^{1}H NMR spectral data of **4** agreed with that reported in the literature and, as expected, differed only slightly from that of **3**.[130] Compound **4**'s ^{13}C NMR spectrum comprised 12 distinct resonances again, while its ^{1}H NMR spectrum differed from that of **3** only in that it lacked the primary amine 2H singlet previously observed at 1.45 ppm. IR spectroscopy was also performed for **4**, which importantly revealed the

appearance of an azide stretch at 2095 cm^{-1} - the spectrum of **4** is compared to that obtained for **3** in **Figure 22**.

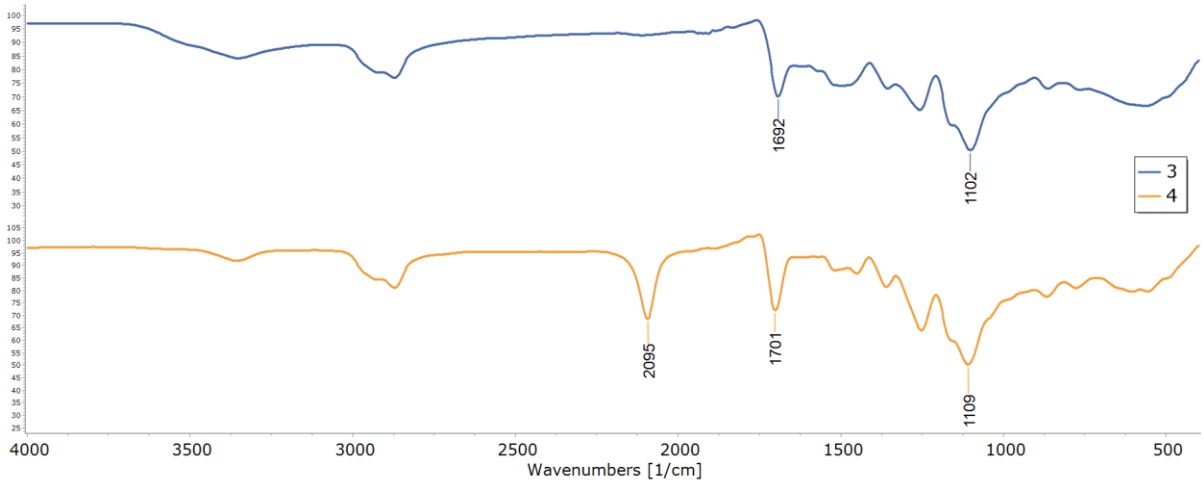

Figure 22: *IR Spectra of **3** and **4**, highlighting key diagnostic absorptions.*

The final transformation of the PEG spacer was the deprotection of the Boc-protected amine, as depicted in **Scheme 9**.

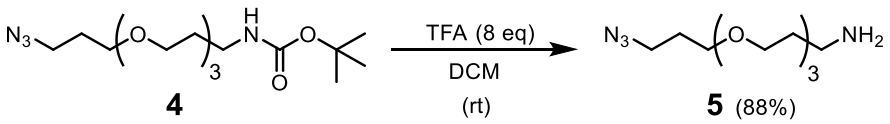

Scheme 9: *Boc deprotection of **4**, to yield the azido-PEG3 spacer (**5**).*

This transformation was achieved as per standard conditions with TFA (8 eq) in anhydrous DCM at room temperature. The progress of the reaction was followed by the disappearance of **4** on TLC, and the appearance of a more polar spot. Upon reaction completion, the reaction was purified directly by flash column chromatography to afford **5** as an amber oil, in 88% yield.

The ^{13}C NMR, ^{1}H NMR and IR spectral data of **5** agreed with that reported in the literature, in which the ^{13}C NMR spectral data displayed 10 unique resonances, accounting for all 10 of the carbon atoms.[130] The ^{1}H NMR spectrum retained the expected PEG resonances, as highlighted in **Figure 21** for compound **3**, and lacked the singlet for the Boc *t*-butyl hydrogen atoms.

Upon inspection of the IR spectrum, the azide stretching frequency was seen to be conserved, while that of the carbonyl stretching frequency was absent. The IR spectral data of **5**, highlighting the retained azide stretching frequency at 2094 cm^{-1}, is displayed in **Figure 23**.

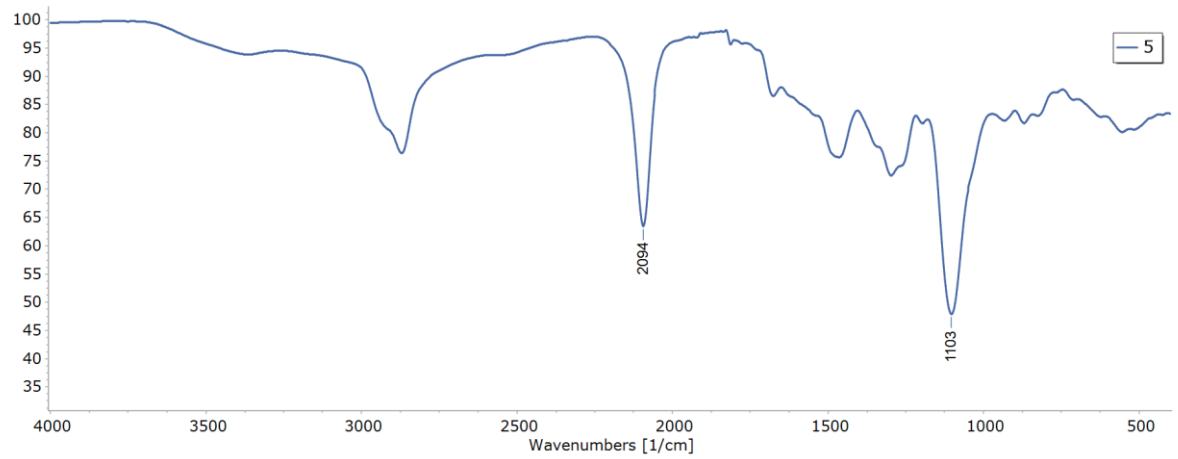

Figure 23: *IR spectrum of **5**, highlighting the retained azide functionality.*

An amide coupling reaction was now possible between the primary amine of **5** and the activated ester of **2**, which was undertaken as conveyed in **Scheme 10**.

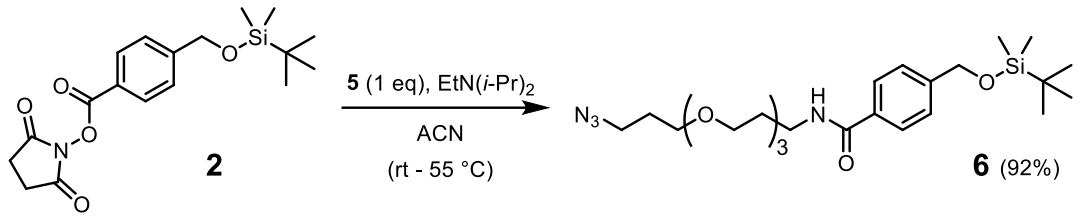

Scheme 10: *Amide coupling reaction of the activated ester (**2**) with the azido-PEG3 spacer (**5**).*

Since the acid was activated for nucleophilic attack in the form of a succinimidyl ester, there was no need for the addition of a coupling reagent in this transformation - a reaction mechanism of which is depicted in **Scheme 11**.

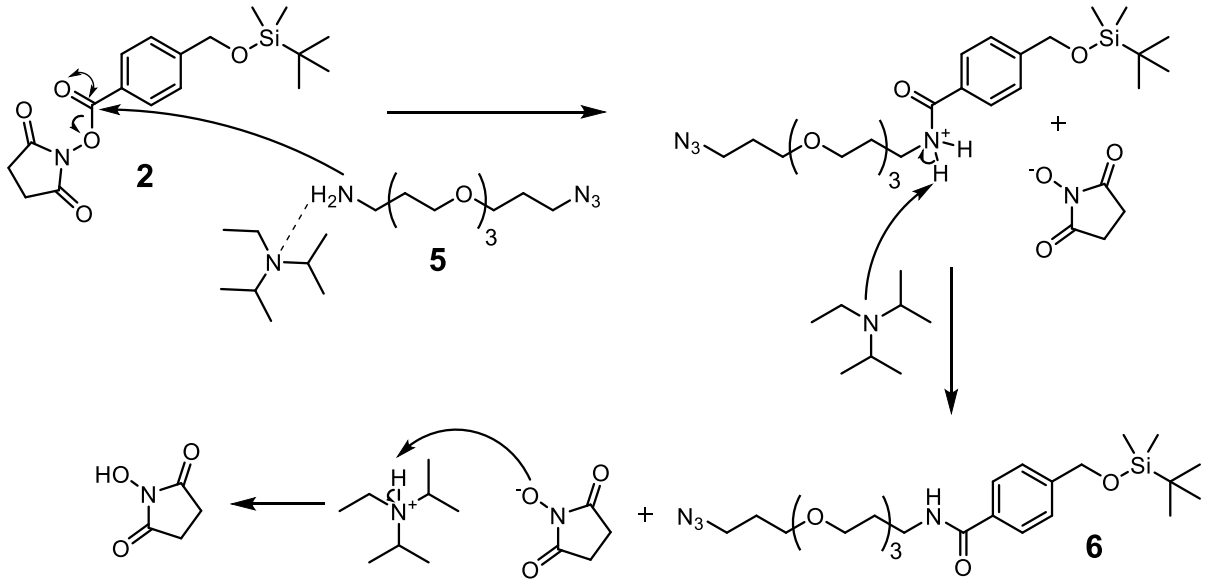

Scheme 11: *Reaction mechanism for the amide coupling reaction of **2** and **5**.*

The transformation was facilitated by *N,N'*-diisopropylethylamine (DIPEA), and progress was monitored by TLC, in which the intensity of NHS as an elimination product could be followed as an indication for reaction progress, along with the disappearance of starting materials. For isolation, the crude mixture was adsorbed onto silica *in vacuo* and purified directly by column chromatography to afford **6**, as a colourless oil, in 92% yield. This compound has not previously been reported in the literature and thus full characterisation was undertaken, for which the ^{1}H NMR spectrum for **6**, along with structural assignments, is displayed in **Figure 24**.

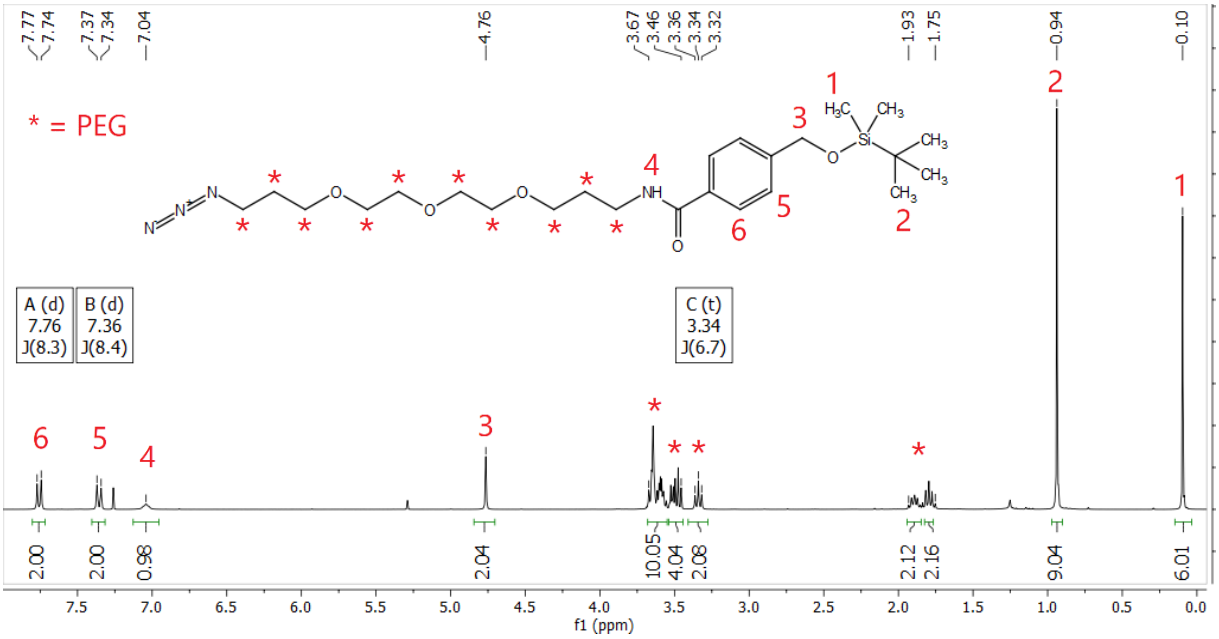

Figure 24: *^{1}H NMR spectrum of **6**, recorded in $CDCl_3$.*

The structural features originating from **2** were clearly present in the combination product **6**, such as singlet resonances at 0.10 ppm (6H) and 0.94 ppm (9H) confirming the retention of the TBS protecting group, and a singlet at 4.76 ppm (2H) representative of the benzylic methylene hydrogens. Further downfield, the aryl hydrogens were represented by the AA'BB' doublet pair at 7.36 and 7.76 ppm. Those signals originating from **5**, namely the PEG methylene hydrogens, were present between 1.5 and 4.0 ppm and the amide secondary amine was represented by a broad singlet (1H) at 7.04 ppm. The ^{13}C NMR spectrum comprised 18 distinct resonances representing the 24 carbon atoms in the molecule, which was expected due to the equivalence of the TBS *t*-butyl and dimethyl carbons, those of the benzene ring, as well as the two carbons adjacent to the central oxygen of the PEG spacer. Further evidence for the successful preparation of **6** was obtained in the form of LC-MS analysis, in which a major peak was observed at an *m/z* value of 495.2 which is in line with the calculated value (495.29) for its $[M+H]^+$ ion. Finally, an IR spectrum of the isolated compound

displayed notable absorptions at 1092 cm^{-1}, 1640 cm^{-1} and 2096 cm^{-1}. The absorption at 1092 cm^{-1} was present in the region characteristic of saturated aliphatic ether C-O-C asymmetric stretches, which supplied additional evidence for presence of the PEG spacer, while that at 1640 cm^{-1} was assigned to the secondary amide as a C=O stretch. As with the spectra obtained for PEG spacer derivatisation, the peak at 2096 cm^{-1} represented the azide stretching frequency. The IR spectrum for compound **6** is displayed in **Figure 25**, with key absorptions highlighted.

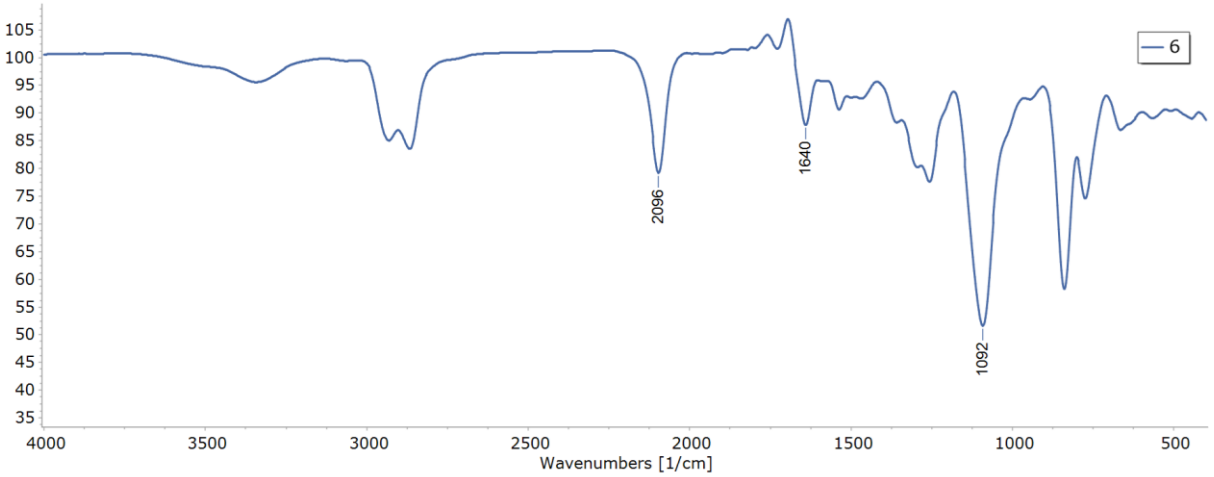

Figure 25: *IR spectrum of **6**, with key absorptions highlighted.*

It was now time to prepare for the installation of BG functionality, which first involved deprotection of the TBS group, a synthetic scheme of which is presented in **Scheme 12**.

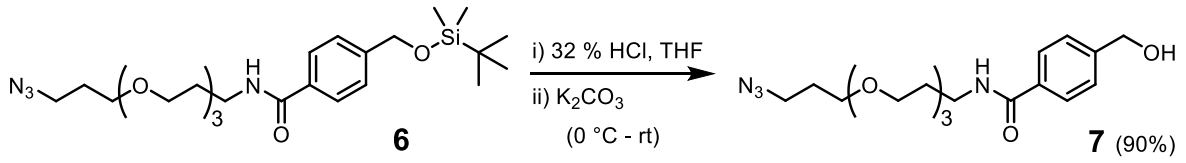

Scheme 12: *TBS deprotection of **6** to yield the free hydroxyl derivative (**7**).*

The deprotection of **6** was achieved under acidic conditions using 32% HCl, at 0 °C, with subsequent warming of the mixture to room temperature. The reaction proceeds via protonation of the ether oxygen followed by substitution at silicon by water, thereby displacing the free hydroxyl. The reaction progress was followed by the disappearance of **6** on TLC, and the formation of a more polar spot. The reaction was neutralised by the addition of K_2CO_3 and purified directly by column chromatography to yield **7**, in 90 %, as a colourless oil.

This compound has not previously appeared in the literature and as a result it was fully characterised. Similarly to that of **6**, the ^1H NMR spectrum displayed key resonances

such as the range of PEG hydrogens (20H) present between 1.5 and 4.0 ppm, the benzylic methylene 2H singlet at 4.71 ppm, the amide hydrogen as a broad 1H singlet at 7.14 ppm and the AA'BB' doublet pair at 7.37 and 7.74 ppm. However, the signals representing the TBS group in compound **6** were absent, being replaced by a broad 1H singlet at 2.44 ppm for the hydroxyl hydrogen. The ^{13}C NMR spectrum displayed 16 distinct resonances, accounting for the 16 non-equivalent carbon atoms in the molecule. IR spectroscopy was also performed, allowing for comparison with the IR spectral data obtained for **6**, which is presented in **Figure 26**.

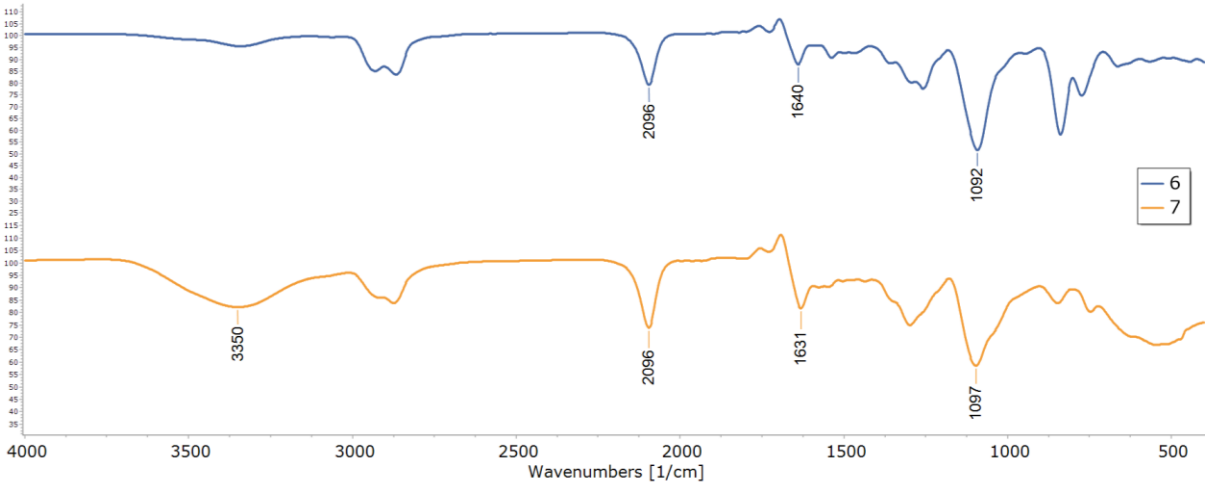

Figure 26: *IR spectrum of **6** in comparison to that of **7**, with key absorptions labelled.*

Notably, the previously highlighted peaks representing the azido, PEG and amide units were conserved and a broad peak was observed at 3350 cm^{-1}, characteristic for an O-H stretch. As a final measure of structure confirmation, the compound was admitted to LC-MS analysis, in which a major peak was observed at an *m/z* value of 381.1 which is in line with the calculated value (381.21) for the proton adduct of **7** as an $[M+H]^+$ ion.

Before the S_NAr reaction to incorporate guanine could ensue, the guanine electrophile was activated with *N*-methylpyrrolidine (**Scheme 13**), as per a literature procedure.[134]

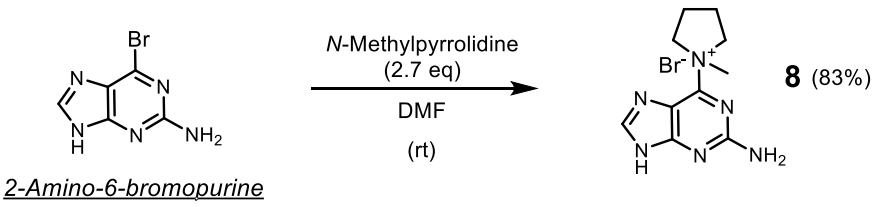

Scheme 13: *Activation of 2-amino-6-bromopurine to yield NMP-guanine (**8**).*

This reaction proceeds via an S_NAr mechanism, in which the pyrrolidine nitrogen attacks at the bromine-bearing carbon, resulting in expulsion of a bromide ion to yield **8**. Acetone was added after the reaction had run its course, allowing for the precipitation of the reaction product, which was collected by filtration to yield the product, in 83% yield, as a pastel white solid. It must be noted that the dimethylformamide (DMF) was required to be freshly distilled over calcium hydride and stored under an inert atmosphere over activated molecular sieves prior to use, as the presence of any water in the reaction resulted in significantly lower yields.

The ^{1}H NMR spectrum of compound **8** is presented in **Figure 27** and was in agreement with that reported in the literature.[134]

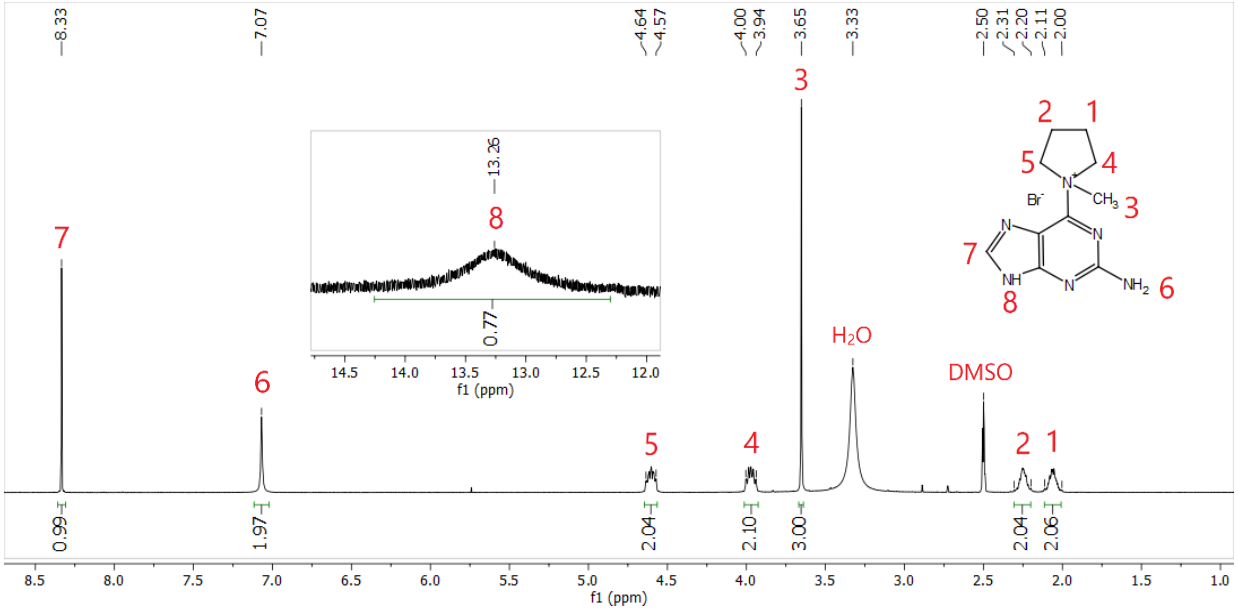

Figure 27: *^{1}H NMR spectrum of **8**, recorded in DMSO-d_6.*

The pyrrolidine ring gave four 2H multiplet methylene signals at 2.05, 2.25, 3.97 and 4.60 ppm and supports quaternization of the pyrrolidine nitrogen. This is due to the methylene hydrogens all becoming diastereotopic, rendering them magnetically non-equivalent as opposed to the two multiplets that would be observed for a pyrrolidine ring that is sp^2-hybridised. In addition, a sharp 3H singlet was present at 3.65 ppm, confirming the introduction of a methyl group, as well as a 2H singlet at 7.07 ppm accounting for the primary amino group at the 2-position. Finally, a 1H singlet at 8.33 ppm was assigned to the guanine methine hydrogen, while a broad 1H singlet was observed downfield at 13.26 ppm accounting for the imidazole NH. In the ^{13}C NMR spectrum of **8**, a total of eight resonances were observed for the 10 carbons in the molecule as a result of the pyrrolidine ring symmetry and free N-C_{aryl} rotation.

With **8** in hand, it was possible to undertake the S_NAr reaction with **7**, in order to yield the azido BG-linker system **9**, a reaction scheme of which is presented in **Scheme 14**.

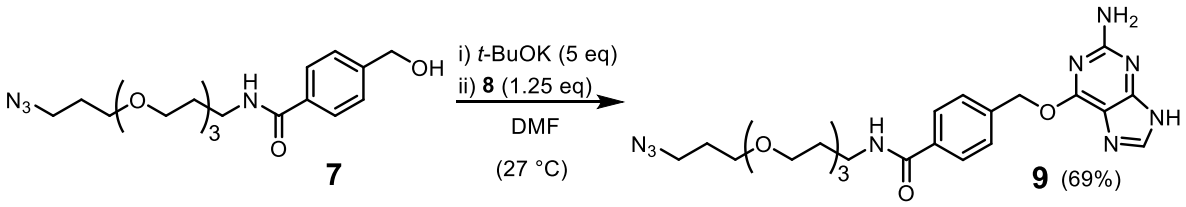

Scheme 14: *Guanine introduction by the S_NAr reaction of **7** and **8**.*

The reaction commenced with the deprotonation of the hydroxyl group of **7**, which was achieved in anhydrous DMF with potassium *tert*-butoxide (*t*-BuOK) as base, by allowing the reaction to stir for thirty minutes or until the solution had adopted a deep orange colour from an initially clear solution, deemed to indicate full deprotonation. Thereafter, compound **8** (1.25 eq) was added and the reaction allowed to proceed at 27 °C, until the starting material was no longer visible upon TLC analysis. The reaction was complete within 4 hours, after which the DMF was removed *in vacuo* and the residue purified directly by column chromatography to afford **9** as a waxy, colourless solid in 69% yield.

This reaction required substantial optimisation in order to achieve appreciable and reproducible yields. As with the guanine activation reaction, extremely dry conditions were necessary in order to achieve complete conversion. The choice of base was also an important factor, as in prior experiments sodium hydride was used, which resulted in a considerably longer reaction time (48 hours) and lower yields. Similarly, the chromatographic purification of **9** also posed a challenge as one particular side-product was consistently produced with very similar polarity to the product. Chromatographic separation was achieved by adhering to a low polarity mobile phase during separation and reducing fraction size appropriately.

This compound has not previously been reported in the literature and thus full characterisation was performed via ^{1}H NMR, ^{13}C NMR, IR spectroscopy and LC-MS analysis. The ^{1}H NMR spectrum (**Figure 28**) was indispensable for structure elucidation, as it was possible to identify resonances correlating with both of the starting materials, and provided diagnostic signals for later.

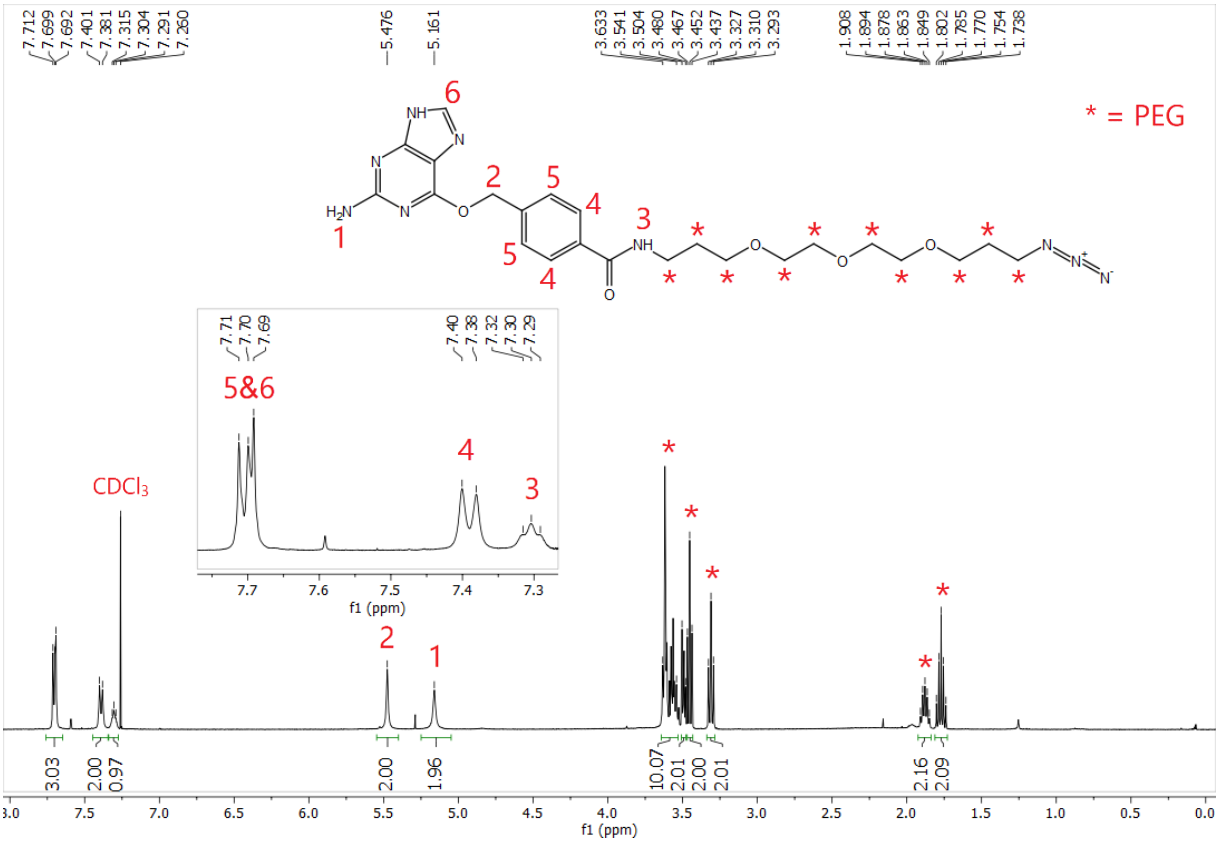

Figure 28: *^{1}H NMR spectrum of **9**, recorded in $CDCl_3$.*

The maintenance of the PEG spacer was evident by virtue of upfield resonances integrating for 20 hydrogens between 1.5 and 4.0 ppm, and two 2H singlet resonances were observed at 5.16 and 5.48 ppm accounting for the guanine primary amino group and the benzylic methylene hydrogens, respectively. The AA'BB' doublet system was seen to be present in the aromatic region and the methine hydrogen resonance of the guanine imidazole (H-6) was identified, embedded in the downfield doublet, at 7.70 ppm. Slightly upfield was a broad 1H triplet for the amide. An important diagnostic signal for future purposes was the benzylic methylene signal, which appeared at around 5.5 ppm (from around 4.7 ppm in compounds **1**, **2**, **6** and **7**). This deshielding was due to an electron-withdrawing inductive effect arising from n-pπ resonance between the heteroaromatic ring and oxygen. Only 17 distinct resonances were present in the ^{13}C NMR spectrum of the 21 that were expected, which was attributed to a slow relaxation of the four quaternary carbons of the guanine ring. The compound was also admitted to LC-MS, giving an *m/z* value of 514.1 which is in line with the calculated value of 514.25 for its $[M+H]^+$ ion. Further data was generated for this compound in the form of IR spectroscopy, the spectrum of which is displayed in **Figure 29**, compared to that obtained for **8** to illustrate absorptions resulting from the guanine ring.

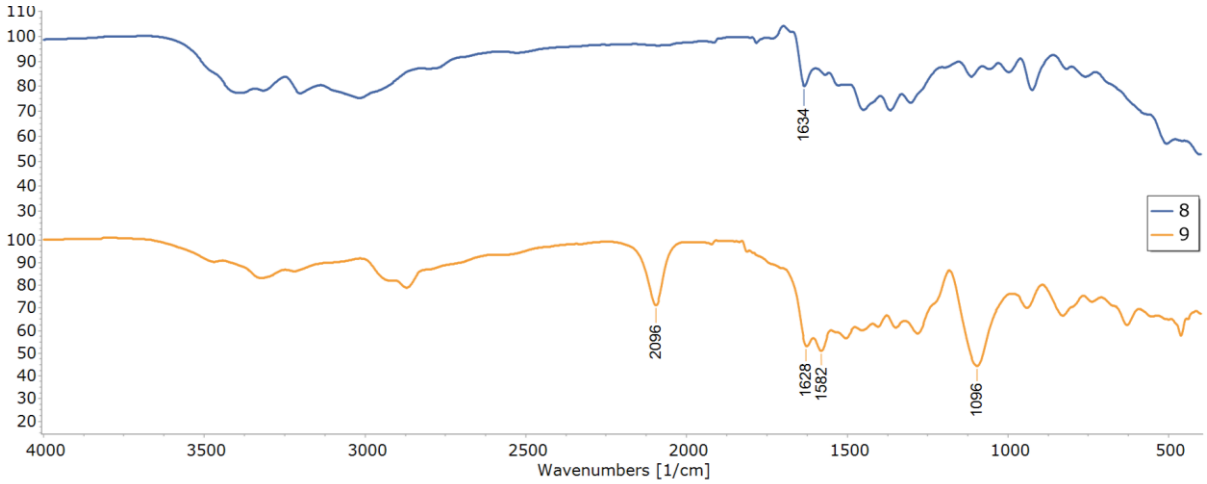

Figure 29: *IR spectrum of **9** in comparison with that of **8**, with characteristic absorptions labelled.*

Notably, the previously reported peaks representing the azide functional group, as well as the aliphatic ether PEG chain, were still present at 2096 cm^{-1} and 1096 cm^{-1}, respectively. On comparison with the spectral output from **8**, a series of absorptions in the range of 1300 cm^{-1} to 1700 cm^{-1} were conserved in the product, for the guanine ring.

Finally, to prepare for the CuAAC reaction with **9**, the derivatisation of MMAF was undertaken, involving the reductive methylation of its N-terminus (**Scheme 15**), following a method provided by a collaborator of the Barth academic group (Dr Wolfgang Richter of Tube Pharmaceuticals).

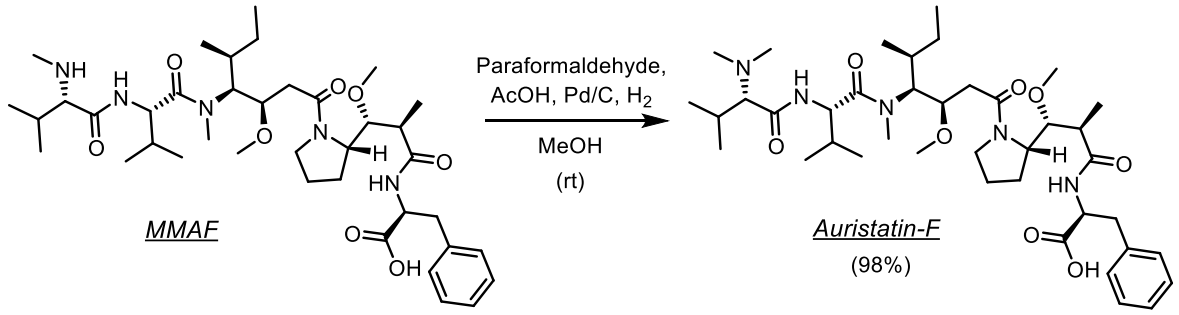

Scheme 15: *Reductive alkylation of the MMAF N-terminus to yield auristatin-F.*

Owing to its toxicity, extreme caution was employed when handling both MMAF and subsequent products containing the cytotoxin, with special attention focused on waste containment concerning the procedures carried out with these substances.

The reaction in question involved dissolving MMAF in anhydrous methanol, completely removing air by degassing with argon, before adding acetic acid, paraformaldehyde

and the heterogenous palladium-on-carbon (Pd/C) catalyst. This was followed by introducing hydrogen gas through a balloon attached to the reaction vessel, under which the reaction was kept throughout its progression. The reaction involves a variation of the Eschweiler-Clarke reductive amination reaction, in which the intermediate iminium ion is reduced by a hydride on the metal surface resulting from the oxidative addition of hydrogen gas onto the Pd/C catalyst. TLC studies for monitoring purposes proved to be problematic as the tertiary amide product had a very similar R_f to the starting secondary amine, both being relatively polar. In addition, they were both poorly UV-active (in spite of the presence of a phenyl ring) and showed poor reactivity towards spray reagents (ninhydrin and anisealdehyde). The lack of UV-activity also posed challenges for further analysis by HPLC-UV and LC-MS, as both of these instruments, within our direct access, relied on UV detectors for their respective outputs. After some experimentation, it was found that more highly concentrated TLC loading accompanied by anisaldehyde spray allowed for visualisation, to an extent. As a result, the reaction was allowed to proceed for 60 hours as opposed to the suggested 24 hours, after which the reaction mixture was filtered through Celite and the filtrate reduced *in vacuo* in order to yield the product as a colourless crystalline material, in 98% yield. This was not subjected to column chromatography, in accordance with the literature, so an analytical procedure was developed involving subjecting a small portion to Boc-protection conditions, anticipating that any residual starting secondary amine would be Boc-protected, and show up on TLC as a less polar spot. In the event, no additional products were observed (a control involving Boc-protection of MMAF showed a less polar spot on TLC), indicating that full reductive methylation had occurred (within the analytical capabilities of TLC monitoring) in which no other sites on the MMAF structure were expected to be affected.

Upon ^{1}H NMR spectroscopic analysis of the reaction product, it was found that the spectral output displayed a high degree of complexity, which has been postulated by Johansson and co-workers to be due to the auristatin peptides existing in solution as a mixture of s-*cis* and s-*trans* rotamers around the tertiary amide.[135] These conformers arise from restricted rotation around the amide bond bearing the pyrrolidine ring, due to partial double bond character resulting from n-pπ resonance of the amide nitrogen lone pair and the adjacent carbonyl group. The molecular structures of both the s-*cis* and s-*trans* rotamers are depicted in **Figure 30**, in which hydrogen atoms resulting in diagnostic ^{1}H NMR signals are represented by red numbers.

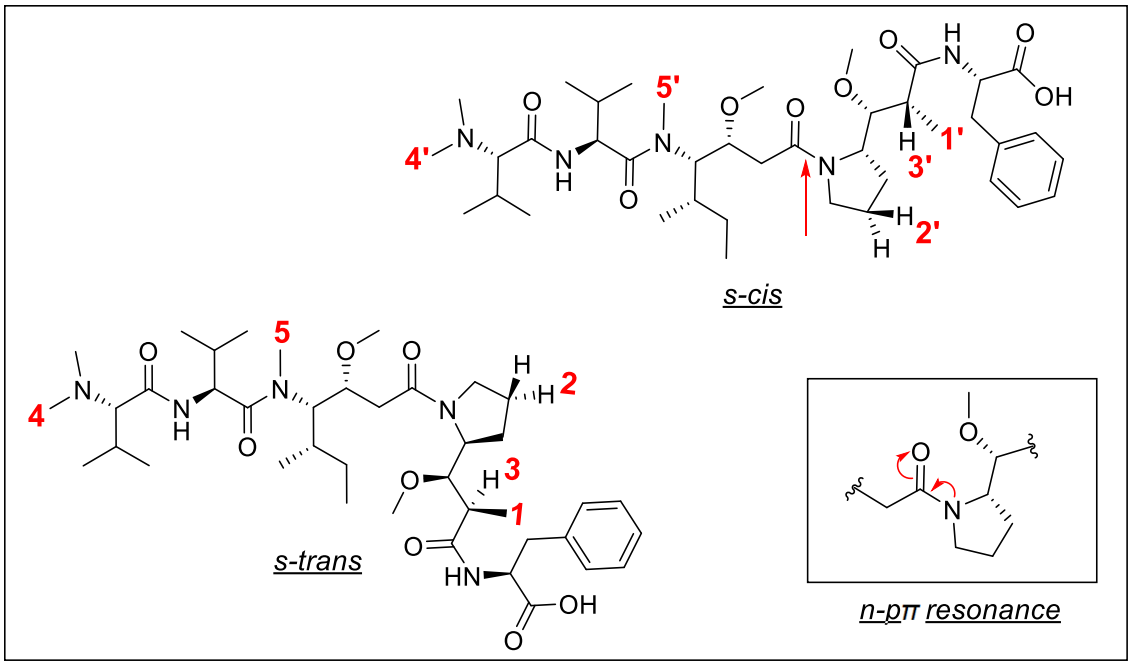

Figure 30: *Structural s-cis and s-trans rotamers resulting from n-pπ resonance, in which the amide bond displaying restricted rotation is highlighted with a red arrow.*

In light of this complexity, the NMR spectra of the auristatin-F derivatives, as well as subsequent products containing auristatin-F in this study, were not fully assigned. However, the upfield region in the ^{1}H NMR spectrum of auristatin-F (**Figure 31**), between 1.1 and 3.3 ppm, allowed for identification and the monitoring of diagnostic signals for this transformation, in which certain signals in this region could be assigned according to those made by Johansson and co-workers in their NMR spectroscopy study.

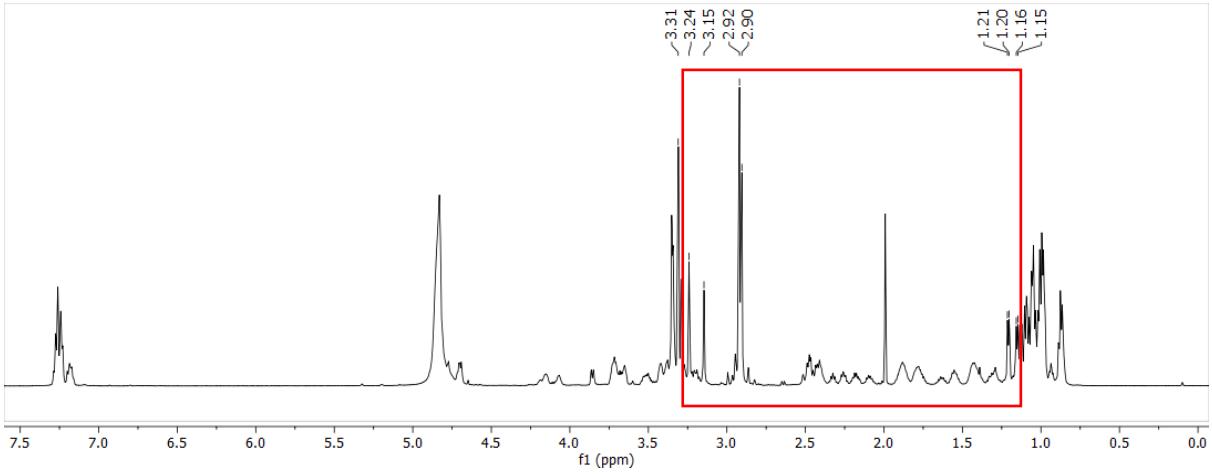

Figure 31: *^{1}H NMR spectrum of auristatin-F, recorded in CD_3OD.*

An expansion of these regions of the ^{1}H NMR spectra of MMAF and auristatin-F are displayed in **Figure 32** and **Figure 33**, respectively (with numerical assignments made according to **Figure 30**).

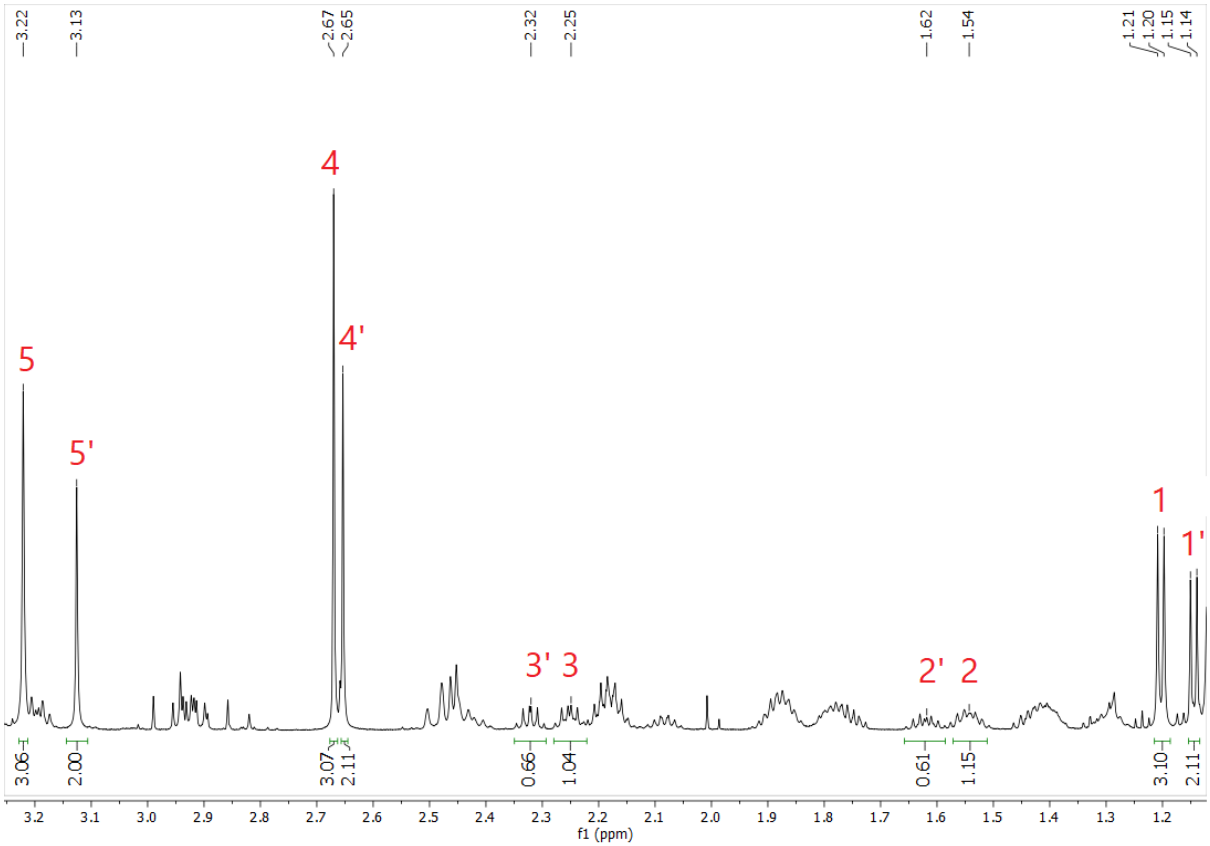

Figure 32: *^{1}H NMR spectrum of MMAF, from 1.1 – 3.3 ppm.*

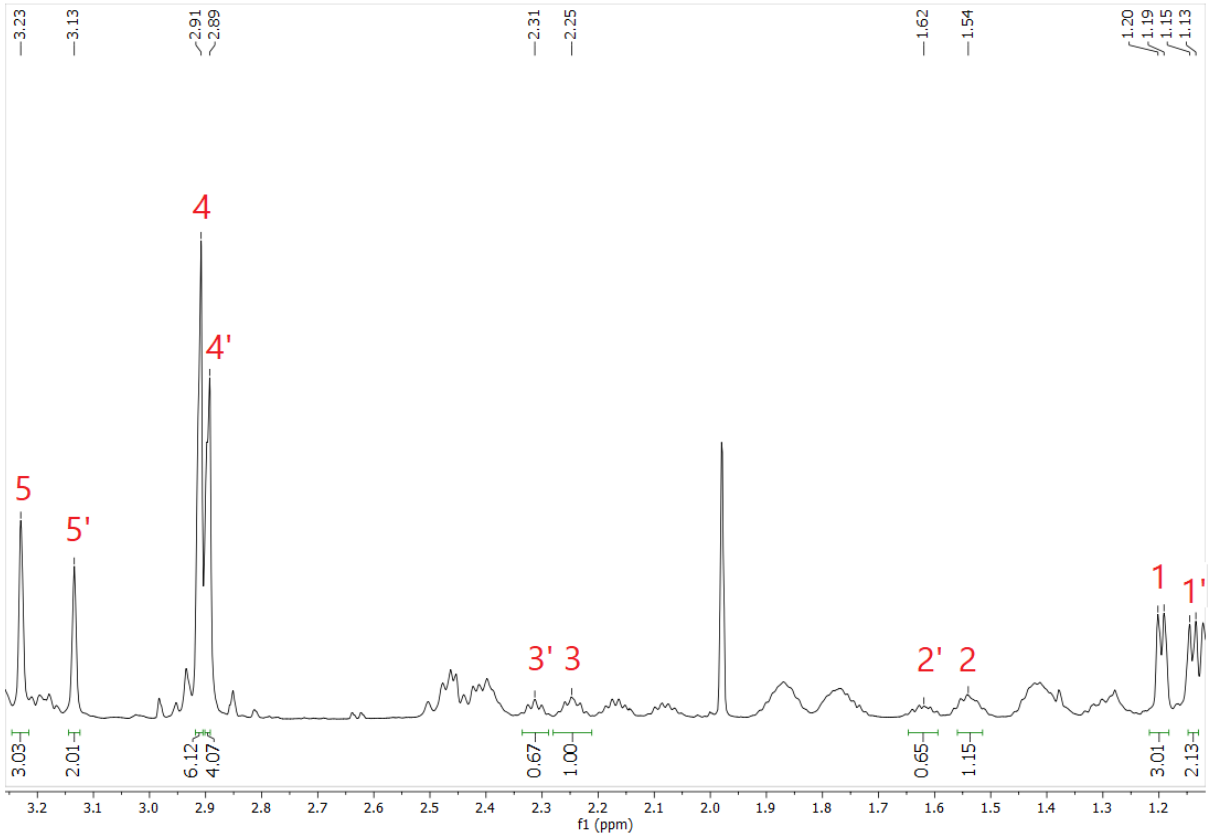

Figure 33: *^{1}H NMR spectrum of auristatin-F, from 1.1 – 3.3 ppm.*

In both spectra, a general integration ratio of *cis:trans* was observed as 2:3, revealing the relative abundance of the conformers in solution at room temperature. This ratio is consistent with the findings of Johansson and co-workers in their NMR study. The energy barrier for interconversion of the two conformers was also reported to be a significant 101 $kJ.mol^{-1}$, suggesting that the distribution of conformers remains relatively stable at biological temperature.[135] Importantly, the relative integration value for *N*-methyl assignments **4** and **4'** in the auristatin-F spectrum had doubled when compared to those of MMAF, while the remainder of the assigned resonances retained similar integration values. This information was sufficient to conclude that the methylation reaction was successful and so the product was admitted to the following transformation without further purification.

The next step involved preparing auristatin-F for the click coupling reaction, by converting its C-terminal carboxyl group into an *N*-propargylamide, as shown in **Scheme 16**.

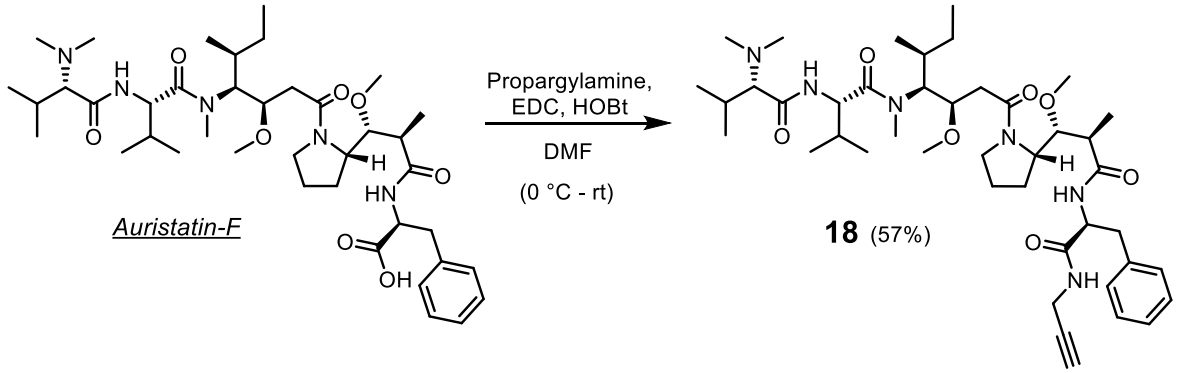

Scheme 16: *Amide coupling reaction between auristatin-F and propargylamine to yield* ***18****.*

This coupling reaction was performed in anhydrous DMF, in which propargylamine and catalytic hydroxybenzotriazole (HOBt) were added to a solution of auristatin-F and 1-ethyl-3-(3-dimethylaminopropyl)carbodiimide (EDC) at 0 °C before warming the reaction to room temperature. Once again, the reaction needed to be monitored with anisaldehyde spray, as previously described, in which it was possible to monitor the disappearance of auristatin-F concurrently with the formation of a less polar spot. Upon reaction completion, the DMF was removed *in vacuo* and the resulting residue adsorbed onto silica for purification directly by column chromatography, yielding the product as a colourless solid in 57% yield.

Characterisation of **18** was undertaken in the form of high-resolution MS (HRMS), in order to provide evidence for a successful coupling reaction, the spectrum of which is presented in **Figure 34** along with the structure of the $[M+H]^+$ ion. NMR spectroscopy was also performed, but the complex nature of the spectra resulted in upfield diagnostic resonances resulting from the installed propargylamide to be buried.

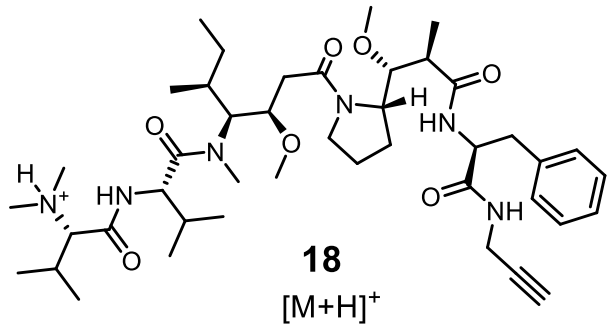

Chemical Formula: $C_{43}H_{71}N_6O_7$
Exact Mass: 783.5384
Molecular Weight: 784.0615
m/z: 783.5384 (100.0%), 784.5418 (46.5%), 785.5451 (10.6%)

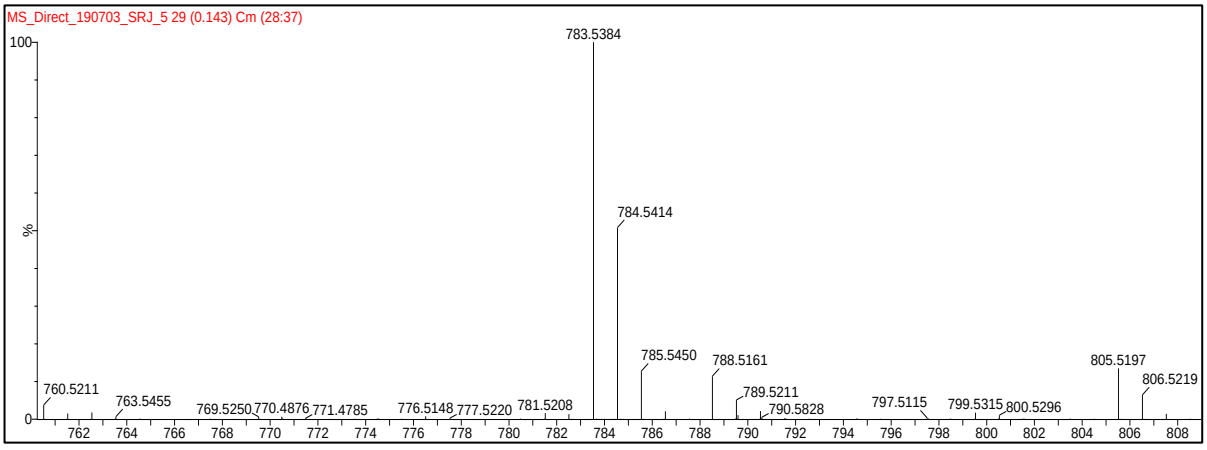

Figure 34: *HRMS output for **18** and the chemical structure of the $[M+H]^+$ ion.*

The MS output provided full confidence in the successful preparation of **18**, as a major peak was observed at an *m/z* value of 783.5384 that coincided exactly with the calculated value for the $[M+H]^+$ ion (783.5384). Not only did this allow for confirmation of a successful amide coupling reaction, but also that the preceding methylation reaction had been successful.

With both **18** and the azido BG-linker (**9**) in hand, it was now possible to undertake the pivotal click convergent step (**Scheme 17**) for producing the first BG-modified auristatin-F construct.

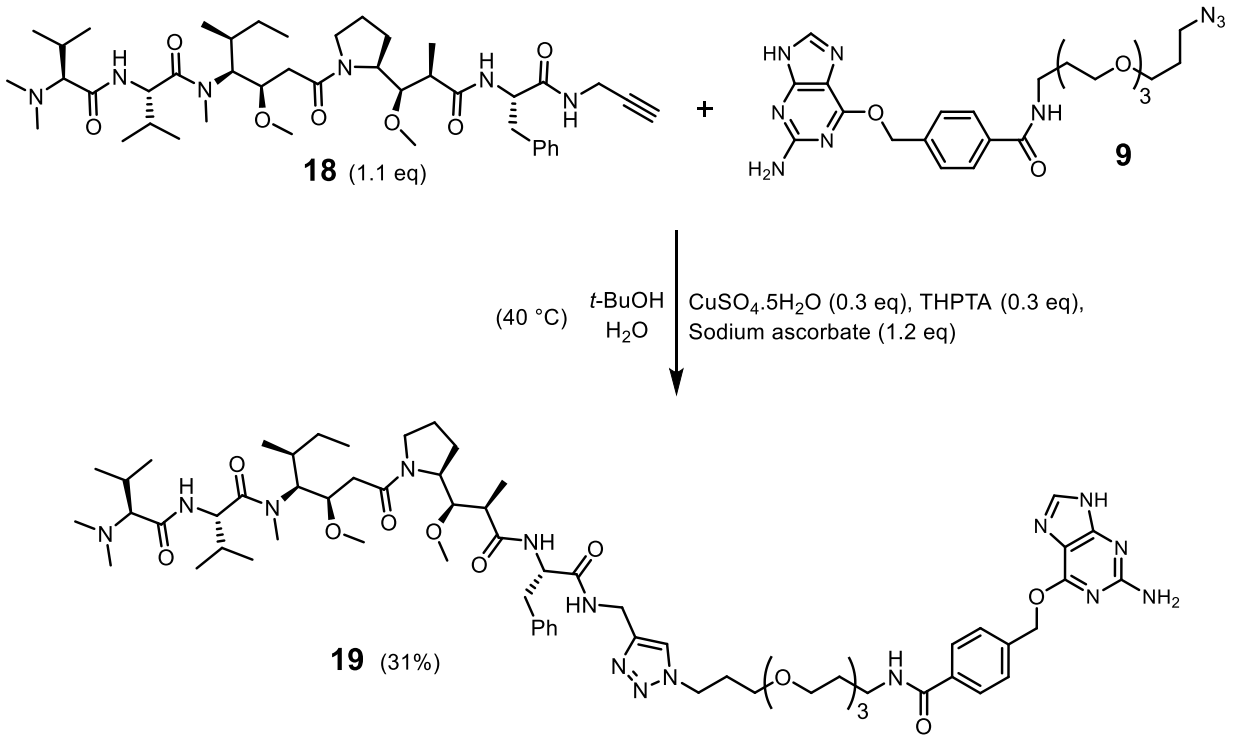

Scheme 17: *Key CuAAC click reaction of* ***18*** *and* ***9****.*

In initiating this reaction, compounds **18** (1.1 eq) and **9** were dissolved in *t*-BuOH to which an aqueous solution of $Cu_2SO_4{\cdot}5H_2O$ and tris(benzyltriazolylmethyl)amine (THPTA) was added to result in a 1:1 ratio of *t*-BuOH and water. The THPTA acts as a copper ligand, accelerating the reaction by ensuring the maintenance of the Cu(I) oxidation state.[136] Finally, sodium ascorbate was added in order to reduce the Cu(II) species to Cu(I) to initiate the CuAAC reaction, and the reaction warmed to 40 °C. Initial attempts to monitor this reaction with the previously utilised anisaldehyde system proved inadequate, but superior results were fortunately achieved by using a potassium permanganate ($KMnO_4$) stain. The product was identified on TLC by the appearance of a single spot, just below that of **9**, and after 60 hours the complete disappearance of **9** (as the limiting reagent) was observed. The resulting reaction mixture was stripped of solvent by freeze drying and the residue purified directly by column chromatography to yield **19** as a colourless solid (8.7 mg, 31% yield).

Owing to the intense UV-activity of **9**, it was expected that the click combination product would display adequate UV-activity to overcome the challenges faced with MMAF derivatisation. However, once again the UV-activity of the product was found to be extremely low, suggesting that the conjugation to MMAF resulted in quenching of the BG UV-activity. This presented similar challenges pertaining to its isolation and purity determination by HPLC-UV as with the products of the MMAF derivatisation reactions.

In spite of these challenges, NMR spectroscopic analysis was performed on the isolated product and the ^{1}H NMR spectrum is displayed in **Figure 35**, which displayed resonances attributable to both reactants.

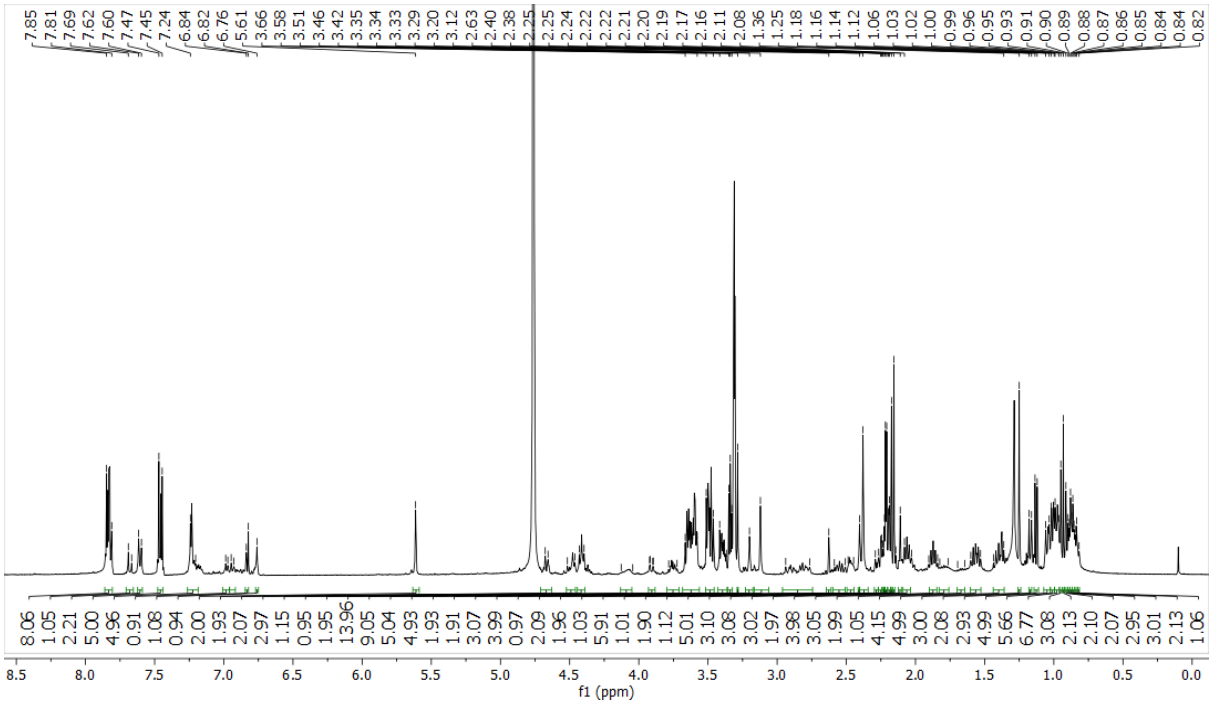

Figure 35: *^{1}H NMR spectrum of **19**, recorded in CD_3OD.*

In the spectrum, the all-important benzylic methylene singlet was immediately recognised at 5.61 ppm, along with highfield auristatin-F signals, suggesting a successful reaction outcome. Since only 8.7 mg was isolated, and due to the large molecular weight of the compound, the upfield region containing the complex auristatin-F broad multiplet signals (as well as those of the PEG chain) was not highly resolved and so it was not possible to fully differentiate and assign all of the resonances. However, the presence of both conformers in the product was suggested by the upfield region between 1.1 and 3.3 ppm displaying a similar pattern to that previously assigned for auristatin-F, as well as signal pairing in the aromatic region. A pair of doublet resonances at 7.46 ppm was assigned as the hydrogens previously assigned to the more upfield doublet of the AA'BB' ring system in the ^{1}H NMR spectrum of **9**, and those previously assigned to the downfield doublet, as well as the guanine methine signals, were assigned to a multiplet signal around 7.82 ppm. Furthermore, the auristatin-F aryl hydrogens were assigned to a multiplet around 7.23 ppm and the triazole hydrogen was assigned to a pair of singlet resonances at 7.61 ppm. This data provided evidence that both rotamers had reacted and the respective products were isolated as a mixture due to having equal polarity. The ^{13}C NMR spectrum of **19**, allowing for further structural insight, is shown in **Figure 36**.

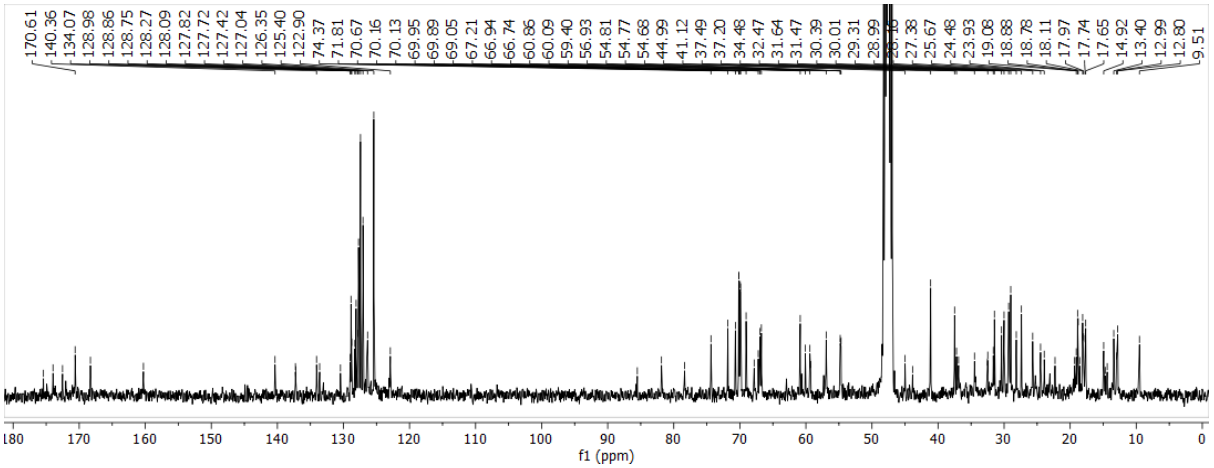

Figure 36: *^{13}C NMR spectrum of **19**, recorded in CD_3OD.*

Resonances in the ^{13}C spectrum of **19** were correlated with those in the ^{13}C NMR spectra of both auristatin-F and **9**, allowing for further corroboration of structure. Specifically, vital ^{1}H NMR signals of **9** were assigned to their corresponding ^{13}C NMR resonances by use of 2D Heteronuclear single quantum coherence (HSQC) NMR spectroscopy, such as those of the benzylic methylene, the guanine methine and the AA'BB' doublet pair. These signals were assigned in the ^{13}C NMR spectrum of **19** as resonances at 66.74 ppm, 140.36 ppm as well as at 127.04 and 127.72 ppm, respectively.

In order to improve on confidence in the reaction outcome, the product was submitted for HRMS analysis – the output of which is displayed in **Figure 37**.

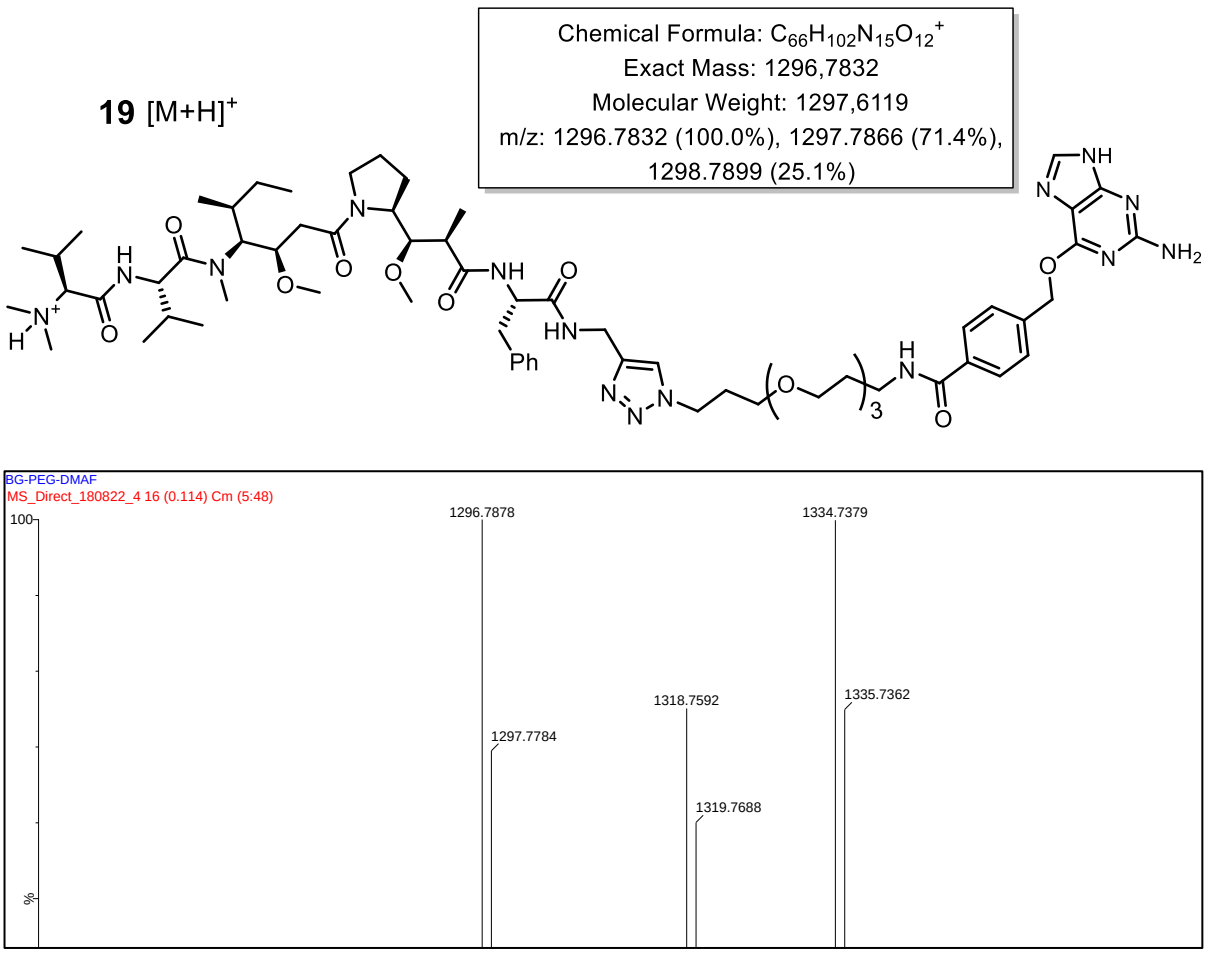

Figure 37: *HRMS output for* ***19*** *and the chemical structure of the [M+H]⁺ ion.*

A major peak in this spectrum displayed an *m/z* value of 1296.7878, corresponding to the $[M+H]^+$ ion of the product for which this value was calculated as 1296.7832. Error in the *m/z* value is tolerated up to 50 per 10,000 in major journals, so the deviation from the calculated value is well within bounds for **19**.

The data on the first ADC-precursor construct supported its successful preparation and even though analytical purity data was not obtainable via HPLC, the product did display a single spot on TLC, reasonable NMR spectra and a satisfactory HRMS. In spite of these shortcomings, **19** was considered to be satisfactory for SNAP-tag conjugation and subsequent biological evaluation. Since the SNAP-tag conjugation is followed by a purification step to remove unconjugated material from conjugated fusion proteins by use of size-exclusion chromatography, a level of purity uncertainty was not expected to influence the biological evaluation. In the event, subjecting the sample to SNAP-tag conjugation and evaluating the resulting ADC biologically showed some positive results, which are discussed in **Chapter Three**.

In light of the lack of UV-activity for **19**, which made analysis and isolation aspects difficult, it was decided to redesign the linker system to include a fluorescent tag. Not

only would this strengthen the case of this MSc research from a chemistry perspective, but it was considered likely to afford insights into the design and synthesis of SNAP-tag ADC-precursor constructs concerning other non-UV-active cytotoxins.

2.2.3 Fluorescent BG-linker strategy

Based on knowledge gleaned from the first target study, the next and final ADC-precursor target identified an amide coupling of the carboxyl of auristatin-F with the amino group of a BG-linker incorporating a fluorescent tag. The dansyl (5-(dimethylamino)naphthalene-1-sulfonyl) fluorescent tag was chosen for this application, in view of its ease of incorporation and handling, as well as its UV and fluorescent properties. Access to an amino group at the terminus was anticipated to be achievable via Staudinger reduction of an azide, since technology was now in place for azido introduction. In order to reduce synthesis efforts, introducing the BG moiety was proposed to be achievable by modification and incorporation of the azido BG-linker (**9**) already in hand. The chemical structure of the new fluorescent BG-linker target is presented in **Figure 38**, in which the component resulting from **9** is highlighted in blue colour. The synthesis aimed to use *p*-aminobenzoic acid as a bifunctional component, around which various couplings including Mitsunobu and standard amide coupling could be used.

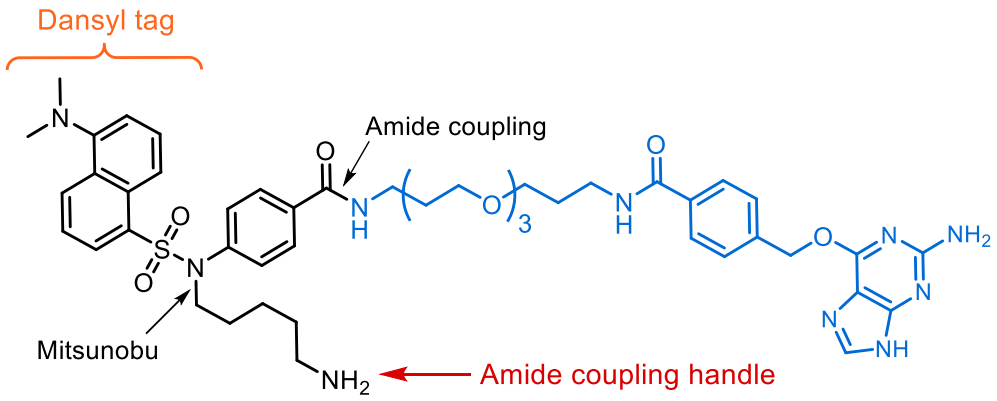

Figure 38: *Chemical structure of the fluorescent BG-linker target.*

The synthesis to afford the fluorescent BG-linker commenced with Fischer esterification of *p*-aminobenzoic acid, as per **Scheme 18**, using HCl (generated from acetyl chloride) in anhydrous methanol.[137]

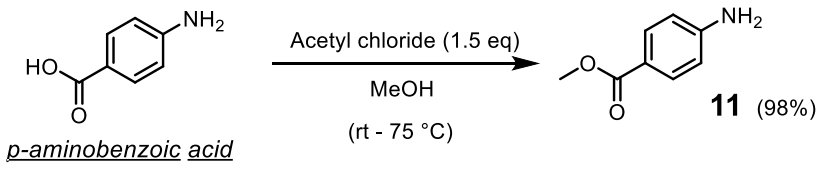

Scheme 18: *Methyl ester formation on p-aminobenzoic acid, to afford* ***11****.*

The transformation was monitored by TLC and the progression was determined by disappearance of the starting material concurrently with the formation of a less polar spot. Upon completion, the reaction mixture was added to a saturated $NaHCO_3$ solution and extracted with DCM, which was subsequently washed, dried and concentrated to afford **11**, in 98% yield, as a light-yellow solid which was sufficiently pure without chromatography.

The spectral data obtained for **11** agreed with that reported in the literature, in which the ^1H NMR spectrum importantly displayed the aryl AA'BB' 2H doublet pair, as well as the methyl ester 3H singlet, at 7.85, 6.63 and 3.85 ppm, respectively.[138]

Incorporation of the dansyl fluorescent tag was achieved by the S_NAc-like reaction of **11** with dansyl chloride, using anhydrous pyridine as a base and a solvent (**Scheme 19**). These reaction conditions resulted from an in-house innovation due to poor yields (37%) resulting from the literature procedure, in which triethylamine was used as a base and DCM as a solvent.[139]

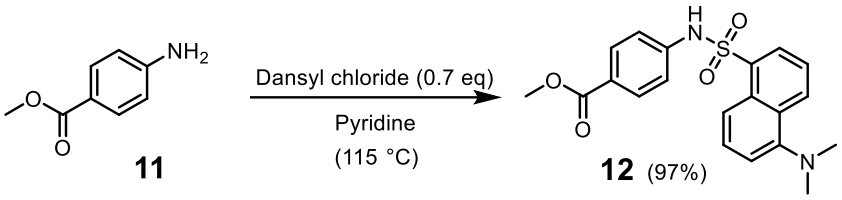

Scheme 19: *Reaction of **11** with dansyl chloride, to afford **12**.*

The reaction was stirred under reflux, for 36 hours, at which point the depletion of dansyl chloride (as the limiting reagent) was observed on TLC, along with the formation of **12** as a more polar fluorescent spot. Following the removal of pyridine under vacuum, the residue was adsorbed directly onto silica for purification by column chromatography, which yielded **12** as a bright yellow solid, in 97% yield. The significantly improved yields of our method likely resulted from pyridine forming a salt with dansyl chloride as a sulfonyl transfer catalyst, thereby increasing the sulfonyl electrophilicity with the relatively poorly nucleophilic amine.

The successful isolation of **12** was confirmed by its ^1H NMR and ^{13}C NMR spectra, which agreed with those reported in the literature.[139] The ^1H NMR spectrum is shown in **Figure 39**, revealing a discernible pattern of aromatic resonances for future reference, as well as the dimethylamino and methyl ester singlets.

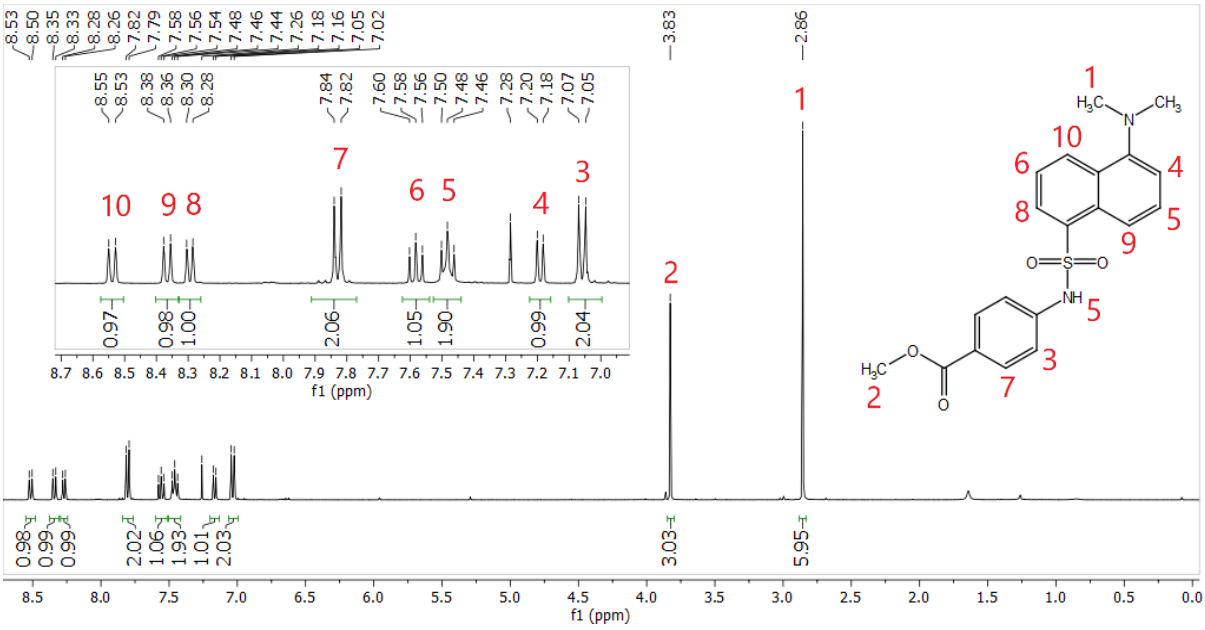

Figure 39: *^{1}H NMR spectrum of **12**, recorded in $CDCl_3$.*

The 1,4-substituted ring was represented by a pair of AA'BB' doublets, at 7.04 and 7.83 ppm, while the dansyl aromatic hydrogens were assigned to four doublets and two triplet resonances, with the integration values correctly summing to 6H. A broad singlet for the secondary amine of the sulfonamide was present within the most upfield triplet (5), at 7.48 ppm. The ^{13}C NMR spectrum displayed a total of 17 distinct resonances in accordance with the structure and symmetry of **12**.

Introduction of the azido alkyl spacer was planned to proceed with N-alkylation by way of a Mitsunobu reaction, which required the preparation of an azido alcohol. This species was prepared from 1,5-pentanediol, via a mono-mesylate, as shown in **Scheme 20**.

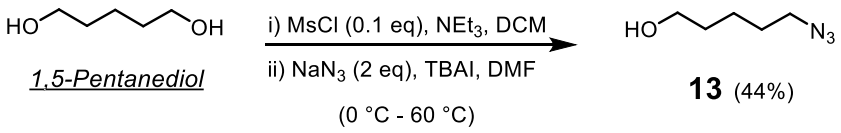

Scheme 20: *Derivatisation of 1,5-pentanediol, by mono-mesylation and azidation, to yield **13**.*

Mono-mesylation was ensured by having the diol in a tenfold excess, in which excess diol could be removed after the reaction by washing the organic extracts with brine in view of its high water solubility. Thereafter, the crude product was dissolved in DMF and reacted with excess NaN_3 and tetrabutylammonium iodide (TBAI), the latter acting as a catalyst for the S_N2 reaction with NaN_3. After reaction completion, as determined by TLC analysis, the DMF was removed *in vacuo* and the residue purified directly by column chromatography to afford **13** as a clear oil, in 44% yield over two steps.

The NMR spectroscopic data of **13** agreed with that in the literature, confirming the success of the conversion.[140] The ^{1}H NMR spectrum is displayed in **Figure 40**, in which two distinct triplets were observed for the terminal methylene hydrogens, thereby confirming the mono-functionalisation. Similarly, the ^{13}C NMR spectrum displayed five distinct signals, accounting for all five carbon atoms in the molecule.

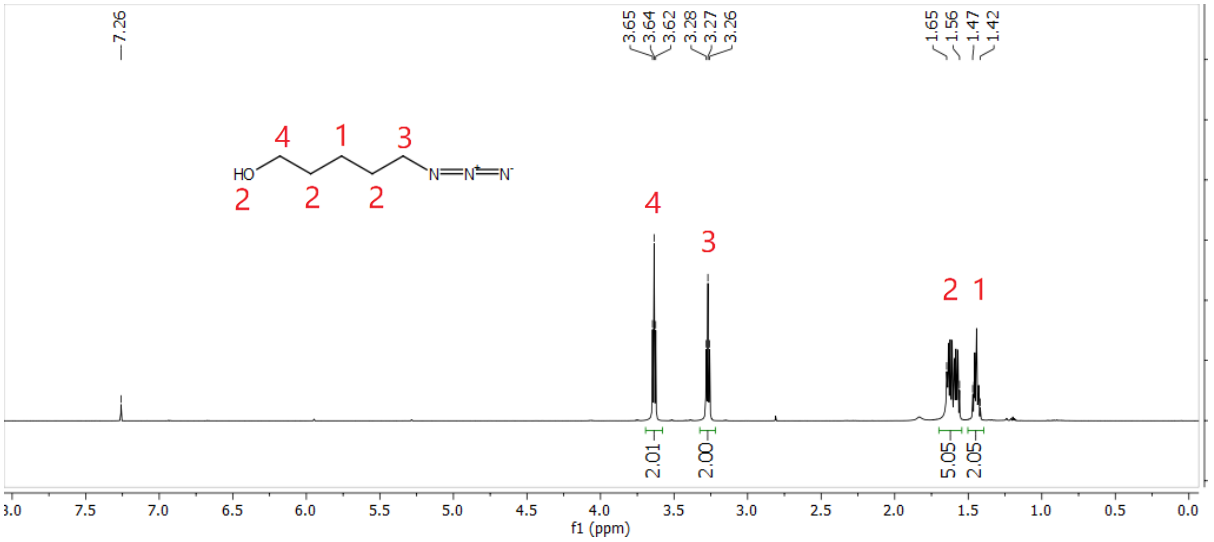

Figure 40: *^{1}H NMR spectrum of **13**, recorded in $CDCl_3$.*

Finally, the IR spectrum (**Figure 41**) revealed a typical azide stretching frequency at 2097 cm^{-1} and an O-H stretching frequency at 3352 cm^{-1}, further corroborating the synthesis of **13**.

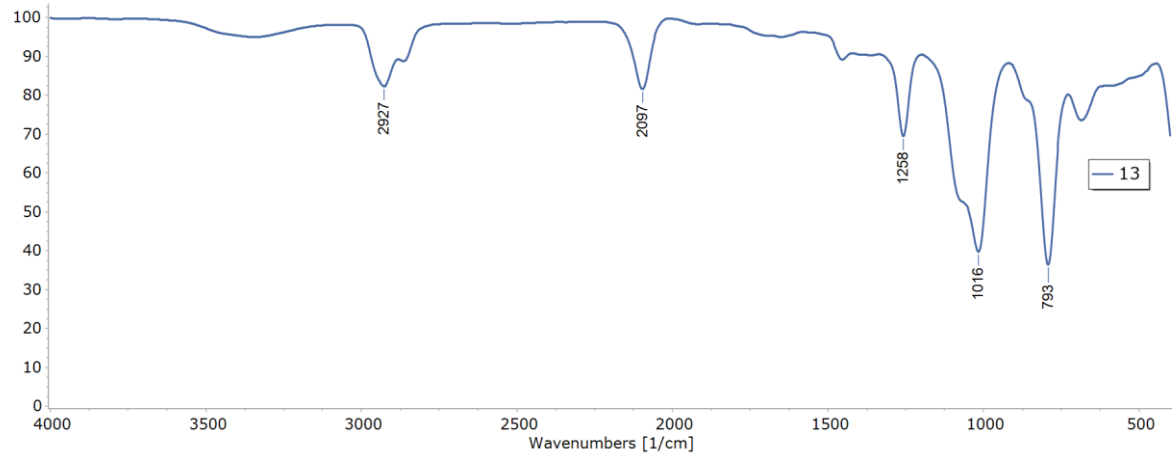

Figure 41: *IR spectrum of **13**, with diagnostic absorptions highlighted.*

Acquisition of **13** allowed for a Mitsunobu reaction to be carried out with **12**, as shown in **Scheme 21**.

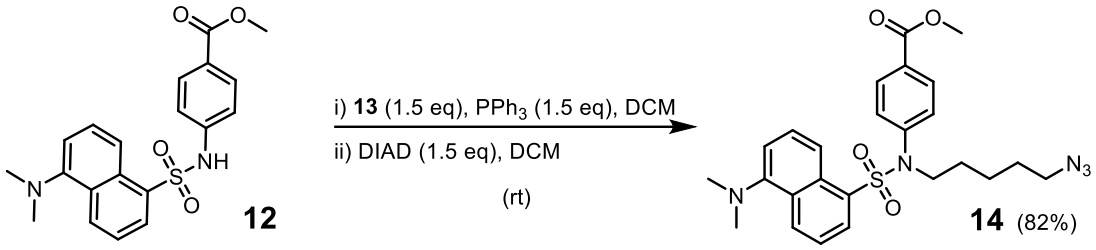

Scheme 21: *Mitsunobu reaction of* ***12*** *and* ***13****, to yield* ***14****.*

The mechanism of the Mitsunobu reaction is long but well-known, in which PPh_3 adds to a diisopropyl azodicarboxylate (DIAD) nitrogen atom to form a betaine intermediate that abstracts a proton from the relatively acidic sulfonamide **12** to generate its anion.[141] Substitution of the oxophilic phosphonium ion of the betaine by the alcohol **13** generates an oxyphosphonium ion that subsequenty reacts with the sulfonamide anion. This affords the N-alkylation via an S_N2 mechanism, with expulsion of the notorious triphenylphosphine oxide, which is oftentimes difficult to remove from the reaction product. The reaction was complete within 3 hours at room temperature, delivering **14** as a yellow oil, in 82% yield, after work-up and chromatography. The compound appeared as a beautiful fluorescent and brightly UV-active spot on the TLC plate, under 354 and 254 nm light respectively.

This compound has not previously been reported in the literature and as a result, full characterisation was undertaken in the form of ^{1}H NMR, ^{13}C NMR and IR spectroscopy, as well as LC-MS. In the assigned ^{1}H NMR spectrum, as shown below in **Figure 42**, the individual resonances arising from both **12** and **13** were clearly visible.

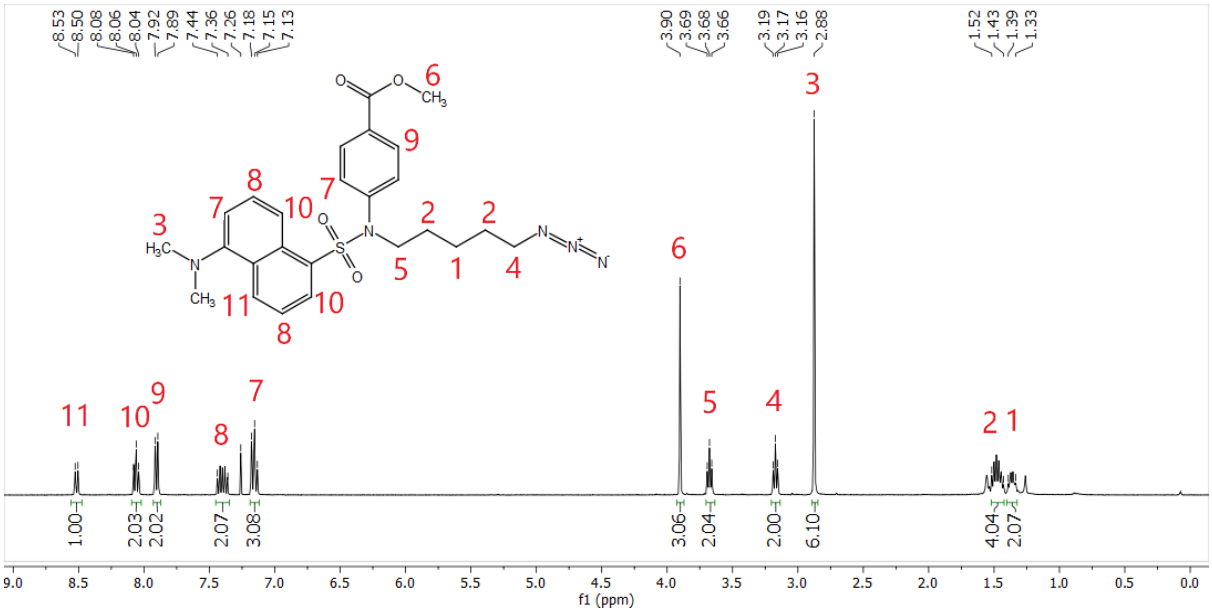

Figure 42: *^{1}H NMR spectrum of* ***14****, recorded in $CDCl_3$.*

The upfield region harboured resonances analogous to those previously seen for the azido alkyl chain, dimethylamino and methyl ester hydrogen atoms. By comparison, the downfield aromatic region remained largely similar to that of **12**, in which a downfield shift of certain resonances (testament to the change in electronic environment afforded by the N-alkylation) resulted in coalescence with neighbouring resonances. Similarly, the ^{13}C NMR spectrum of **14** displayed all of the expected 22 distinct signals, on symmetry grounds, of the 25 carbon atoms in the molecule. The IR spectrum of **14** was compared to that of **12** in **Figure 43**, with an additional absorption for an azide stretch at 2094 cm^{-1}.

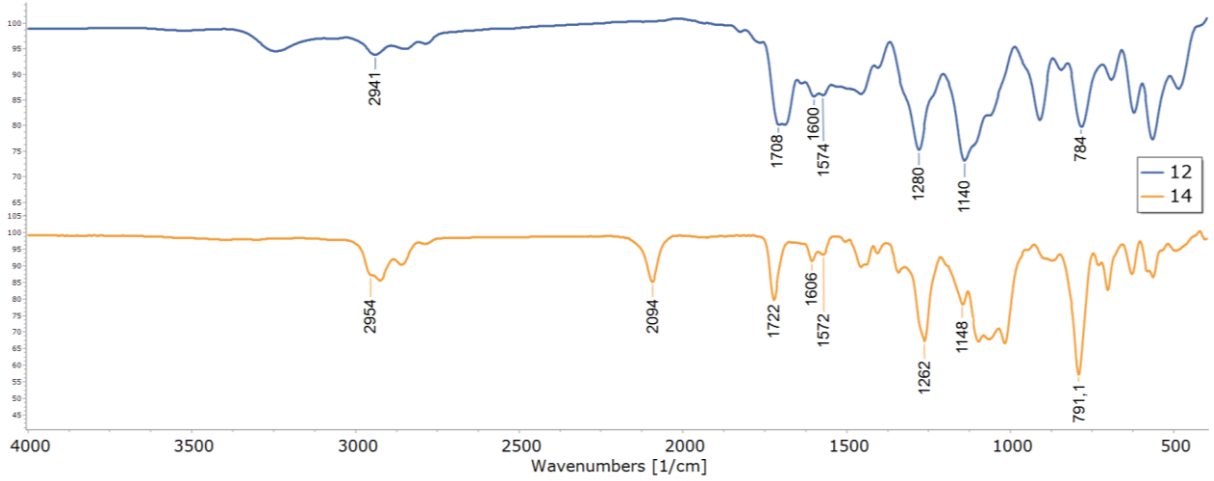

Figure 43: *IR spectrum of **14**, compared to that of **12**, displaying key absorptions.*

As a final measure of structure confirmation, the compound was submitted for LC-MS analysis, in which a major peak was observed at an *m/z* value of 496.1 in good agreement with the calculated value (496.20) for the $[M+H]^+$ ion of **14**.

The following transformation involved methyl ester hydrolysis of **14** to its free carboxylic acid, as depicted in **Scheme 22**.

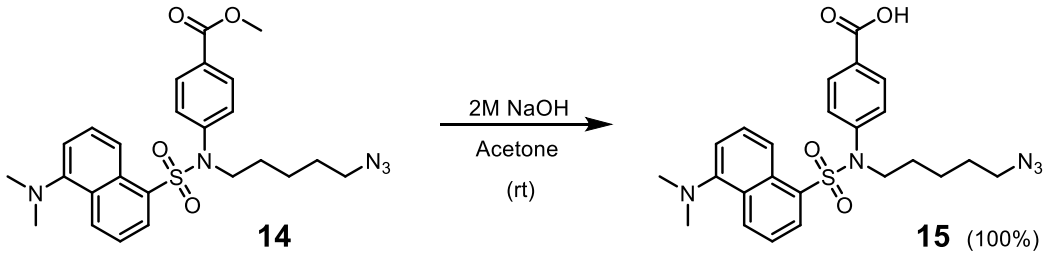

Scheme 22: *Ester hydrolysis of **14**, with aqueous NaOH, to yield **15**.*

This transformation proceeded via base hydrolysis, using sodium hydroxide (NaOH), in quantitative yield after an acid-base extraction that served as an adequate method of purification to afford **15** as a yellow oil.

This compound has not previously been reported in the literature and as a result was fully characterised by ^{1}H NMR, ^{13}C NMR and IR spectroscopy as well as LC-MS. The most notable difference in the ^{1}H NMR spectrum of **15** (**Figure 44**) was the loss of the 3H singlet for the methyl ester, while the remaining signals were conserved.

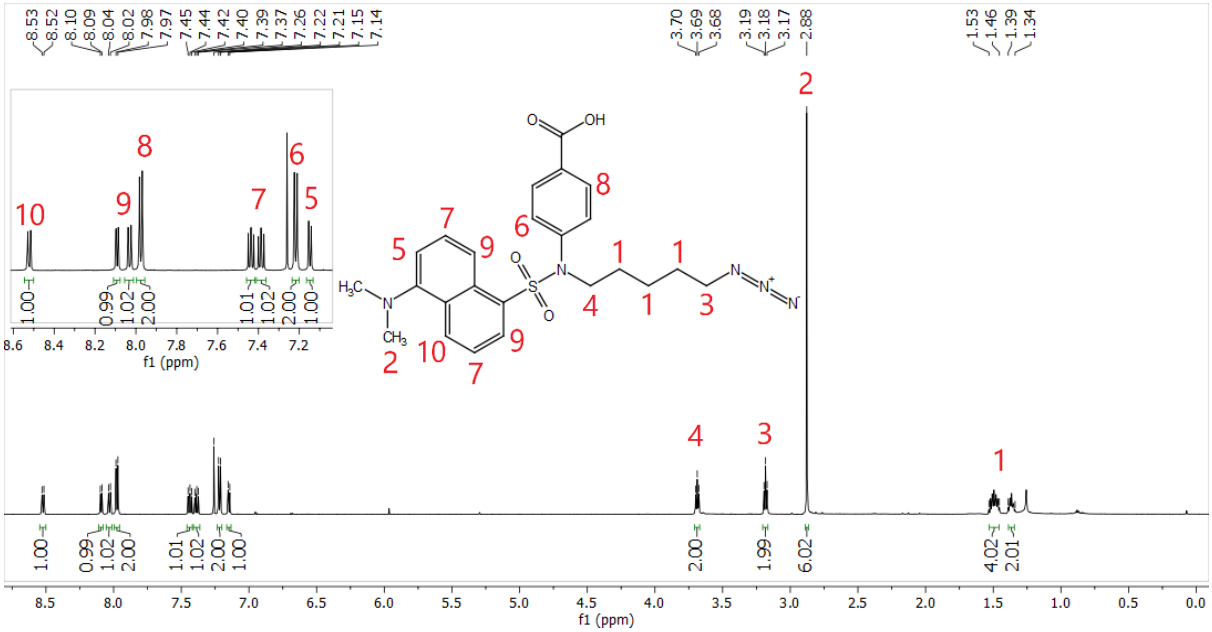

Figure 44: *^{1}H NMR spectrum of **15**, recorded in $CDCl_3$.*

The ^{13}C NMR spectrum lacked one highfield resonance in comparison to **14**, displaying 21 distinct resonances, while the IR spectrum revealed an absorption at 3296 cm^{-1} typical of a carboxylic acid O-H stretch. Finally, LC-MS yielded an *m/z* value of 482.0, which is in close agreement for the calculated value of 482.19 for the $[M+H]^{+}$ ion.

With **15** in hand, the next step towards the fluorescent BG-linker target involved Staudinger reduction of the azido BG-linker (**9**), presented in **Scheme 23**, in order to generate the primary amino group for amide coupling with **15**.[142]

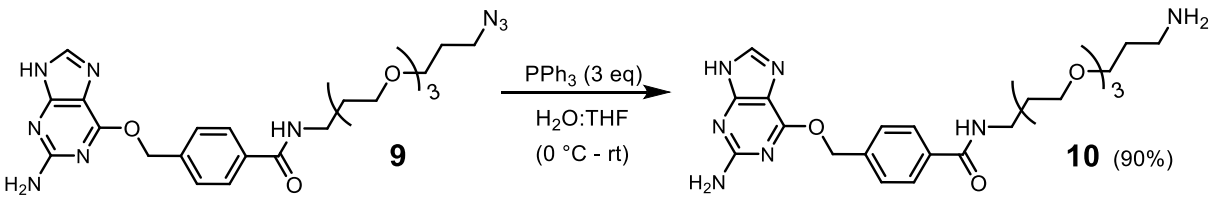

Scheme 23: *Staudinger reduction of **9**, to yield the amino derivative **10**.*

Mechanistically, PPh_3 undergoes addition with the azide to form a phosphazide that eliminates N_2 to generate an iminophosphorane, which hydrolyses to the amine. The reaction proceeded uneventfully to produce the polar amine as a colourless solid, in 90% yield, following chromatography facilitated by ammonia in the eluant.

Full characterisation was carried out on this molecule in the form of ^{1}H NMR, ^{13}C NMR and IR spectroscopy, as well as LC-MS, as it has also not previously been reported in the literature. The ^{1}H NMR spectrum differed from that of **9** only by virtue of a broad 2H singlet at 2.82 ppm for the terminal amino group hydrogens. The ^{13}C NMR spectrum displayed 21 distinct resonances as expected, accounting for all non-equivalent carbon atoms. The IR spectrum of **10** is presented in **Figure 45**, compared to that of **9**, showing loss of the azido stretch as a confirmation of the success of the Staudinger reduction. The main diagnostic signal for the new amine functional group would have been the C-N stretching absorption, which was likely embedded within the aliphatic ether signal at 1095 cm^{-1}.

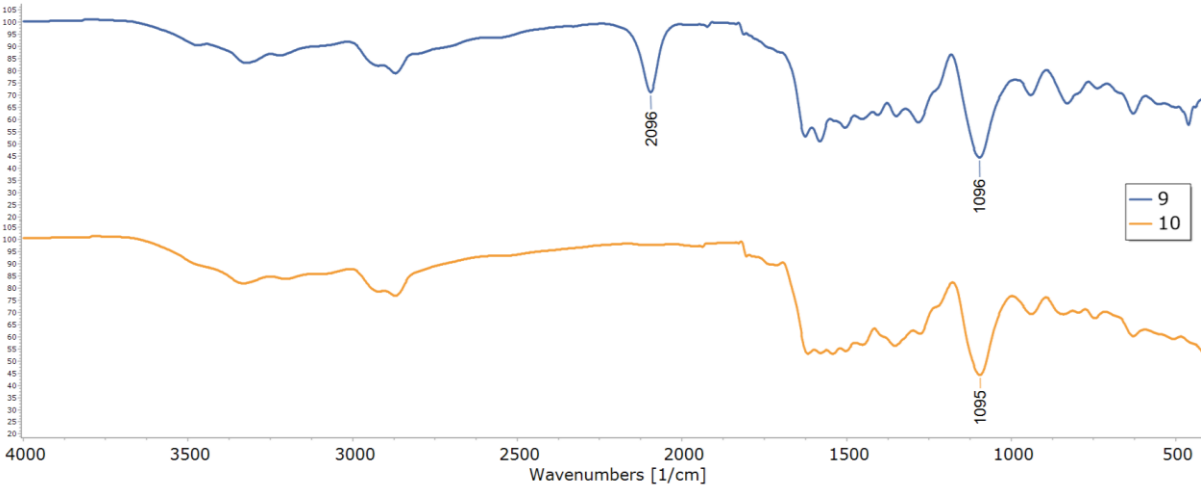

Figure 45: *IR spectrum of **10**, compared to that of **9**, displaying key absorptions.*

Final characterisation was achieved by LC-MS analysis, in which an *m/z* value of 488.1 agreed with the calculated value of 488.26 for the $[M+H]^{+}$ ion.

The amide coupling of **15** and **10** followed, which was achieved as per **Scheme 24** using anhydrous DMF as a solvent, DMAP as a promoter and EDC (1.5 eq) as a coupling agent.

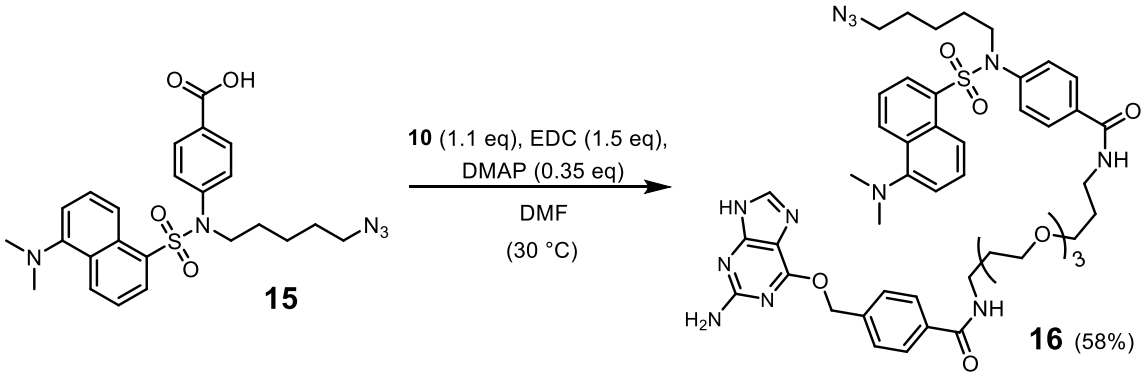

Scheme 24: *Amide coupling reaction of **15** and **10**, to yield **16**.*

A slight excess of **10** was used to ensure full consumption of **15**, in order to simplify chromatography, which was observed by TLC within 36 hours. Upon completion, the DMF was removed *in vacuo*, which was followed by direct purification using column chromatography, yielding **16** as a yellow oil in 58% yield.

Once again, full characterisation was undertaken since, unsurprisingly, this compound has not been reported in the scientific literature. The ^{1}H NMR spectrum of **16** comprised signals representing both **15** and **10**, the upfield region of which is displayed in **Figure 46**.

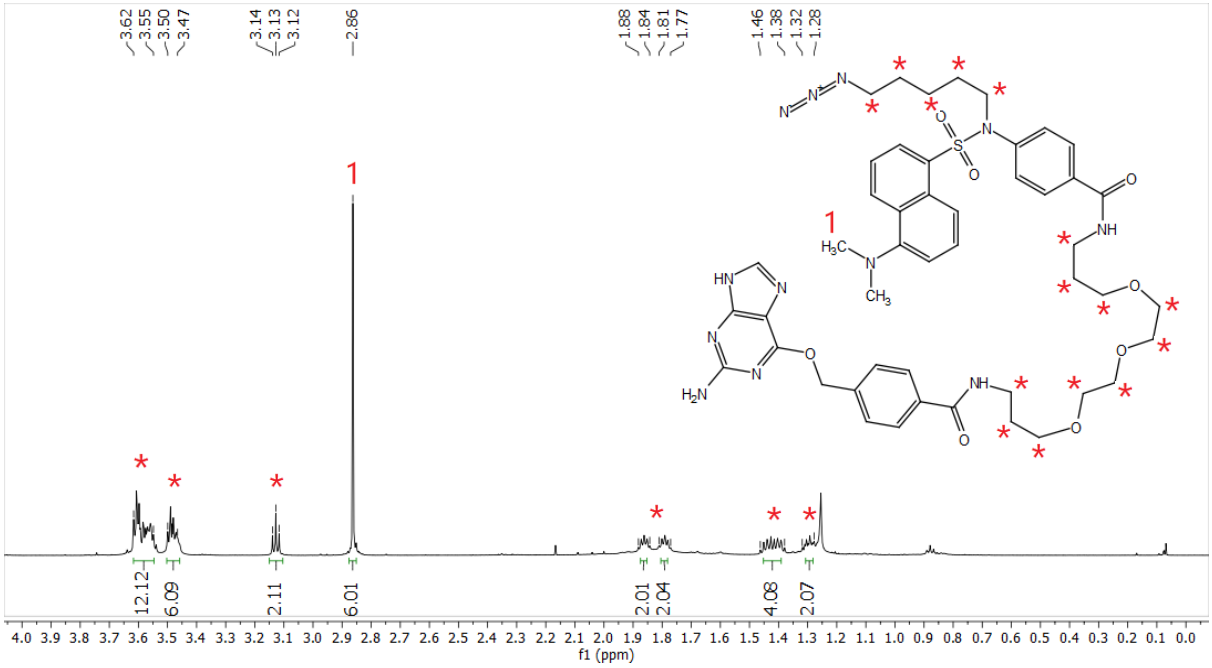

Figure 46: *Upfield region of the ^{1}H NMR spectrum of **16**, recorded in $CDCl_3$.*

The aliphatic ether PEG hydrogens as well as those of the alkyl azido spacer were represented by a range of multiplet signals between 1.2 and 3.7 ppm, in similar regions as previously reported for **15** and **10**, while a 6H singlet was present at 2.86 ppm for the dimethylamino hydrogen atoms. The downfield region of this spectrum is displayed in **Figure 47**, which accounted for the remainder of the resonances. Two 2H singlets were present at 4.97 and 5.53 ppm, representing the guanine amino and BG benzylic methylene hydrogens, respectively. Although the integration values of the aromatic region were in line with the aromatic regions of **15** and **10**, coalescence of certain aromatic resonances were observed in the spectrum. As seen in **Figure 47**, the signals were all assigned and consistent with the resonances resulting from the precursors.

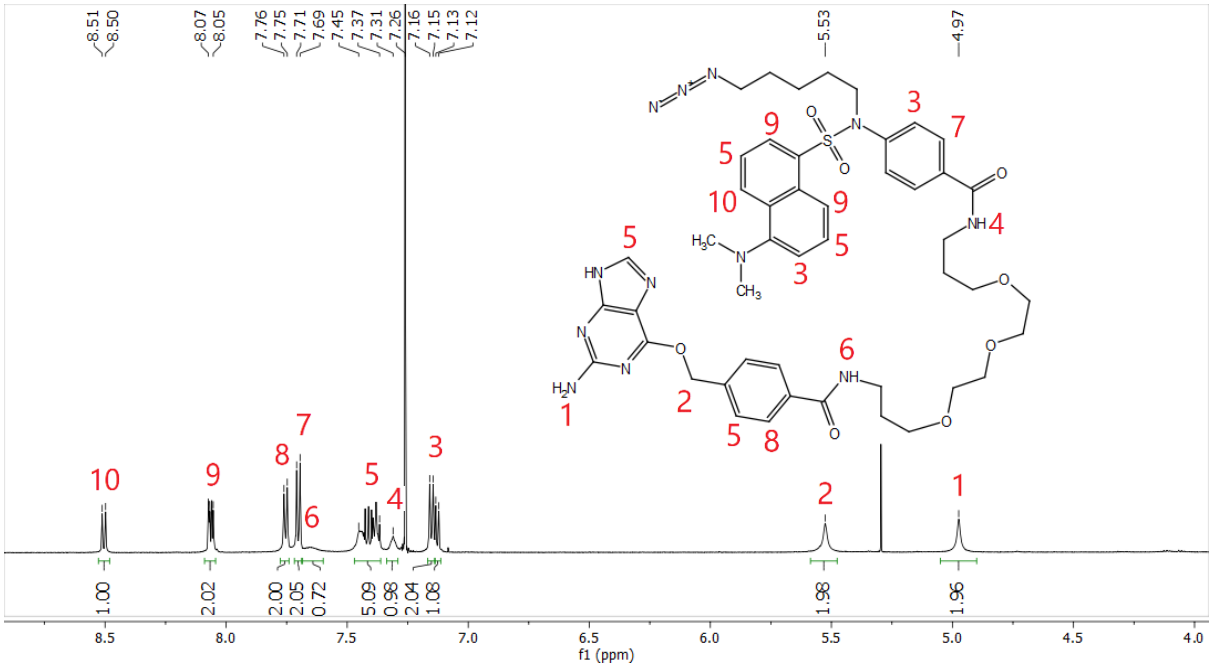

Figure 47: *Downfield region of the ^{1}H NMR spectrum of* ***16****, recorded in $CDCl_3$.*

The successful preparation of **16** was also corroborated by ^{13}C NMR spectroscopy and HRMS analysis, the latter returning an *m/z* value of 951.4293, which was in close agreement with the calculated $[M+H]^+$ ion of 951.4300.

The final transformation to afford the trifunctional fluorescent BG-linker **17** was a Staudinger reduction, which was achieved according to conditions shown in **Scheme 25**.

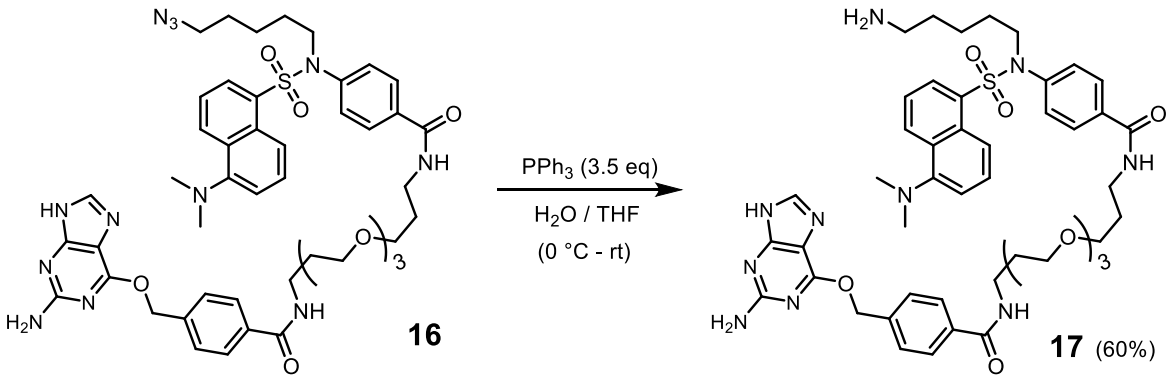

Scheme 25: *Staudinger reduction reaction on* ***16****, to afford the amino derivative* ***17****.*

This transformation was carried out as per the reduction of **9**, in which the product was visible on TLC as a highly polar fluorescent spot. Upon completion, direct column chromatography using neutralised silica yielded **17** as a yellow solid, in 60% yield. Full characterisation was carried out once again, in which the IR spectral data for both **16** and **17** are displayed in **Figure 48** showing loss of the azido functionality.

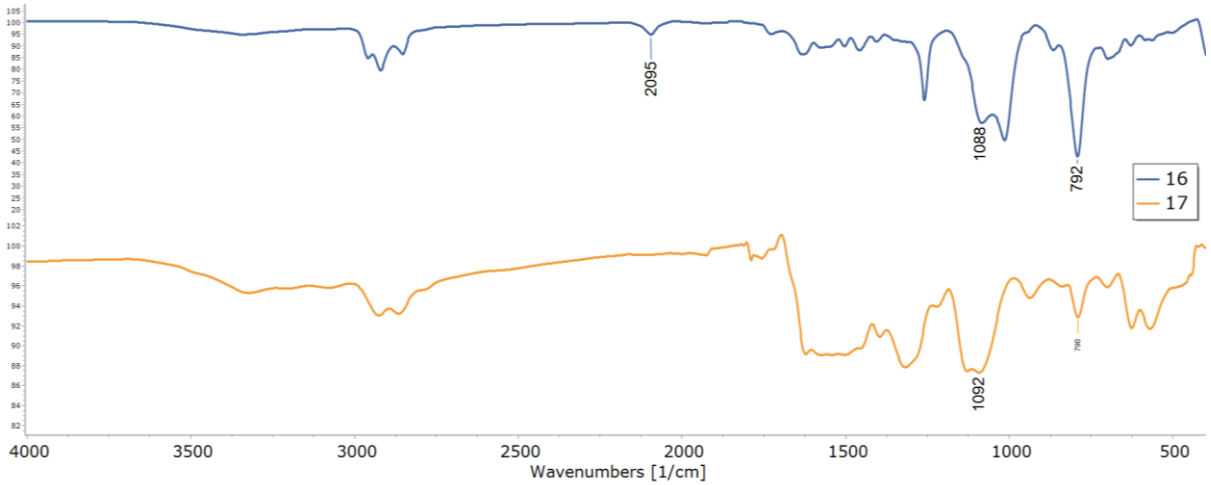

Figure 48: *Comparison of the IR spectra of both* ***16*** *and* ***17****.*

Extensive NMR spectroscopic analysis was also undertaken. Figures **49** and **50** show the various regions of the ^{1}H NMR spectrum of **17**, with assignments, in which the upfield region remained similar to that of **16**, except for a new 2H singlet at 2.60 ppm for the alkyl primary amine hydrogens. Also of note in the downfield region was the benzylic methylene singlet (H-1) at 5.59 ppm, as well as the methine singlet (H-8) of the guanine ring system at 7.85 ppm. Otherwise all aromatic signals were clearly visible.

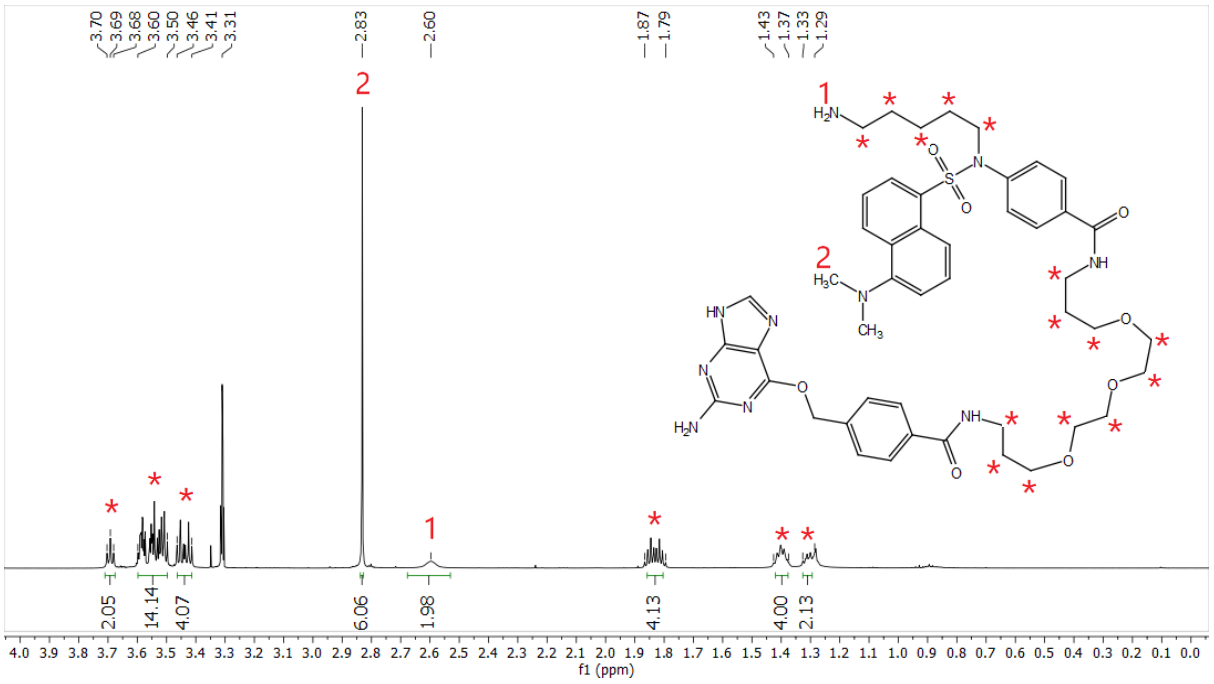

Figure 49: *Upfield region of the ^{1}H NMR spectrum of* ***17****, recorded in CD_3OD.*

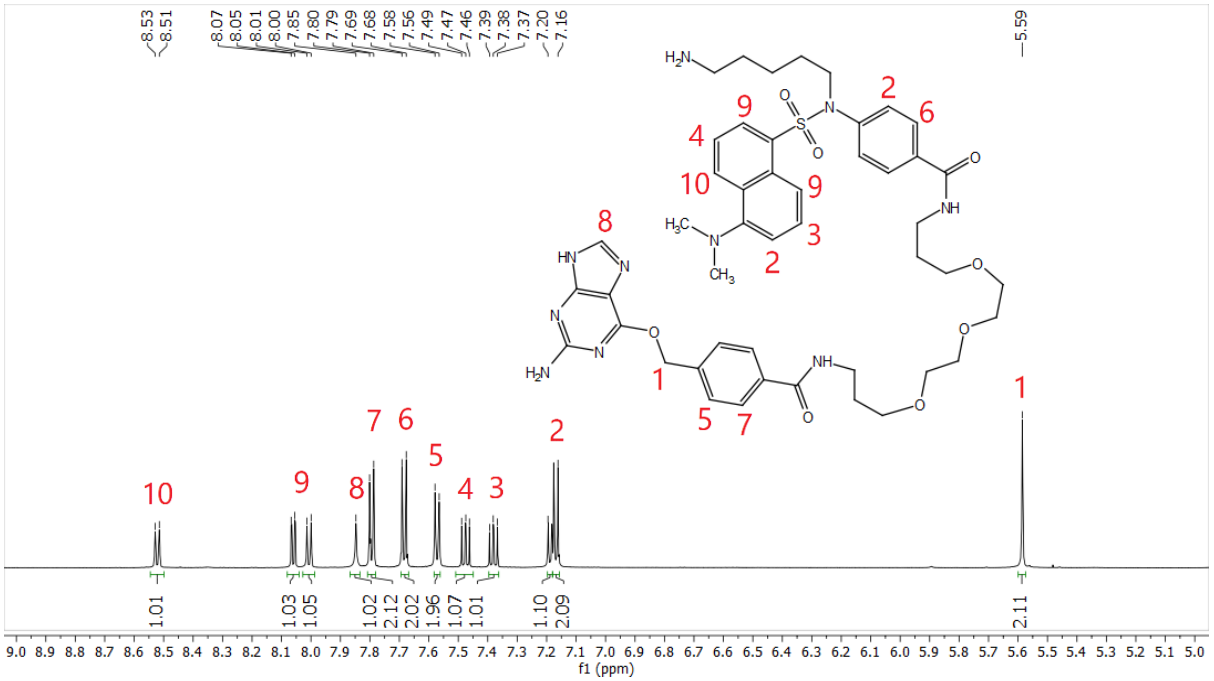

Figure 50: *Downfield region of the ^{1}H NMR spectrum of **17**, recorded in CD_3OD.*

The ^{13}C NMR spectrum also gave good results, revealing 40 distinct resonances of the 41 expected resonances (taking into account magnetic equivalence). Once again, the missing resonance was put down to one of the quaternary carbons of the guanine ring. Finally, the product was subjected to HRMS analysis, which yielded an output with an *m/z* value of 925.4420, consistent with the calculated value of the $[M+H]^+$ ion of 925.4395.

It was now possible to undertake the all-important EDC amide coupling reaction of **17** and auristatin-F, in order to produce the final ADC-precursor in this study. This reaction was carried out as per **Scheme 26**, in which anhydrous DMF was used as the reaction solvent and DMAP as the acyl transfer agent. EDC was selected as the coupling agent because it was not expected to produce any side products of similar polarity to the product and also due to its successful application multiple times in this study.

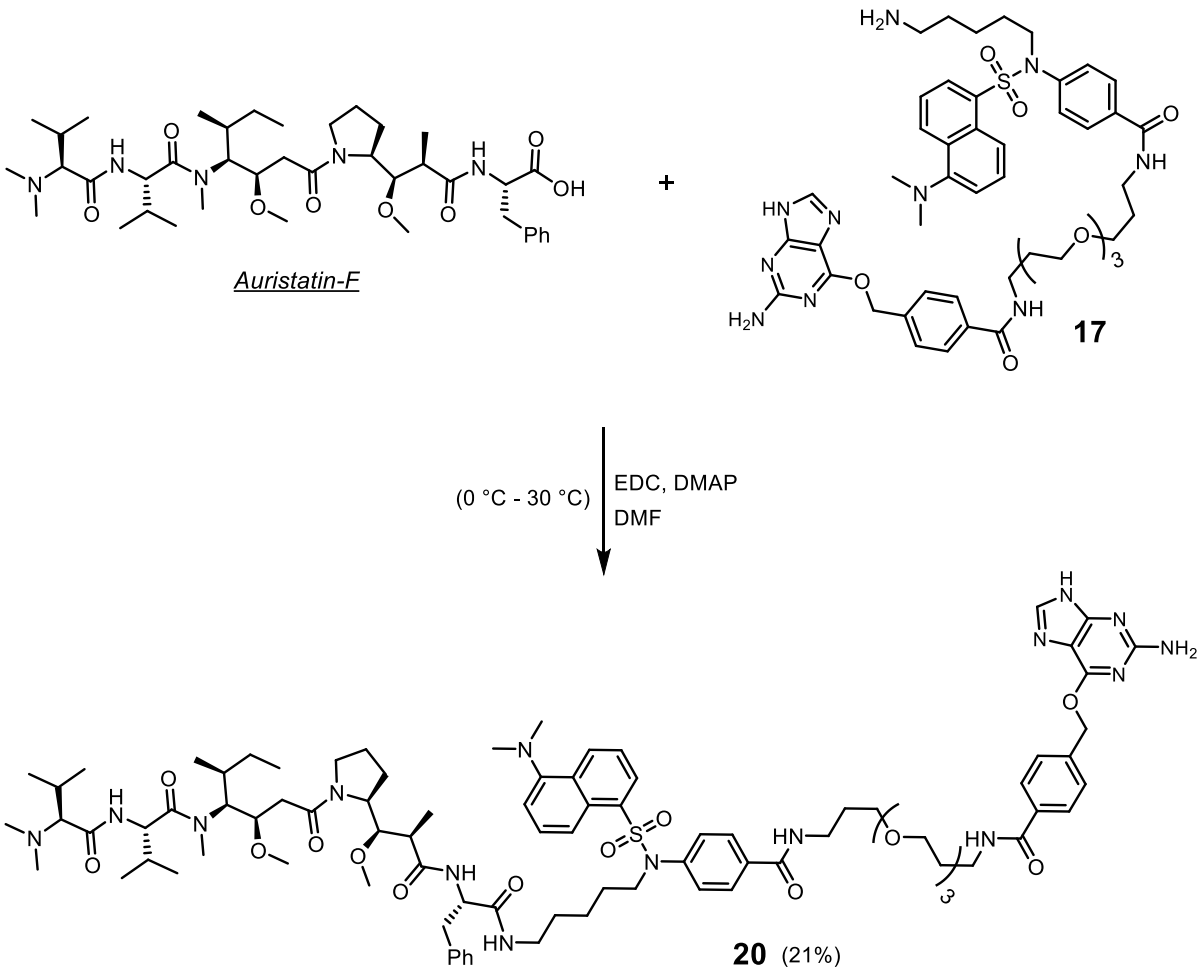

Scheme 26: *Amide coupling reaction of* ***17*** *and auristatin-F, resulting in the production of the final ADC-precursor (****20****).*

To this end, compound **17** (20 mg) was added in slight excess (1.1 eq) in order to fully consume the auristatin-F, and a dominant fluorescent product spot, with lower polarity than both starting materials, was visible on TLC within 6 hours. After 36 hours the reaction was deemed to be complete by virtue of the disappearance of Auristatin-F on TLC, the DMF subsequently removed *in vacuo* and the residue purified directly by column chromatography to afford 7 mg of a yellow solid, in 21% yield. The low yield was supported by the observation of multiple unidentified side products, present on TLC as fluorescent spots with varying polarity.

Following isolation of the reaction product, a sample was subjected to HPLC-UV analysis in which it was found to be 95.1% pure, with a retention time of 1.808 min using a 100% ACN mobile phase with an Agilent ZORBAX Eclipse Plus C-18 column. This result vindicated the synthesis efforts toward obtaining the fluorescent BG-linker by allowing for the product to be easily visible on TLC under 254 and 365 nm light, as well as providing accurate analytical purity data, which was not possible with the

previous construct. The HPLC-UV trace, recorded with the detector set to 254 nm, is presented in **Figure 51**.

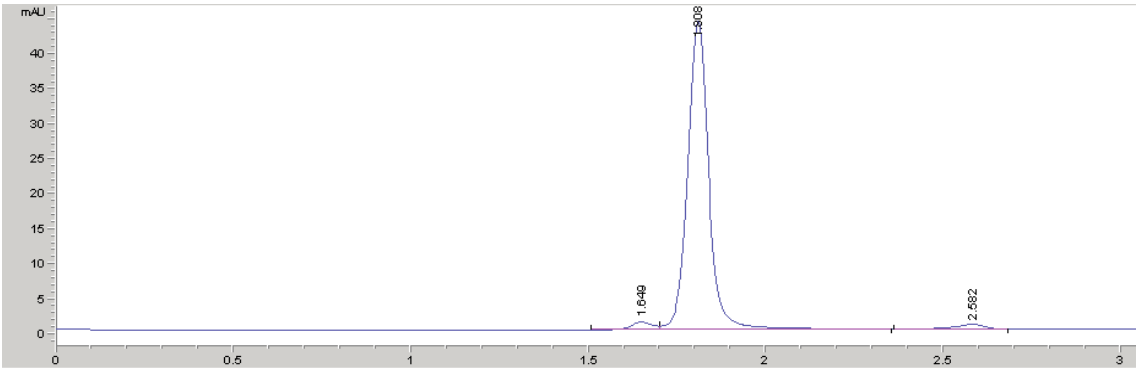

Retention Time	Area (mAU)	Area (%)
1.648	4.93726	2.5857
1.808	181.60587	95.1094
2.582	4.40107	2.3049

Figure 51: *HPLC-UV trace for the purified ADC-precursor construct* ***20****.*

The purity was considered to be sufficient for the characterisation and biological aspects of this study, the first of which was characterisation by ^{1}H NMR spectroscopy, for which the spectrum is displayed in **Figure 52**.

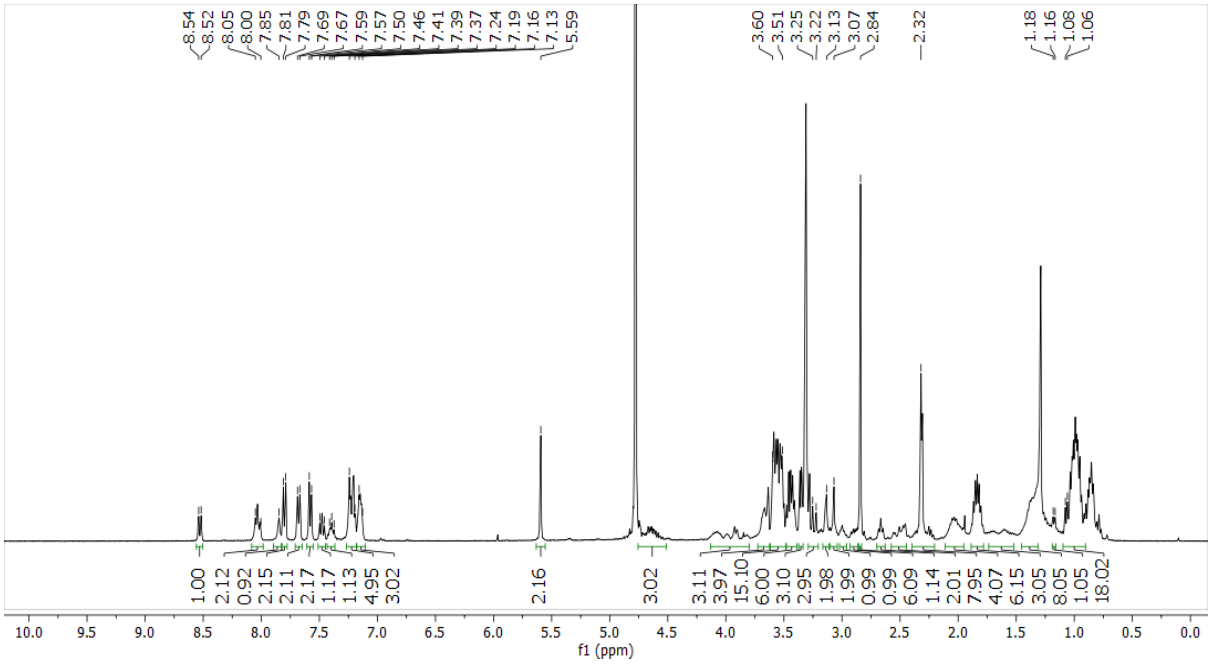

Figure 52: *^{1}H NMR spectrum of* ***20****, recorded in CD_3OD.*

An important milestone was realised upon first sight of this spectrum, which showed a good balance of signals for the two reactants. In depth analysis of the spectrum also revealed the presence of a single geometric isomer (configuration unknown as s-*cis* or s-*trans*). This was in line with the chromatography, which achieved separation of the

closely running major and minor compounds. More specifically, a sharp 2H singlet for the benzylic methylene hydrogens at 5.59 ppm could be immediately discerned, as well as highfield auristatin-F signals, which gave us confidence in the successful synthesis of **20**. As with **19**, the upfield region containing the complex auristatin-F broad multiplet signals (as well as those of the PEG and alkyl chain) was not highly resolved and as a result it was not possible to fully differentiate and assign all of the resonances. However, a sharp 6H singlet at 2.84 ppm could be assigned to the dimethylamino hydrogens on the dansyl tag, and a 6H singlet at 2.32 ppm was assigned as the auristatin-F N-terminal dimethylamino hydrogens. A downfield expansion of the spectrum was fully assigned and is displayed in **Figure 53**, allowing for comparison to the spectrum of **17**.

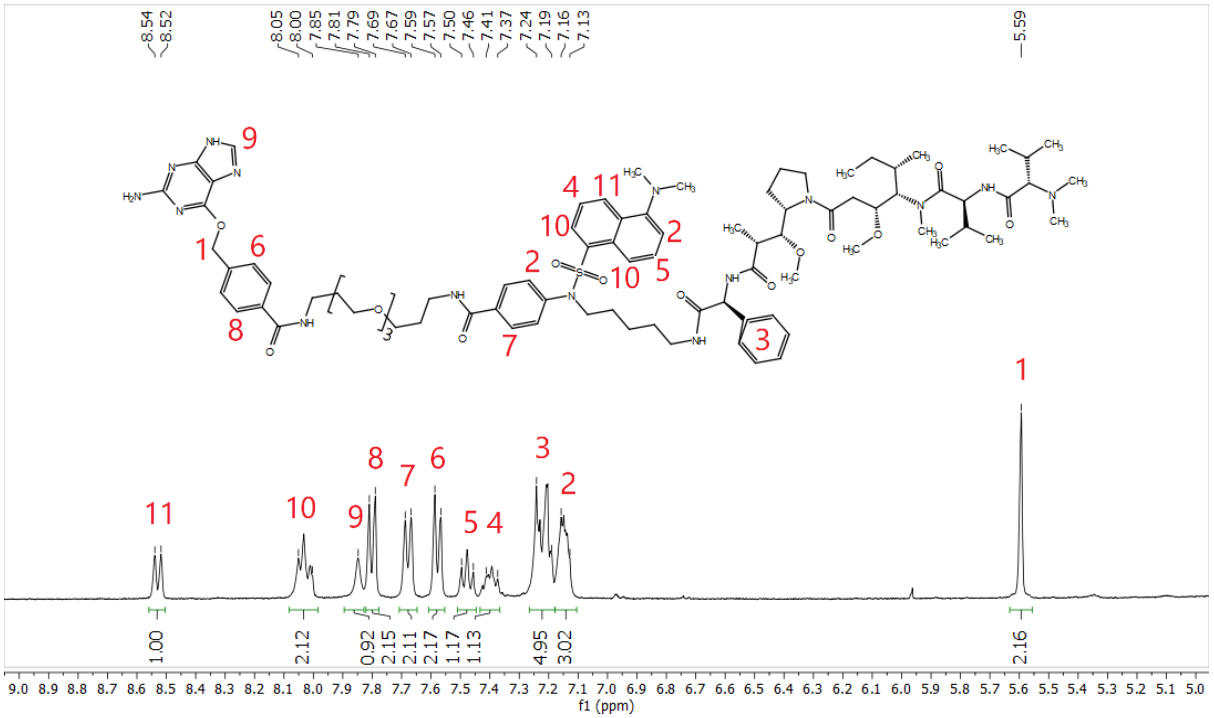

Figure 53: *Downfield expansion of the ^{1}H NMR spectrum of **20**, recorded in CD_3OD.*

The aromatic resonances resulting from **17** were clearly visible and among them an additional 5H multiplet (**3**) ranging from 7.19 – 7.24 ppm was assigned as the auristatin-F C-terminal phenyl ring, providing further evidence that auristatin-F was successfully coupled to the linker. Additionally, the lack of signal pairing in the spectrum provided further confirmation that a single rotamer had been isolated.

Further evidence for a successful coupling could be extrapolated from the ^{13}C NMR spectrum of **20**, which is presented in **Figure 54**. Since the ^{13}C spectrum was too complex to fully assign, emphasis was focused on identifying key resonances resulting from both **17** and auristatin-F.

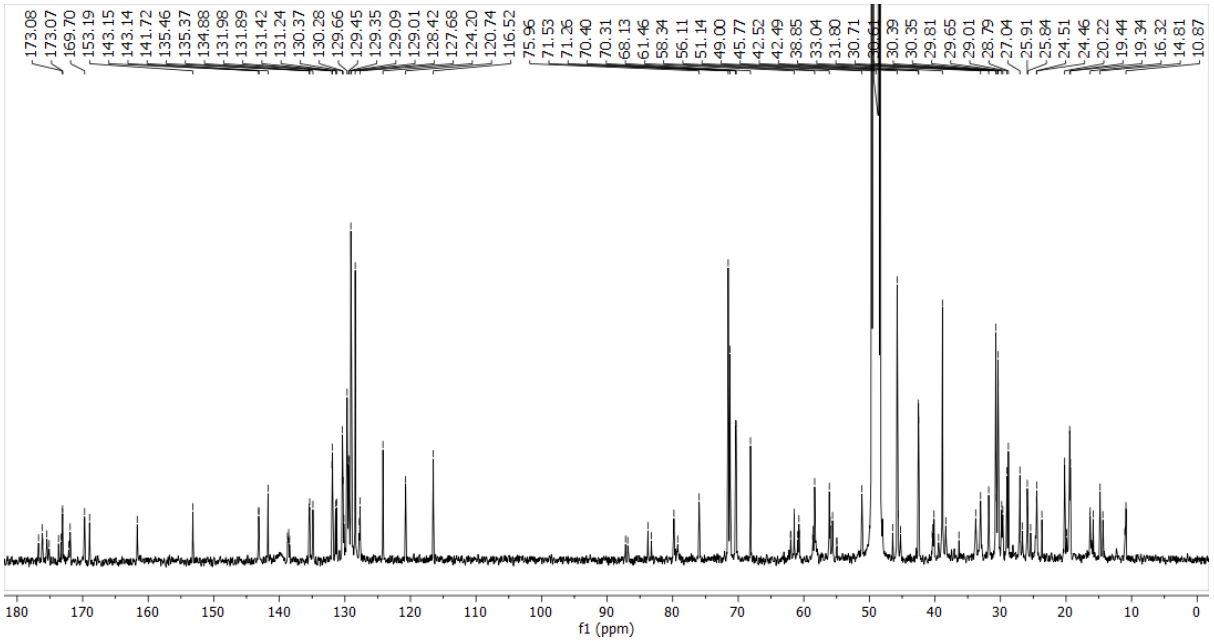

Figure 54: *^{13}C NMR spectrum of **20**, recorded in CD_3OD.*

An HSQC spectrum of **17** allowed for the identification of ^{13}C NMR spectroscopic resonances relating to key resonances in the corresponding ^{1}H NMR spectrum. The aromatic region of the HSQC spectrum of **17** is displayed in **Figure 55**, assigned numerically as per **Figure 50**.

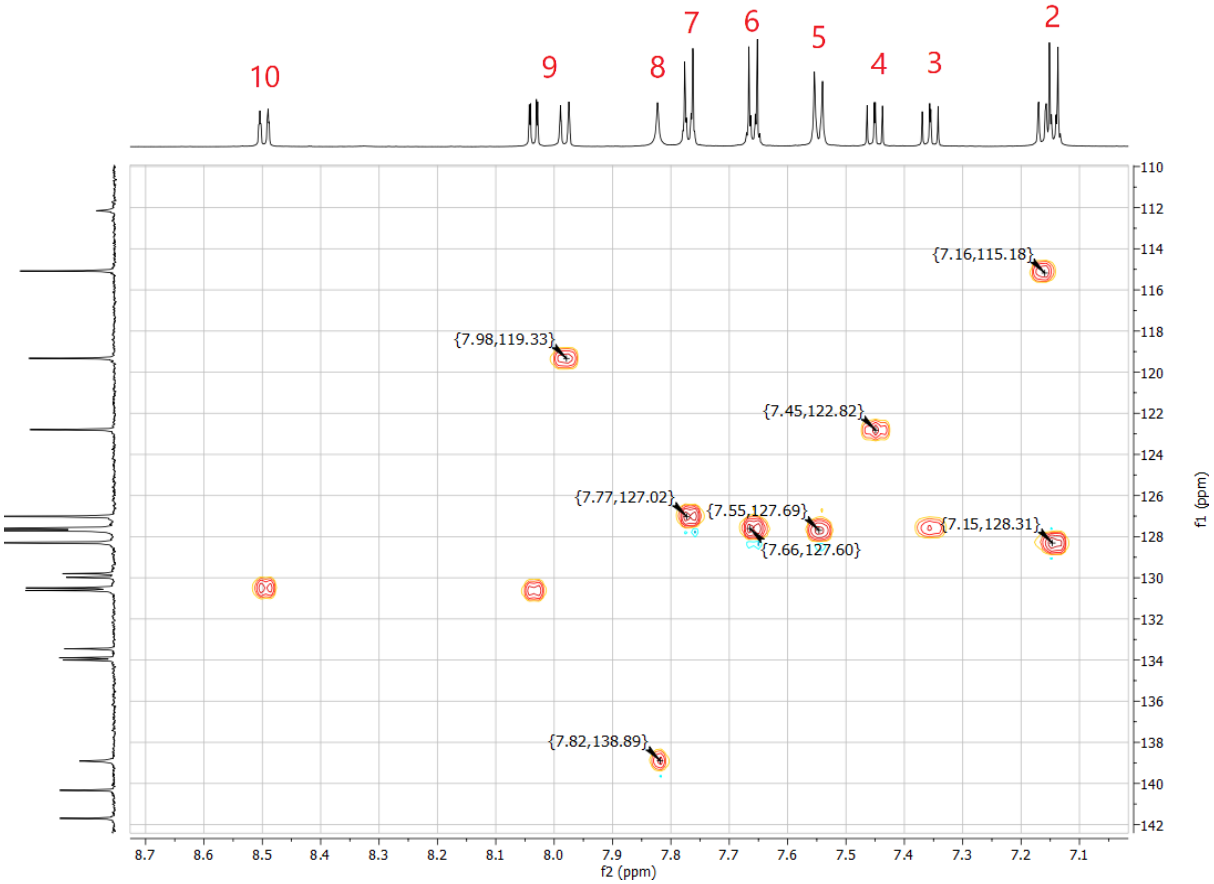

Figure 55: *Aromatic expansion of the HSQC spectrum of **17**.*

The two AA'BB' doublet pairs resulting from the BG moiety and the other 1,4-disubstituted ring in **17** correlated to four contiguous peaks in the ^{13}C NMR spectrum at 127.0, 127.6, 127.7 and 128.3 ppm, while the guanine methine signal correlated to a peak at 138.9 ppm. Furthermore, slightly downfield in the ^{13}C NMR spectrum were three peaks at 115.2, 119.3 and 122.8 ppm correlating to ^{1}H NMR resonances assigned to the dansyl naphthalene ring hydrogens. Inspection of the ^{13}C NMR spectrum of **20** from 110 – 145 ppm (**Figure 56**) allowed for the identification of all of these signals in the product, allowing for evidence that the all-important BG moiety and the dansyl tag were successfully installed.

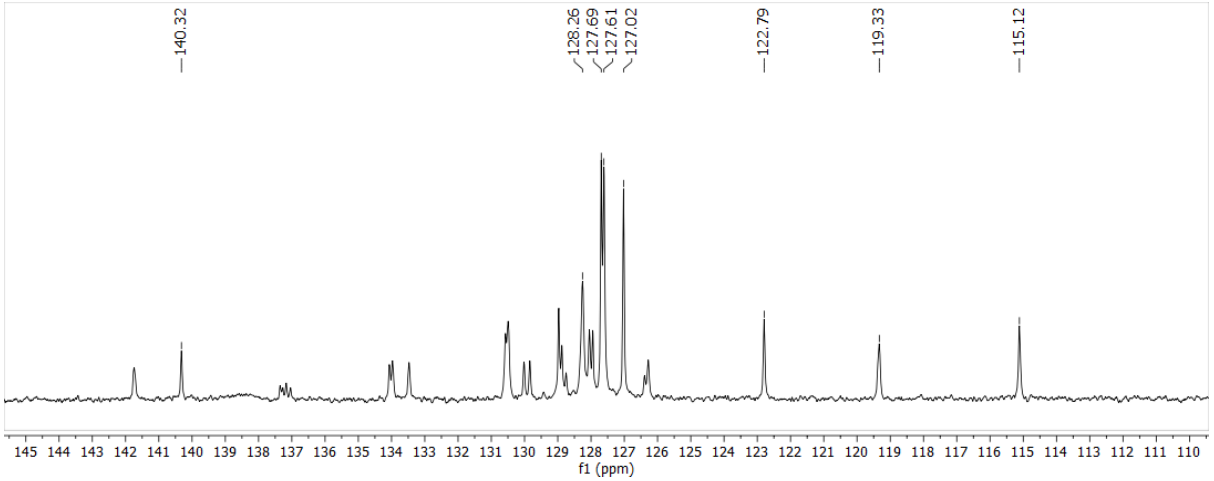

Figure 56: *An expansion of the ^{13}C NMR spectrum of **20**, from 110 – 145 ppm.*

Similar analysis of **20** resulted in identifying a ^{13}C NMR spectroscopic resonance at 66.7 ppm representing the benzylic methylene carbon, as well as the remaining signals of the linker. The remainder of the signals in the ^{13}C NMR spectrum of **20** (those not attributed to **17**) were compared to the ^{13}C NMR spectrum of auristatin-F, which showed good correlation and strongly supported the successful synthesis of **20**.

Finally, to further corroborate the successful synthesis of **20**, the product was admitted to HRMS analysis (**Figure 57**) where a peak was observed at an *m/z* value of 1675.9044, in line with the calculated value of the $[M+Na]^+$ adduct of **20** (1675.9093), within the previously discussed error bounds.

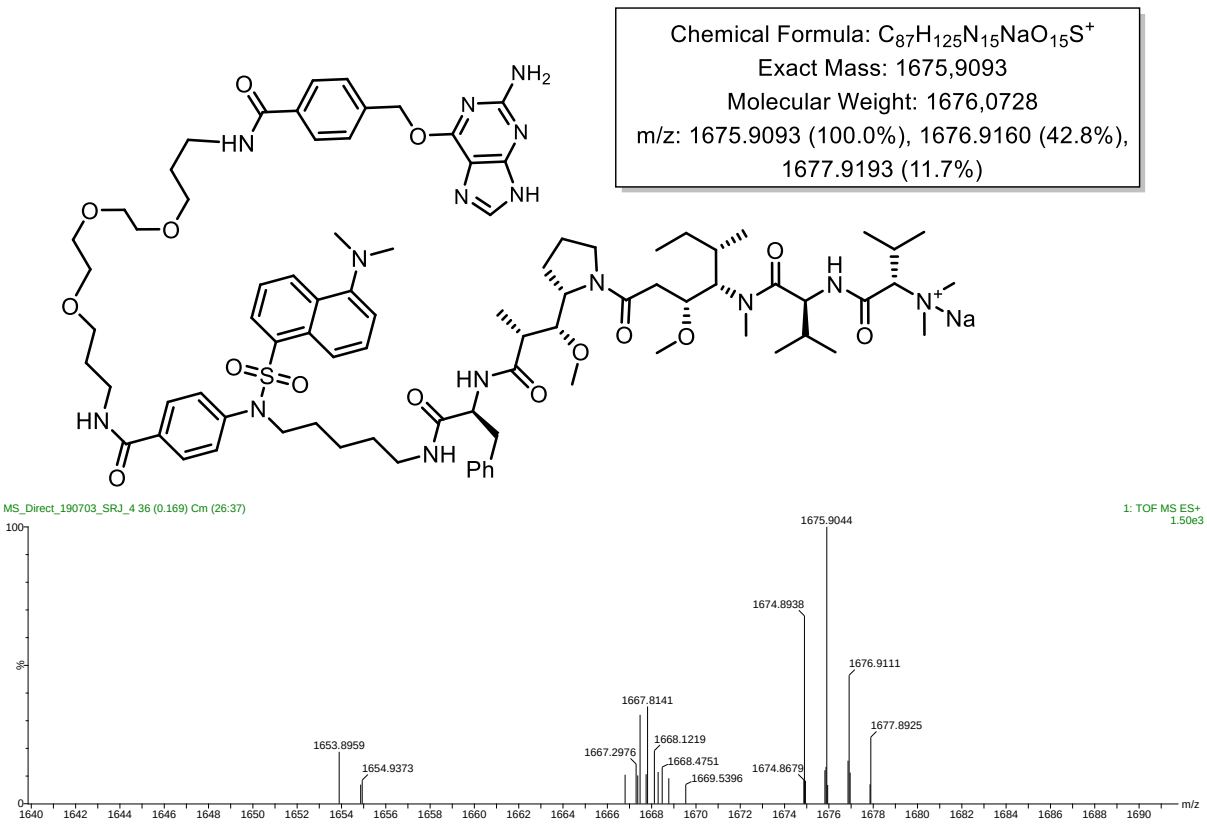

Figure 57: *HRMS output for* ***20*** *and the chemical structure of the* $[M+Na]^+$ *ion.*

The characteristics of the final construct, in terms of visibility and ease of purification, were much improved compared to those of construct **19,** and as a result it was possible to generate more conclusive data. However, during SNAP-tag conjugation and biological evaluation this compound was found to be extremely hydrophobic, the implications of which are discussed further in **Chapter Three**.

Both final ADC-precursor molecules, **19** and **20**, exhibited adequate stability at room temperature following isolation. This finding allowed for confidence that the integrity of the compounds would be upheld during the SNAP-tag conjugation reactions and subsequent purification steps.

This concluded the synthetic chemistry aspect of this study, which ultimately resulted in the production of two novel ADC-precursor constructs (**19** and **20**). The final aspect of this research involved SNAP-tag conjugation of **19** and **20** to scFv-SNAP fusion proteins, followed by biological evaluation of the resulting ADCs. The application of these ADC-precursor constructs was carried out within the academic group of Professor Stefan Barth, in the Medical Biotechnology and Immunotherapy Unit, Institute of Infectious Disease and Molecular Medicine, Faculty of Health Sciences, University of Cape Town.

Chapter Three: SNAP-Tag and Biological Evaluation

3.1 SNAP-Tag Conjugation

Following isolation of the ADC-precursor constructs generated in this study, conjugation to SNAP-tag fusion proteins was undertaken in order to evaluate the efficacy and potential of the resultant ADCs as cancer therapeutics. Recombinant SNAP-tag fusion proteins can be produced from either full immunoglobulins, mAbs or scFv antibody fragments, the latter being utilised for ADC generation in this study. Primary antigen targets for the scFv fragments utilised in this study were the EGFR, CSPG4 and CD44 receptors.

The biotechnology work contributing to the research output of this study was performed by Dr Fleury Augustin Nsole Biteghe and Ms Neelakshi Mungra of the Barth academic group. Results pertaining to fusion protein generation, SNAP-tag conjugation and biological evaluation using αEGFR(scFv)-SNAP fusion proteins are attributed to Dr Biteghe, while those concerning αCSPG4(scFv)-SNAP and αCD44(scFv)-SNAP fusion proteins are attributed to Ms Mungra.

3.1.1 Fusion protein preparation and isolation

Prior to the SNAP-tag conjugation reaction with BG-substrates, the scFv-SNAP fusion proteins were produced using recombinant DNA technology. The scFv gene sequences were obtained from collaborators and incorporated into an open reading frame (ORF) within a plasmid map, using SnapGene software (GSL Biotech LLC). The ORF is defined by a sequence of nucleotides that is actively recognised by DNA processing proteins and transcribed into mRNA - to ultimately be translated into the protein of interest. This sequence comprises a start codon, the scFv gene sequence, the SNAP-tag gene sequence and a stop codon. The ORF coding for the fusion protein was cloned into mammalian plasmids after which bacterial transformation was undertaken. Colonies containing the plasmid were selected for and sequenced in order to ensure that the plasmid was successfully ligated with the fusion protein ORF. This was followed by transfection in Hek293T cells, which express the plasmid and secrete the protein into the cell-culture supernatant. The supernatant was subsequently harvested and subjected to purification by Immobilised Metal Affinity Chromatography (IMAC). The IMAC stationary phase comprises metal ions immobilised via chelating ligands on the resin, which have Lewis acid character. The immobilisation of the target protein on the stationary phase is due to Lewis base character of certain amino acid side chains, such as those of cysteine and tryptophan. This immobilisation allows for impurities to be eluted before releasing the target protein by the introduction of imidazole to the

mobile phase, which competitively associates with the metal ions and displaces the fusion proteins.

In order to visualise the purified protein profile, SDS-polyacrylamide gel electrophoresis (SDS-PAGE) was performed with samples of the IMAC eluate, using a protein molecular weight ladder in order to approximate the molecular weight of the sample protein bands. The SDS-PAGE gel for visualisation of the eluate of one of the fusion proteins used in this study, αCSPG4(scFv)-SNAP (54 kDa), is displayed in **Figure 58**.

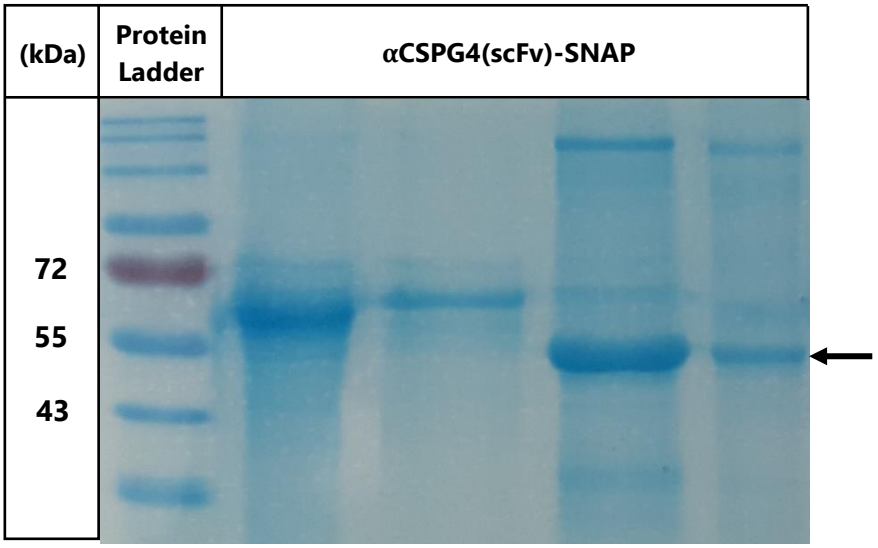

Figure 58: *SDS-PAGE gel for αCSPG4(scFv)-SNAP IMAC purification eluate, in which the target fusion protein (54 kDa) is present in lanes 4 and 5 marked by the black arrow. The gel displayed in this figure and the respective photograph was generated and supplied by Ms Mungra.*

After the pooling of appropriate fractions containing the target fusion protein, densitometry was performed with ImageJ software in order to ascertain the approximate protein concentration.

3.1.2 Conjugation reaction with BG-substrates

Following the preparation and purification of SNAP-tag fusion proteins, it was possible to undertake SNAP-tag conjugation reactions with BG-modified substrates. The conjugation reaction is typically carried out by introducing the BG-substrate into an aqueous buffer solution (with 4% DMSO v/v) containing the fusion protein (5 μM) as well as dithiothreitol (1 mM), a reducing agent. The standard reaction protocol required 2 molar equivalents of the BG-substrate, and the reaction was allowed to run for 2 hours at room temperature.

Prior to the conjugation reactions with the BG-modified auristatin-F constructs generated in this study, conjugation reactions with BG-Alexa488 were performed in order to verify the successful preparation of the fusion proteins. The chemical structure of BG-Alexa488, obtained from New England Biolabs, is displayed in **Figure 59**.

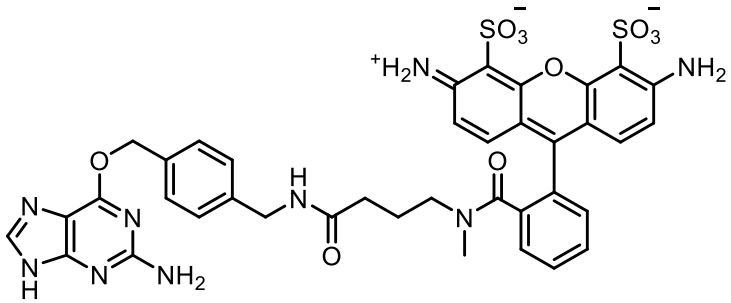

Figure 59: *The chemical structure of BG-Alexa488, a fluorescent BG-substrate used for SNAP-tag conjugation with scFv fusion proteins generated in this study.*

The BG-Alexa488 compound contains a highly delocalised fluorophore that allows for clear visualisation of the progress of the SNAP-tag conjugation reaction, as well as providing a means for visualisation of the combination product binding to target cells by use of confocal microscopy. In **Figure 60**, an SDS-PAGE gel of a sample of the SNAP-tag conjugation reaction between BG-Alexa488 and the αCSPG4(scFv)-SNAP fusion protein is displayed.

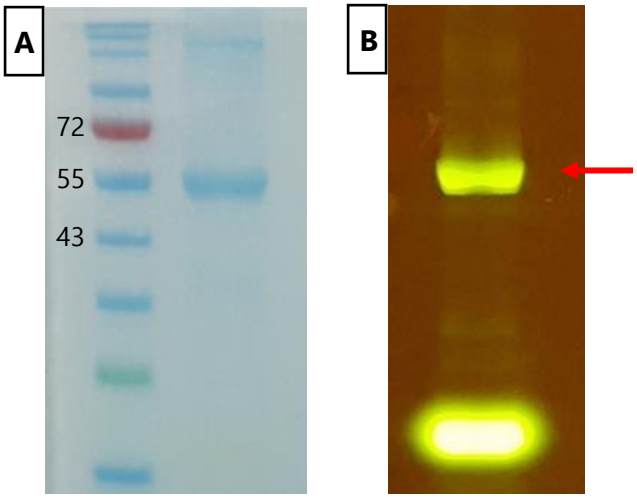

Figure 60: *SDS-PAGE gel for the SNAP-tag conjugation reaction of BG-Alexa488 and αCSPG4(scFv)-SNAP. Frame B displays a photograph taken upon irradiating the gel with visible blue light, in which the conjugation product is denoted by a red arrow. The gels displayed in this figure and the respective photographs were generated and supplied by Ms Mungra.*

In frame A, the fusion protein band (lane 2) was clearly visible at roughly 50 kDa according to the molecular weight ladder in lane 1; however, it was not possible to determine whether a successful conjugation reaction has taken place in this view as the conjugation product molecular weight is too similar to that of the unconjugated fusion protein. Upon irradiation of the gel with visible blue light (Frame B), the Alexa488 fluorophore fluoresced, confirming the conjugation reaction outcome. In frame B, unconjugated BG-Alexa488 substrate was seen near the base of the gel and conjugation was confirmed by the presence of a higher molecular weight fluorescent band around 50 kDa. Conjugation with BG-Alexa488 was performed for all generated fusion proteins, in which the presence of the conjugation product band allowed for confidence in both the success of the conjugation reaction as well as the integrity of the scFv-SNAP fusion proteins.

Finally, the conjugation reactions concerning the BG-modified auristatin-F constructs **19** and **20** were undertaken to yield the respective ADCs. The structures of the auristatin-F ADC targets for this study are displayed in **Figure 61**.

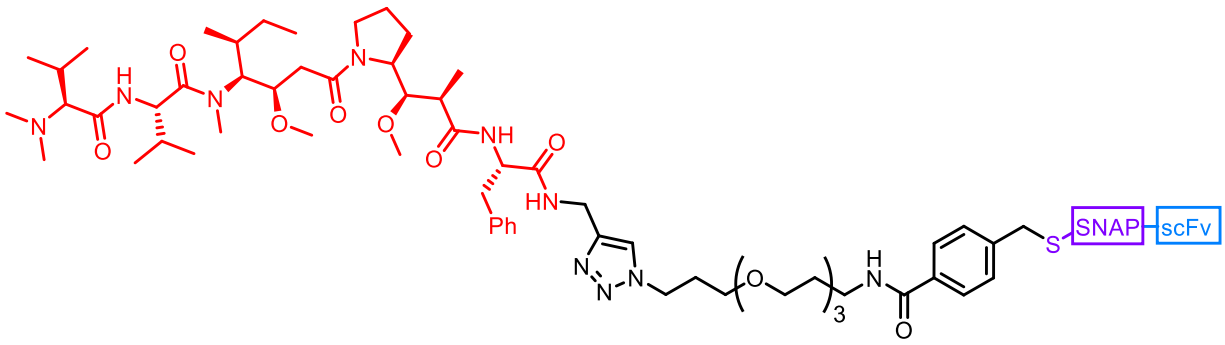

*SNAP-tag conjugation product with **19***

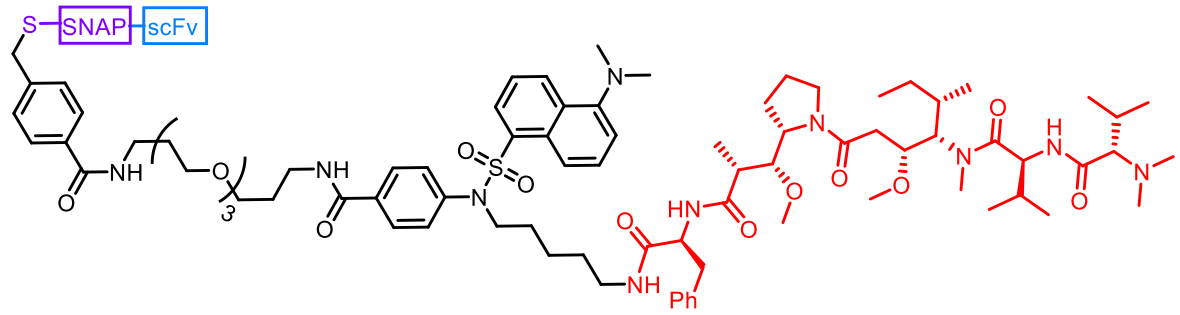

*SNAP-tag conjugation product with **20***

***Figure 61:** ADC SNAP-tag conjugation products of BG-modified auristatin-F ADC-precursor constructs generated in this study (**19** and **20**).*

The conjugation reactions were performed largely as per the standard protocol used for the conjugation with BG-Alexa488, with slight modification pertaining to the aqueous solubility of the ADC-precursor constructs. Since construct **19** was isolated quite some time before **20**, initial conjugation experiments were carried out with this molecule. It was necessary to increase the DMSO concentration of the conjugation reaction from 4% to 15%, in order to maximise the solubility of the BG-substrate and thus the conjugation efficiency, as **19** was not freely soluble in the standard 4% DMSO system. The reduced solubility of ADC-precursor constructs generated in this study, when compared to that of BG-Alexa488, could be attributed to an increased hydrophobicity due to having no charged groups, together with the possibility of aggregation and folding of the molecules in an aqueous system.

The need for solubility adjustments in SNAP-tag conjugation reactions with organic molecules was further exemplified when a conjugation reaction was attempted with **20**. Aqueous solubility experiments with **20** found that a DMSO concentration of approximately 80% was necessary in order to fully solubilise the molecule, which was unexpected due to its relatively high polarity observed during chromatography. This was attributed to the relatively non-polar dansyl tag, lending support about notions on conformation alluded to previously, in which minimisation calculations in aqueous media would be beneficial but were not carried out in this study. It has been shown that DMSO concentrations above 20% can lead to DMSO-induced protein unfolding, denaturation, aggregation or degradation.[143,144] Hence, in order to preserve the integrity of the SNAP-tag fusion proteins, it was not possible to fully solubilise **20** for SNAP-tag conjugation as per the standard protocol.

This stimulated thought into possible methods for augmenting the solubility of organic ADC-precursor molecules in aqueous media, without chemical modification of the substrate, which is currently an unaddressed problem in ADC research and development. This problem was addressed by the use of compatible solutes, or osmoprotectants, which are molecules utilised by various organisms in response to osmotic stress.[145] These molecules preserve the tertiary structure of proteins by facilitating the formation of hydration shells around the proteins via promoting hydrogen bonding between water and the substrate. This acts as a protectant against high concentrations of inorganic ions, which would act to unfold the proteins.[146] Compatible solutes have been recently adopted by our biotechnology group to preserve proteins during multiple freeze-thaw cycles, in which they have been successful in greatly improving protein integrity. The chemical structure of ectoine and

hydroxyectoine, two of the compatible solutes used in the group are displayed in **Figure 62**, along with their hydrogen bonding profile.

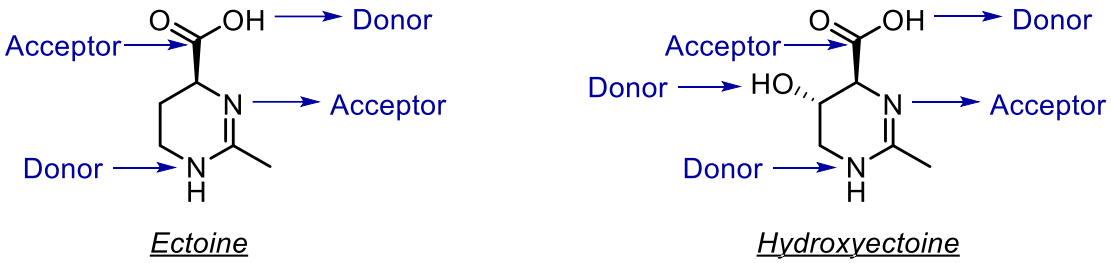

Figure 62: *The chemical structure of ectoine and hydroxyectoine, compatible solutes utilised in this study, together with their H-bonding profile.*

The stimulated formation of hydration shells by compatible solutes was interesting, as the use of detergents for enhancing the solubility of BG-substrates was previously considered. Ectoine was attractive as it contained both hydrogen bond acceptor and hydrogen bond donor sites (shown in **Figure 62**), potentially acting as a conduit between the BG-substrate and water, with a subsequent reduction in effective substrate hydrophobic character overall. The hypothesis was tested by assessing the aqueous solubility of the azido BG-linker **9**, visually, with and without ectoine supplementation. It was found that **9** did not dissolve in a 5% v/v DMSO aqueous solution while full dissolution was achieved upon supplementation with 1M ectoine. This experiment was also carried out with hydroxyectoine, another compatible solute, but ectoine displayed superior qualities for improving solubility. These findings were extrapolated to the SNAP-tag conjugation protocol, resulting in modification by supplementation of the conjugation reaction solution with ectoine (1M). This protocol was applied to the SNAP-tag conjugation reaction with **20**, in which a 15% DMSO concentration was employed. Visually, the solubility appeared to improve, although there was no accurate method established to definitively measure the extent of its dissolution.

3.1.3 Purification of combination products

Following completion of the conjugation reactions, a purification step was necessary to separate the conjugation product from unconjugated BG-substrate. This was achieved by size-exclusion chromatography, using 40K Zeba™ Spin Desalting Columns from ThermoFisher, which contain a high-performance size-exclusion resin with a 40 kDa molecular weight cut-off (MWCO) value. This resin allows unhindered passage of macromolecules with a molecular weight greater than 40 kDa, while retaining molecules with a molecular weight lower than 2 kDa. Here, only unconjugated fusion

protein and the conjugation product were expected to have a mass above 2 kDa, rendering this purification suitable to separate the ADCs. The purification was achieved by loading the conjugation reaction solution on top of the gel bed, which was followed by centrifugation in order to elute the protein into the internal reservoir. For cell viability assay calculation purposes, the eluate containing the conjugation product was assumed to be of equal concentration to that of the unconjugated fusion protein within the conjugation reaction (5 μM). This assumption could have been a source of error in the cytotoxicity values obtained for the isolated ADCs and could be improved on by further analysis after the purification step, which is outlined further in **Chapter Four**.

3.2 XTT-Based Cell Viability Assays

In order to ascertain the efficacy of the ADCs generated in this study, XTT cell viability assays were performed by treating various cell lines with the conjugation products generated in the SNAP-tag conjugation reactions. This assay allowed for determination of the fraction of viable cells in culture as determined by a colorimetric output, which was quantified by spectrophotometry and a corresponding IC_{50} value calculated. The latter value was representative of the concentration of the ADC required in order to achieve a 50% reduction in cell viability relative to the control cells, with the concentration value being inversely proportional to the efficacy of the ADC. The assays were performed by seeding specific cell lines in 96-well plates, which were allowed to adhere to the plate base at 37 °C overnight. Following the removal of the cell culture supernatant, the various wells were treated with PBS solutions containing decreasing concentrations of the ADC, as well as appropriate controls, and incubated for 72 hours. Finally, the XTT (Cell Proliferation Kit II) reagent was added to the cells, followed by another 4-hour incubation period, after which the absorbance values of each well were recorded.

The XTT reagent contains a colourless tetrazolium sodium salt, 2,3-bis(2-methoxy-4-nitro-5-sulfophenyl)-2*H*-tetrazolium-5-carboxanilide, which is reduced to a violet formazan derivative by dehydrogenase enzymes in living cells only (**Figure 63**). This conversion acts as a direct representation of cell viability, with absorbance values in treated cell cultures being directly proportional to cell viability.

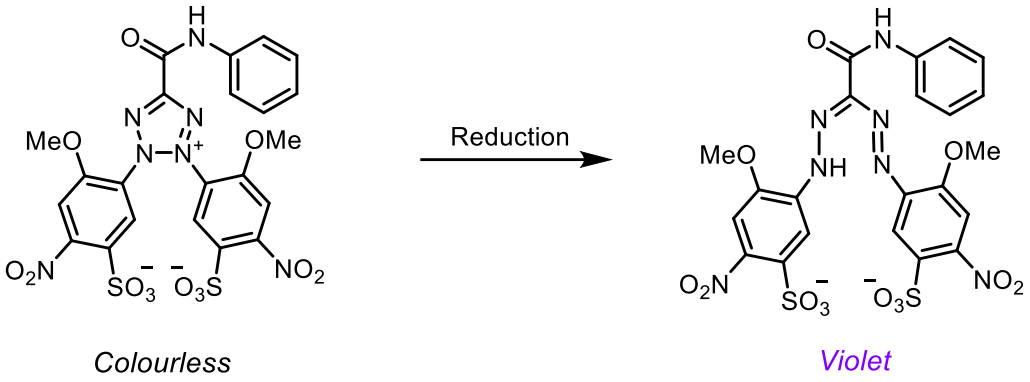

Figure 63: *Reduction of the colourless XTT reagent to a violet formazan dye product, achieved by dehydrogenase enzymes in living cells.*

3.2.1 XTT assay results

Following the isolation of the SNAP-tag conjugation product of **19** with αEGFR(scFv)-SNAP fusion proteins, XTT viability assays were conducted by the treatment of A431 ($EGFR^+$), SK-Mel-28 ($EGFR^+$), MDA-MB468 ($EGFR^+$) and A2058 ($EGFR^-$) cells. These cell lines were established from human epidermoid carcinoma, melanoma, breast metastatic adenocarcinoma and malignant melanoma, respectively. The results obtained from the XTT experiments are displayed in **Figure 64**, in the form of dose-response curves.

Separate control experiments were also undertaken, in which each cell line was subjected to a 2 μM concentration of the unconjugated ADC-precursor. In the control experiment, marginal toxicity was observed across all cell lines, in which cell viability did not decrease by more than 20%.

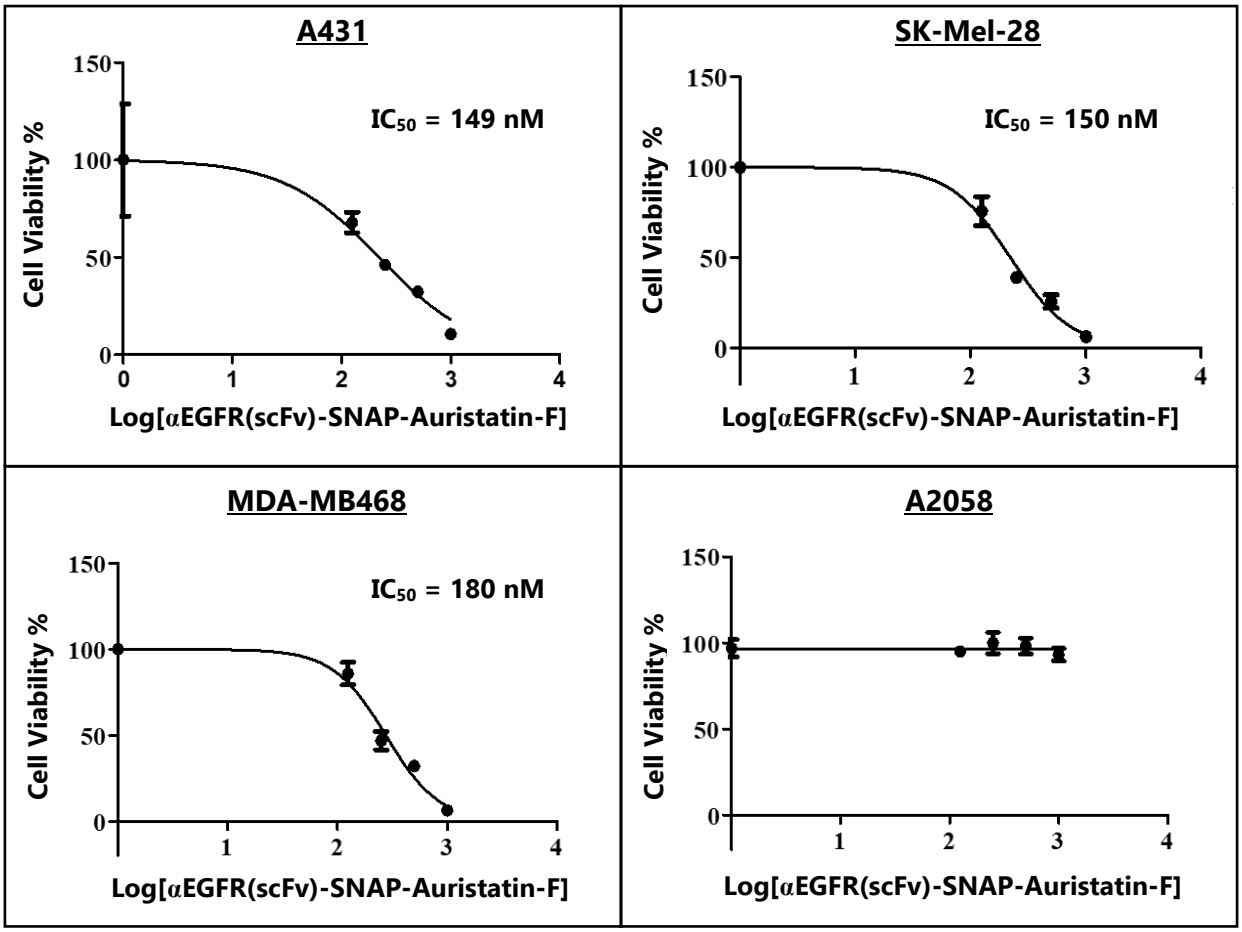

Figure 64: *XTT assay dose-response curves demonstrating the cytotoxic activity of αEGFR(scFv)-SNAP-Auristatin-F (of **19**) on A431, SK-Mel-28, MDA-MB468 and A2058 cells. The results displayed in this figure were generated and supplied by Dr Biteghe.*

These experiments were carried out in duplicate, at least three times, and the control cells of each cell line in these experiments were subjected to equal treatment except for the addition of the ADC. It can be seen that the ADC was effective in a dose-dependent manner, in nanomolar concentrations, for those cells possessing the EGFR target receptor (A431, SK-Mel-28 and MDA-MB468) and ineffective in eliminating cells which lacked the receptor (A2058).

The ADC-precursor construct **19** was also conjugated to αCD44(scFv)-SNAP and αCSPG4(scFv)-SNAP fusion proteins and the respective ADCs isolated. These ADC combination products were then applied in XTT assays with Hs578T (triple negative breast cancer) cells, which express both CSPG4 and CD44 antigens. The results obtained from these XTT experiments are displayed in the form of dose-response curves in **Figure 65**.

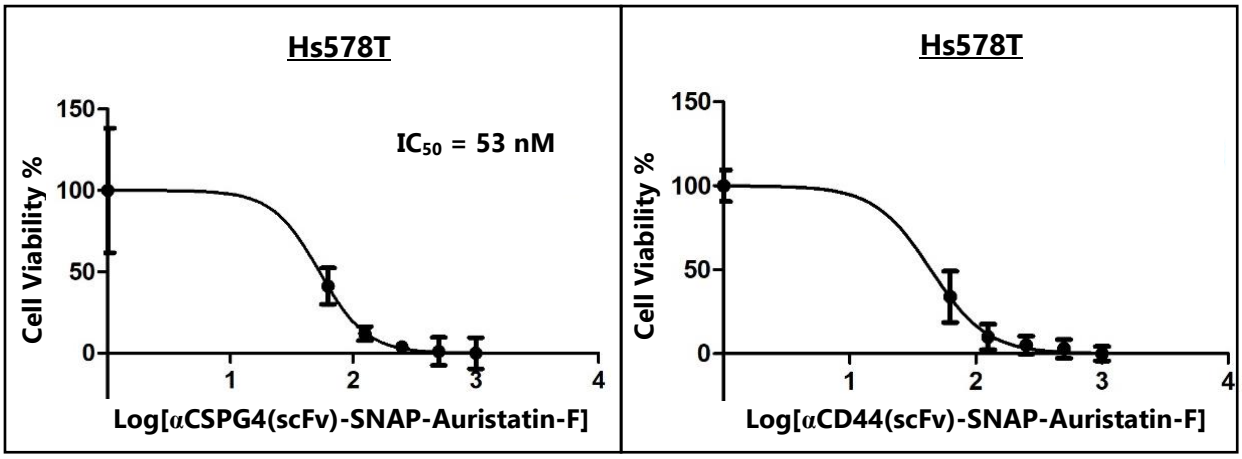

Figure 65: *XTT assay dose-response curves demonstrating the cytotoxic activity of αCSPG4(scFv)-SNAP-Auristatin-F and αCD44(scFv)-SNAP-Auristatin-F on Hs578T cells. The results displayed in this figure were generated and supplied by Ms Mungra.*

In these experiments, the synthesised recombinant ADC once again showed nanomolar activity in $CD44^+$ and $CSPG4^+$ cell lines. Overall, these results suggest a level of success for the ADCs involving **19** conjugated to scFv-SNAP fusion proteins targeting the EGFR, CD44 and CSPG4 epitopes. At this stage more research needs to be carried out in order to fully quantify efficacy, probably in comparison with mAb ADCs by treatment of an array of appropriate cell lines.

SNAP-tag conjugation and subsequent XTT viability assays were also performed with ADC-precursor **20**, but reproducible cytotoxicity results were not obtained. It was clear in XTT assay results that the isolated ADCs were exhibiting toxicity, but the standard deviations within replicates were too large to draw accurate conclusions on their actual cytotoxicity. It is unknown whether this may be attributed to the lack of conjugation efficiency due to the low solubility of **20** or due to other factors. This uncertainty necessitates further research into improving the understanding of the structural nuances that influence solubility, as well as improving the monitoring of SNAP-tag conjugation reactions, which will be discussed in **Chapter Four**.

Chapter Four: Conclusion and Future Research

Overall, this MSc study set out to synthesise a novel auristatin-F-based recombinant ADC, for evaluation as a potential cancer therapeutic by monitoring its cytotoxicity towards various cancer cell lines. The synthesis component involved first designing and synthesising a suitable BG-linker system to be covalently linked to auristatin-F. This was to be followed by biological studies involving SNAP-tag conjugation to scFv-SNAP fusion proteins, and *in vitro* cell viability assays of the resultant constructs for assessing the efficacy of the produced recombinant ADCs. Since this research was initially new to our group, a main goal was to gain insight and experience into the synthesis of BG-modified cytotoxins and their subsequent application in SNAP-tag conjugation. Initially, the various effects at play in producing a successful ADC were not fully understood, although the literature provided general guidance in important factors to consider in the design process.

The first challenge was to produce a non-cleavable BG-linker system allowing for successful coupling to auristatin-F, which was achieved successfully with two unique linker structures. Our first BG-modified auristatin-F ADC-precursor (**19**) was achieved via using CuAAC coupling between a propargylated auristatin-F derivative and an azido BG-linker; however, this construct lacked UV-activity and thus led to complications in isolation and determination of purity. Our second ADC-precursor (**20**), in which a dansyl fluorescent tag was incorporated into the linker, was afforded by amide coupling chemistry with auristatin-F, which allowed for improved visibility, thereby improving purification and characterisation results. The ADC-precursors were subjected to SNAP-tag conjugation with various scFv-SNAP fusion proteins, exhibiting specificity for the EGFR, CD44 and CSPG4 cancer-specific epitopes. The respective conjugation reaction combination products were admitted to XTT cell viability assays concerning various cell lines, either expressing or lacking the target epitopes. Here, the combination products incorporating **19** were found to exhibit cytotoxicity towards cell lines bearing the target antigen, with IC_{50} values ranging from 44 nM – 180 nM, and were ineffective in eliminating cells which lacked the target epitope. The combination products incorporating **20** failed to yield reproducible cytotoxicity data, which was postulated to be due to its hydrophobicity limiting solubility in the aqueous conjugation reaction solution, and thus leading to incomplete conjugation. The application of compatible solutes as a supplement in the SNAP-tag conjugation reaction solution was proposed to improve the aqueous solubility of the produced organic molecules produced in this study, in which ectoine provided positive results.

However, a quantitative method was not established to accurately determine the extent of solubility improvement.

Although multiple prototype auristatin-F-based recombinant ADCs were successfully produced in this MSc study, various insights were gained regarding possible modifications which could act to improve the properties of future products. Firstly, it is clear that focus needs to be directed towards understanding and evaluating the role of solubility in the conjugation protocol in respect to efficacy of the final construct. Increased solubility could be achieved by the incorporation of a greater number of hydrophilic functional groups in the linker structure, such as hydroxyl groups, phosphate groups or urea linkages, but crucially computational molecular modelling needs to be brought to bear to address the issue of ADC-precursor conformation and its role in the part. With this information, possible modifications to improve these characteristics could be assessed and implemented. In line with improving the UV-activity of auristatin-F-based ADC-precursors, the linker system could be modified to incorporate a suitable chromophore, while minimising the hydrophobicity resulting from such an addition, in conjunction with derivatives from molecular modelling. In addition, further research is required in order to quantify the advantages of compatible solutes on the aqueous solubility of organic ADC-precursors in the SNAP-tag conjugation reaction, which could be achieved by turbidimetric analysis of suitable organic molecules with a range of compatible solutes. Furthermore, greater reproducibility and insight into the SNAP-tag conjugation reaction itself could be achieved by developing analytical methodology for monitoring reaction progress in a more quantitative fashion. In turn, this could generate an SAR profile for establishing various rules for the design of effective ADCs. Finally, to allow for full confidence in the cytotoxic activity of the isolated ADCs it would be necessary to analyse the eluate of the SNAP-tag conjugation reaction purification step in both a quantitative and qualitative fashion. This would allow for accurately determining the concentration of the resultant ADCs, eliminating the need to make assumptions which could lead to skewed cytotoxicity data.

This MSc study has undoubtedly provided a foundation for future research into the generation of recombinant ADC therapeutics, by establishing methodology for the preparation of BG-modified auristatin-F constructs for application in SNAP-tag conjugation with scFv-SNAP fusion proteins. It has provided insights into multiple factors governing the successful preparation of ADCs and could ultimately be extrapolated to aid in the preparation of even more effective ADCs, in which other cytotoxins and BG-linker systems could be incorporated.

Chapter Five: Experimental Section

5.1 Materials and Equipment

All precursor chemicals were obtained commercially from Sigma Aldrich and used without further purification. All reaction solvents were freshly distilled under nitrogen before use and the removal of water was afforded by distilling over sodium wire for THF (with benzophenone as an indicator), P_2O_5 for DCM and CaH_2 for ACN, DMF and pyridine.

Visualisation was afforded by TLC, using Merck aluminium-backed silica 60 F_{254} plates and irradiation with short-wave (254 nm) or long-wave (365 nm) UV-light or by use of stains and subsequent heating. Anisaldehyde stain was prepared as a 2.5% solution of anisaldehyde in sulfuric acid and ethanol (1:10 v/v), ninhydrin stain was prepared as a 0.3% solution of ninhydrin in absolute ethanol and glacial acetic acid (97:3 v/v) and the $KMnO_4$ stain was prepared by dissolving 1.5 g of $KMnO_4$, 10 g K_2CO_3, and 1.25 mL 10% NaOH in 200 mL water.

Purification by column chromatography was carried out using silica gel 60 from Sigma Aldrich with the mobile phase comprising mixtures of MeOH and DCM or ethyl acetate (EtOAc) and Hexane. Purity data was afforded by high-performance liquid chromatography (HPLC) with a UV detector, using an Agilent 1220 unit equipped with an Agilent ZORBAX Eclipse Plus C-18 column.

Characterisation of isolated compounds by nuclear magnetic resonance (NMR) was performed on Varian Mercury 300 MHz, Bruker 400 MHz and Bruker 600 MHz spectrometers. Chemical shifts were recorded relative to residual methanol in CD_3OD (^{1}H NMR: δ3.31 ppm, ^{13}C NMR: δ49.00 ppm), residual chloroform in $CDCl_3$ (^{1}H NMR: δ7.26 ppm, ^{13}C NMR: δ77.16 ppm) and residual DMSO in DMSO-d_6 (^{1}H NMR: δ2.50 ppm, ^{13}C NMR: δ39.52 ppm). Infrared spectroscopy was performed on a PerkinElmer Spectrum Two FT-IR. Mass spectrometry was performed either by LC-MS or HRMS, the former using an Agilent 6120 Quadrupole system with positive ESI and the latter at the Central Analytical Facility at Stellenbosch University, using a Waters Synapt G2 system with an ESI probe in positive mode.

Compounds were named according to the IUPAC nomenclature system, generated automatically by PerkinElmer ChemDraw Professional 17.1.

5.2 Experimental Methods and Data

5.2.1 BG-linker Synthesis

4-{[(*tert*-Butyldimethylsilyl)oxy]methyl}benzoic acid[128] (1)

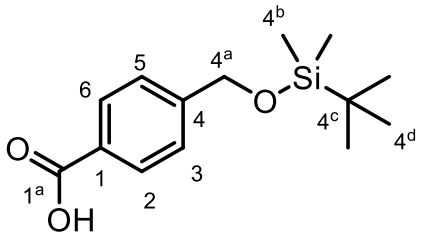

4-(Hydroxymethyl)benzoic acid (0.350 g, 2.30 mmol) and imidazole (0.314 g, 4.61 mmol) were taken up in anhydrous THF (6 mL) and stirred for 15 min under an argon atmosphere. TBSCl (0.694 g, 4.61 mmol) was added, upon which a white precipitate was formed, and the reaction stirred for 16 hours at rt. This reaction mixture was filtered and the filtrate concentrated, resulting in a pale-yellow oil. THF:H_2O (6 mL, 1:1) was then added, followed by K_2CO_3 (0.180 g, 1.30 mmol), and the solution stirred for 5 hours. This was followed by the addition of 0.5 M $KHSO_4$, until the evolution of precipitate halted, after which the organic acid was extracted into DCM (3 x 20 mL) and the extracts washed with brine (50 mL) and water (50 mL). The organic phase was dried over $MgSO_4$, followed by filtration, and concentrated by rotary evaporation to yield **1** as a colourless crystalline material (0.587 g, 96%). ^{1}H NMR δ (300 MHz, $CDCl_3$) 0.12 (s, 6H, H-4^b), 0.96 (s, 9H, H-4^d), 4.82 (s, 2H, H-4^a), 7.43 (d, 2H, *J* = 8.3 Hz, H-3 and H-5), 8.09 (d, 2H, *J* = 8.3 Hz, H-2 and H-6); ^{13}C NMR δ (100.6 MHz, $CDCl_3$) -5.1, 18.6, 26.1, 64.7, 126.0, 128.1, 130.4, 148.0, 172.0. The spectroscopic data of **1** matched that presented in literature.[128]

2,5-Dioxopyrrolidin-1-yl 4-{[(*tert*-butyldimethylsilyl)oxy]methyl}benzoate (2)

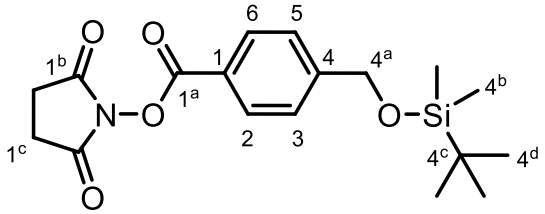

N-Hydroxysuccinimide (0.285 g, 2.48 mmol) and *N,N'*-dicyclohexylcarbodiimide (0.511 g, 2.48 mmol) were taken up in anhydrous ACN (15 mL), at 0 °C under an argon atmosphere, and stirred for roughly 10 min until dissolved. Compound **1** (0.550 g, 2.06 mmol) as well as DMAP (0.050 g, 0.41 mmol) were then added, along with anhydrous ACN (5 mL), the reaction allowed to warm to rt and stir for 12 hours. The resulting reaction mixture was placed at -20 °C for 3 hours, before filtering, after which the

filtrate was concentrated and purified by column chromatography (30% EtOAc/Hexane). The pure product was achieved as a pearly, colourless crystalline material (0.713 g, 95%). ^{1}H NMR δ (400 MHz, $CDCl_3$) 0.11 (s, 6H, H-4^{b}), 0.95 (s, 9H, H-4^{d}), 2.90 (s, 4H, H-1^{c}), 4.82 (s, 2H, H-4^{a}), 7.46 (d, 2H, J = 8.6 Hz, H-3 and H-5), 8.10 (d, 2H, J = 8.6 Hz, H-2 and H-6); ^{13}C NMR δ (100.6 MHz, $CDCl_3$) -5.2, 18.5, 25.9, 26.0, 64.6, 123.8, 126.2, 130.8, 149.4, 162.0, 169.3; IR 2941, 1741, 1214, 1072 cm^{-1}.

tert-Butyl (3-{2-[2-(3-aminopropoxy)ethoxy]ethoxy}propyl)carbamate[130] (3)

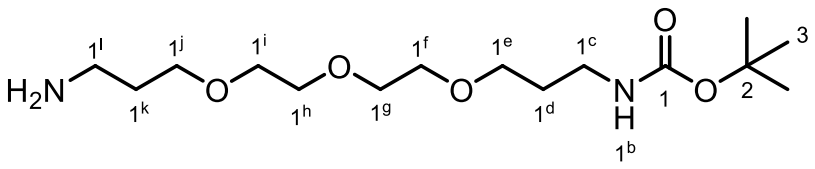

4,7,10-Trioxa-1,13-tridecanediamine (7.75 mL, 35.4 mmol) was taken up in anhydrous DCM (25 mL) and stirred under an argon atmosphere at rt. Di-*tert*-butyl dicarbonate (0.772 g, 3.54 mmol) dissolved in anhydrous DCM (10 mL) was added in a dropwise fashion and the resulting reaction mixture stirred for 3 hours at rt. The reaction mixture was subsequently reduced *in vacuo* and the residue purified by column chromatography (8% MeOH/DCM, 1% NEt_3) to yield an amber oil (1.065 g, 94%). ^{1}H NMR δ (300 MHz, $CDCl_3$) 1.35 (s, 9H, H-3), 1.45 (br s, 2H, NH_2), 1.59 – 1.71 (m, 4H, H-1^{d} and H-1^{k}), 2.71 (t, 2H, J = 6.7 Hz, H-1^{l}), 3.12 (app. q, 2H, J = 6.0 Hz, H-1^{c}), 3.43 - 3.58 (m, 12H, H-1^{e}, H-1^{f}, H-1^{g}, H-1^{h}, H-1^{i} and H-1^{j}), 5.16 (br s, 1H, H-1^{b}); ^{13}C NMR δ (100.6 MHz, $CDCl_3$) 28.4, 29.7, 33.3, 38.5, 39.6, 69.4, 70.2, 70.6, 78.7, 156.1, 2 signals not observed in spectrum; IR 1692, 1102 cm^{-1}. The spectroscopic data of **3** matched that presented in literature.[130]

tert-Butyl (3-{2-[2-(3-azidopropoxy)ethoxy]ethoxy}propyl)carbamate[130] (4)

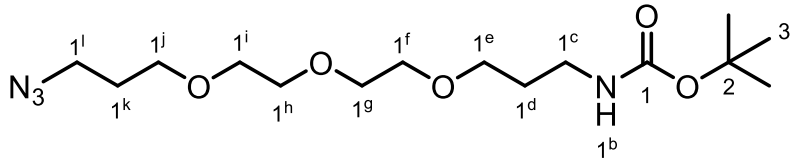

NaN_3 (0.930 g, 14.3 mmol) was taken up in H_2O (2.3 mL) to which toluene (2.3 mL) was added and the biphasic solution cooled to 0 °C. With vigorous stirring, triflic anhydride (1.55 mL, 9.21 mmol) was introduced in a dropwise manner and the reaction kept at 0 °C for 30 min. The temperature of the reaction was then allowed to rise to 10 °C and the stirring continued for a further 2 hours, after which a saturated, aqueous $NaHCO_3$ solution was added dropwise until the evolution of CO_2 halted. The toluene was separated and the resulting solution extracted twice with toluene (2.3 mL). Compound

3 (1.00 g, 3.12 mmol), $NaHCO_3$ (1.061 g, 12.63 mmol) and $Cu(II)SO_4{\cdot}5H_2O$ (0.030 g, 0.12 mmol) were then taken up in H_2O (4 mL), to which the triflic azide toluene extracts (7.0 mL) were added. This was followed by the addition of MeOH (27.0 mL) to afford a homogenous solution, which was stirred vigorously for 6 hours at rt. The organic solvents were removed *in vacuo* and the resulting aqueous solution extracted with DCM (3 x 10 mL) before drying with anhydrous $MgSO_4$, followed by filtration. The filtrate was subsequently adsorbed onto silica by rotary evaporation and the residue subjected to column chromatography (30% EtOAc/Hexane) to yield the product as a colourless oil (1.030 g, 95%). ^{1}H NMR δ (300 MHz, $CDCl_3$) 1.41 (s, 9H, H-3), 1.68 – 1.77 (m, 2H, H-1^k), 1.77 – 1.87 (m, 2H, H-1^d), 3.17 – 3.20 (m, 2H, H-1^l), 3.33 – 3.39 (m, 2H, H-1^c), 3.48 - 3.61 (m, 12H, H-1^e, H-1^f, H-1^g, H-1^h, H-1^i and H-1^j), 4.97 (br s, 1H, H-1^b); ^{13}C NMR δ (100.6 MHz, $CDCl_3$) 28.6, 29.3, 29.8, 38.7, 48.6, 68.0, 69.7, 70.4, 70.5, 70.7, 79.0, 156.2; IR 2095, 1701, 1109 cm^{-1}. The spectroscopic data of **4** matched that presented in literature.[130]

3-{2-[2-(3-Azidopropoxy)ethoxy]ethoxy}propan-1-amine[130] (5)

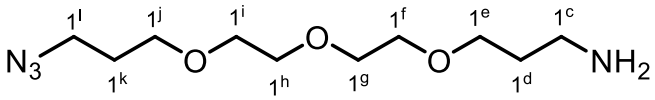

Compound **4** (1.00 g, 2.89 mmol) was taken up in anhydrous DCM (10 mL) and stirred under an argon atmosphere. To the resulting solution was added TFA (1.80 mL, 23.5 mmol), in a dropwise fashion, and the reaction was stirred for 5 hours at rt. Thereafter, the reaction mixture was reduced *in vacuo* and purified by flash chromatography (8% MeOH/DCM, 1% NEt_3) to yield **5** as an amber oil (0.625 g, 88%). ^{1}H NMR δ (300 MHz, $CDCl_3$) 1.65 – 1.81 (m, 4H, H-1^d and H-1^k), 2.73 – 2.77 (m, 2H, H-1^c), 3.14 (br s, 2H, NH_2), 3.30 (t, 2H, *J* = 6.7 Hz, H-1^l), 3.44 - 3.54 (m, 12H, H-1^e, H-1^f, H-1^g, H-1^h, H-1^i and H-1^j); ^{13}C NMR δ (100.6 MHz, $CDCl_3$) 29.0, 32.1, 39.2, 48.4, 67.8, 69.3, 70.1, 70.2, 70.4, 70.5; IR 2094, 1103 cm^{-1}. The spectroscopic data of **5** matched that presented in literature.[130]

N-(3-{2-[2-(3-Azidopropoxy)ethoxy]ethoxy}propyl)-4-{[(*tert*-butyldimethylsilyl)oxy]methyl}benzamide (6)

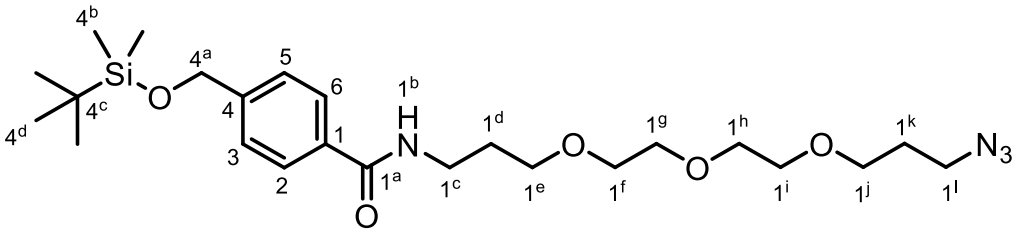

Compound **2** (1.00 g, 2.75 mmol) and **5** (0.680 g, 2.76 mmol) were taken up in anhydrous ACN (50 mL), under an argon atmosphere, and stirred for roughly 10 min at rt. DIPEA (1.30 mL, 7.46 mmol) was then added, the reaction warmed to 55 °C and stirred under reflux for 12 hours. The reaction mixture was adsorbed onto silica *in vacuo*, and the residue subjected to column chromatography (40-60% EtOAc/Hexane, elution gradient), yielding the product as an oil (1.250 g, 92%). ^{1}H NMR δ (300 MHz, $CDCl_3$) 0.10 (s, 6H, H-4^{b}), 0.94 (s, 9H, H-4^{d}), 1.80 (app. p, 2H, *J* = 6.5 Hz, H-1^{k}), 1.89 (app. p, 2H, *J* = 5.8 Hz, H-1^{d}), 3.34 (t, 2H, *J* = 6.5 Hz, H-1^{l}), 3.46-3.67 (m, 14H, H-1^{c}, H-1^{e}, H-1^{f}, H-1^{g}, H-1^{h}, H-1^{i} and H-1^{j}), 4.76 (s, 2H, H-4^{a}), 7.04 (br s, 1H, H-1^{b}), 7.36 (d, 2H, *J* = 8.4 Hz, H-3 and H-5), 7.76 (d, 2H, *J* = 8.4 Hz, H-2 and H-6); ^{13}C NMR δ (100.6 MHz, $CDCl_3$) -5.1, 18.5, 26.1, 29.1, 29.3, 39.1, 48.6, 64.7, 68.0, 70.5, 70.7, 70.9, 126.0, 127.1, 133.7, 145.0, 167.2, 2 signals not observed in spectrum. LC/MS (ES) *m/z*: $[M + H]^+$ Calcd for $C_{24}H_{43}N_4O_5Si$ 495.3; Found 495.2. IR 2096, 1640, 1092 cm^{-1}.

***N*-(3-{2-[2-(3-Azidopropoxy)ethoxy]ethoxy}propyl)-4-(hydroxymethyl)benzamide (7)**

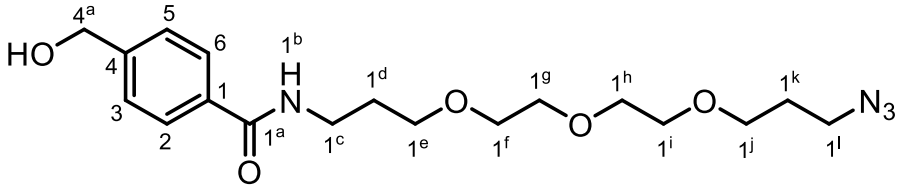

Compound **6** (0.860 g, 1.74 mmol) was dissolved in THF (20 mL) and stirred at 0 °C. To this solution was added 32% HCl (0.20 mL, 2.0 mmol), in a dropwise fashion, and the solution stirred for 45 min. The reaction was then allowed to warm to rt and stirred for an additional 2 hours. Thereafter, K_2CO_3 (1.00 g, 7.24 mmol) was added and the neutralisation allowed to proceed for 30 min before filtering. The filtrate was subsequently adsorbed onto silica *in vacuo* and the residue purified by column chromatography (100% EtOAc) to yield **7** as an oil (0.595 g, 90%). ^{1}H NMR δ (300 MHz, $CDCl_3$) 1.79 (app. p, 2H, *J* = 6.5 Hz, H-1^{k}), 1.85 – 1.92 (m, 2H, H-1^{d}), 2.44 (br s, OH), 3.33 (t, 2H, *J* = 6.5 Hz, H-1^{l}), 3.45-3.67 (m, 14H, H-1^{c}, H-1^{e}, H-1^{f}, H-1^{g}, H-1^{h}, H-1^{i} and H-1^{j}), 4.71 (d, 2H, *J* = 4.1 Hz, H-4^{a}), 7.14 (br s, 1H, H-1^{b}), 7.37 (d, 2H, *J* = 8.4 Hz, H-3 and H-5), 7.74 (d, 2H, *J* = 8.4 Hz, H-2 and H-6); ^{13}C NMR δ (100.6 MHz, $CDCl_3$) 29.0, 29.2, 39.2, 48.6, 64.8, 68.0, 70.3, 70.5, 70.6, 71.0, 127.0, 127.3, 134.1, 144.5, 167.2. LC/MS (ES) *m/z*: $[M + H]^+$ Calcd for $C_{18}H_{29}N_4O_5$ 381.2; Found 381.1. IR 3350, 2096, 1631, 1097 cm^{-1}.

1-(2-Amino-9*H*-purin-6-yl)-1-methylpyrrolidin-1-ium[134] **(8)**

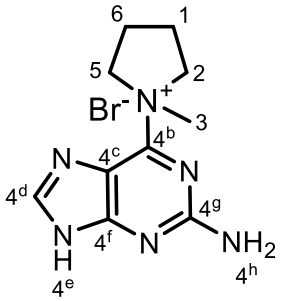

2-Amino-6-bromopurine (0.300 g, 1.40 mmol) was dissolved in anhydrous DMF (2 mL) and allowed to stir, under an argon atmosphere, for 10 min before the addition of *N*-methylpyrrolidine (0.40 mL, 3.9 mmol). The resulting reaction mixture was stirred for 48 hours, at rt, after which acetone was added until the evolution of precipitate halted. The heterogenous mixture was then filtered by gravity and the solid product washed with acetone before drying to yield **8** as a colourless crystalline material (0.350 g, 83%). ^{1}H NMR δ (400 MHz, DMSO-d_6) 2.00–2.11 (m, 2H, H-1/6), 2.20–2.31 (m, 2H, H-1/6), 3.65 (s, 3H, H-3), 3.94-4.00 (m, 2H, H-2/5), 4.57 – 4.64 (m, 2H, H-2/5), 7.07 (s, 2H, H-4^{h}), 8.33 (s, 1H, H-4^{d}), 13.26 (br s, 1H, H-4^{e}); ^{13}C NMR δ (100.6 MHz, DMSO-d_6) 21.4, 51.6, 64.1, 116.0, 142.9, 151.6, 158.5, 159.0. The spectroscopic data of **8** matched that presented in literature.[134]

4-{[(2-Amino-9*H*-purin-6-yl)oxy]methyl}-*N*-(3-{2-[2-(3-azidopropoxy)ethoxy]ethoxy}propyl)benzamide (9)

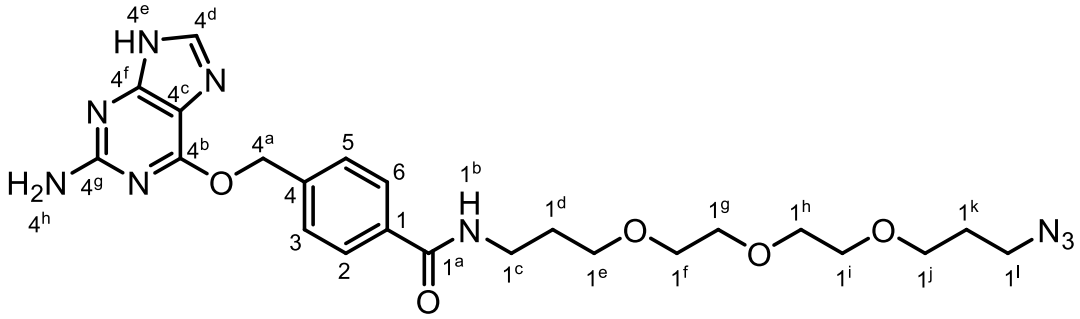

Compound **7** (0.300 g, 0.789 mmol) was taken up in freshly distilled, anhydrous DMF (4 mL) under an argon atmosphere, to which *t*-BuOK (0.450 g, 4.01 mmol) was added and the solution stirred for 30 min or until the solution had changed to a dark orange colour. Compound **8** (0.300 g, 1.00 mmol) was then added and the resulting reaction mixture allowed to stir for 4 hours at 27 °C. The DMF was then evaporated by use of a vacuum pump, the resulting concentrate adsorbed onto silica *in vacuo* and the residue subjected to column chromatography (5% MeOH/DCM) to furnish 9 as a waxy, colourless solid (0.280 g, 69%). ^{1}H NMR δ (300 MHz, $CDCl_3$) 1.77 (app. p, 2H, J = 6.6

Hz, H-1^{k}), 1.88 (app. p, 2H, *J* = 5.9 Hz, H-1^{d}), 3.31 (t, 2H, *J* = 6.6 Hz, H-1^{l}), 3.45 (t, 2H, *J* = 6.1 Hz, H-1^{c}), 3.48 - 3.63 (m, 12H, H-1^{e}, H-1^{f}, H-1^{g}, H-1^{h}, H-1^{i} and H-1^{j}), 5.16 (s, 2H, H-4^{h}), 5.48 (s, 2H, H-4^{a}), 7.30 (t, 1H, *J* = 4.9 Hz, H-1^{b}), 7.39 (d, 2H, *J* = 8.1 Hz, H-3 and H-5), 7.70 (d, 2H, *J* = 8.1 Hz, H-2 and H-6), 7.70 (s, 1H, H-4^{d}); ^{13}C NMR δ (100.6 MHz, $CDCl_3$) 29.0, 29.2, 38.9, 48.6, 67.5, 68.0, 70.4, 70.5, 70.6, 127.3, 128.0, 134.7, 139.7, 159.5, 167.5, 5 signals not observed in spectrum. LC/MS (ES) *m/z*: [M + H]$^{+}$ Calcd for $C_{23}H_{32}N_9O_5$ 514.3; Found 514.1. IR 2096, 1628, 1582, 1096 cm^{-1}.

5.2.2 Fluorescent BG-linker synthesis

4-{[(2-Amino-9*H*-purin-6-yl)oxy]methyl}-*N*-(3-{2-[2-(3-aminopropoxy)ethoxy]ethoxy}propyl)benzamide (10)

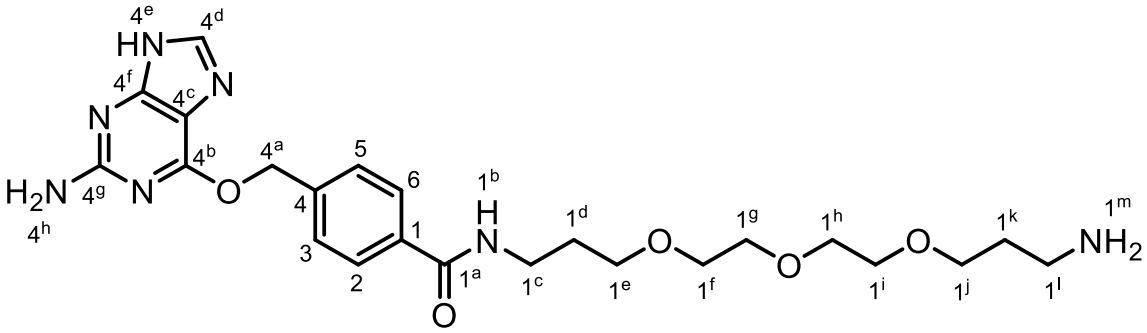

To compound **9** (0.115 g, 0.223 mmol), was added THF (3 mL) and water (0.3 mL) and the solution cooled to 0 °C. This was followed by the addition of PPh_3 (0.190 g, 0.724 mmol) and the resulting reaction allowed to warm naturally to rt to stir for 24 hours by which time the TLC analysis had revealed a full conversion of starting material. The resulting solution was evaporated *in vacuo* on to silica gel, which was used directly for column chromatography (10-20% MeOH/DCM, elution gradient) to yield **10** as a colourless solid (0.098 mg, 90%). ^{1}H NMR δ (600 MHz, CD_3OD) 1.75 (app. p, 2H, *J* = 6.0 Hz, H-1^{k}), 1.88 (app. p, 2H, *J* = 6.6 Hz, H-1^{d}), 2.82 (br s, 2H, H-1^{m}), 3.47 – 3.64 (m, 16H, H-1^{l}, H-1^{c}, H-1^{e}, H-1^{f}, H-1^{g}, H-1^{h}, H-1^{i} and H-1^{j}), 5.62 (s, 2H, H-4^{a}), 7.61 (d, 2H, *J* = 8.4 Hz, H-3 and H-5), 7.83 (d, 2H, *J* = 8.4 Hz, H-2 and H-6), 7.86 (s, 1H, H-4^{d}); ^{13}C NMR δ (151 MHz, CD_3OD) 30.4, 31.9, 38.8, 40.1, 68.1, 70.3, 70.4, 71.1, 71.3, 71.4, 71.5, 113.6, 128.4, 129.1, 135.4, 140.5, 141.8, 157.3, 161.3, 161.6, 169.8; LC/MS (ES) *m/z*: [M + H]$^{+}$ Calcd for $C_{23}H_{34}N_7O_5$ 488.3; Found 488.1. IR 3332, 2928, 2870, 1095 cm^{-1}.

Methyl 4-aminobenzoate[138] **(11)**

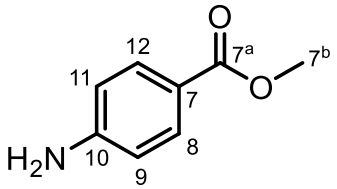

To a 50 mL round-bottomed flask at room temperature was added MeOH (17 mL), followed by the dropwise addition of acetyl chloride (0.62 mL, 8.7 mmol). The reaction was subsequently heated to 30 °C and allowed to stir for 30 min before the addition of *p*-aminobenzoic acid (0.800 g, 5.83 mmol). A reflux condenser was installed, the reaction warmed to 75 °C and stirred for an additional 5 hours. Upon cooling, the reaction mixture was added to a saturated $NaHCO_3$ solution (20 mL) and extracted with DCM (3 x 15 mL) before washing the pooled DCM extractions with water (2 x 20 mL). The organic extract was dried over $MgSO_4$, filtered, and the filtrate reduced *in vacuo* to yield **11** as a light yellow solid (0.868 g, 98%). ^{1}H NMR δ (300 MHz, $CDCl_3$) 3.85 (s, 3H, H-7b), 4.03 (br s, 2H, NH_2), 6.63 (d, 2H, *J* = 8.7 Hz, H-9 and H-11), 7.85 (d, 2H, *J* = 8.7 Hz, H-8 and H-12); IR 3406, 3330, 3227, 1680, 1275 cm^{-1}. The spectroscopic data of **11** matched that presented in literature.[138]

Methyl 4-{[5-(dimethylamino)naphthalene]-1-sulfonamido}benzoate[139] **(12)**

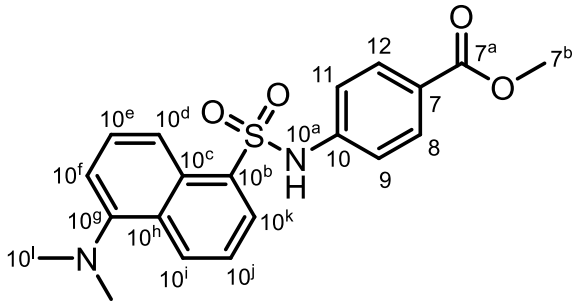

Compound **11** (0.380 g, 2.51 mmol) and dansyl chloride (0.450 g, 1.67 mmol) were taken up in anhydrous pyridine (15 mL), in a 25 mL round bottomed flask equipped with magnetic stirring, and allowed to reflux (115 °C) for 36 hours. The pyridine was subsequently removed *in vacuo* and the residue purified by column chromatography with neutralised silica (1% EtOAc/DCM) to yield **12** as a yellow solid (0.620 g, 97%). ^{1}H NMR δ (400 MHz, $CDCl_3$) 2.86 (s, 6H, H-10^l), 3.83 (s, 3H, H-7^b), 7.03 (d, 2H, *J* = 8.9 Hz, H-9 and H-11), 7.17 (d, 1H, *J* = 7.4 Hz, H-10^f), 7.44 – 7.48 (m, 2H, H-10^a and H-10^e), 7.56 (t, 1H, *J* = 7.9 Hz, H-10^j), 7.80 (d, 2H, *J* = 8.9 Hz, H-8 and H-12), 8.27 (d, 1H, *J* = 7.4 Hz, H-10^k), 8.34 (d, 1H, *J* = 8.7 Hz, H-10^d), 8.51 (d, 1H, *J* = 8.5 Hz, H-10^i); ^{13}C NMR δ (100.6 MHz, $CDCl_3$) 45.5, 52.1, 115.6, 118.4, 119.1, 123.2, 126.2, 129.0, 129.7, 130.1,

130.6, 131.1, 131.5, 134.0,141.2, 152.4, 166.5; IR 3244, 2941, 2850, 1689, 1280, 1140 cm^{-1}. The spectroscopic data of **12** matched that presented in literature.[139]

5-Azidopentan-1-ol[140] **(13)**

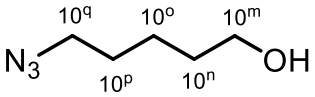

1,5-Pentanediol (10.00 g, 96.02 mmol) was taken up in DCM (50 mL) to which NEt_3 (66.7 mL, 480 mmol) was added and the solution cooled to 0 °C. Mesyl chloride (0.75 mL, 11 mmol) in DCM (20 mL) was added dropwise, with vigorous stirring. After the addition was complete, the reaction was stirred for 3 hours at rt before the removal of volatiles *in vacuo*. The residue was taken up in EtOAc (40 mL) and washed with brine (30 mL) followed by water (2 x 30 mL), to remove unreacted diol, before drying over $MgSO_4$. The extract was subsequently reduced *in vacuo* to yield the crude mono-mesylated product (1.200 g), which was first dried further under vacuum before being dissolved in anhydrous DMF (5 mL). Thereafter, NaN_3 (1.30 g, 20.0 mmol) and TBAI (0.250 g, 0.677 mmol) were added and the solution stirred for 12 hours at 60 °C. On cooling, the DMF was subsequently removed *in vacuo* and the residue suspended in DCM, adsorbed onto silica by rotary evaporation and the silica residue purified via column chromatography (30% EtOAc/Hexane) to yield **13** as a clear oil (0.600 g, 44%). ^{1}H NMR δ (600 MHz, $CDCl_3$) 1.42 – 1.47 (m, 2H, H-10^o), 1.56 – 1.65 (m, 5H, H-10^n and H-10^p and OH), 3.27 (t, 2H, *J* = 6.9 Hz, H-10^q), 3.64 (t, 2H, *J* = 6.5 Hz, H-10^m); ^{13}C NMR δ (151 MHz, $CDCl_3$) 23.1, 28.8, 32.3, 51.5, 62.7. IR 3358, 2097, 1016 cm^{-1}. The spectroscopic data of **13** matched that presented in literature.[140]

Methyl 4-{[*N*-(5-azidopentyl)-5-(dimethylamino)naphthalene]-1-sulfonamido}benzoate (14)

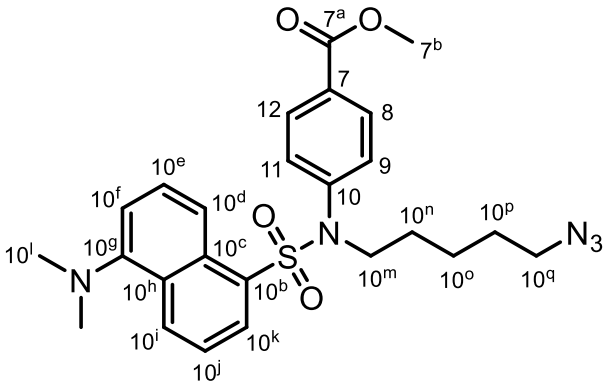

Compound **13** (0.150 g, 1.16 mmol), PPh_3 (0.307 g, 1.17 mmol) and compound **12** (0.300 g, 0.780 mmol) were taken up in anhydrous DCM (2 mL), under an argon

atmosphere, and stirred at rt. DIAD (0.237 g, 1.17 mmol) in anhydrous DCM (1 mL) was added dropwise and the resulting reaction allowed to stir for 3 hours. The solution was adsorbed onto silica by rotary evaporation after which the silica residue was purified by column chromatography (1% MeOH/DCM) to yield **14** as a yellow oil (0.317 g, 82%). ^{1}H NMR δ (400 MHz, $CDCl_3$) 1.34 – 1.39 (m, 2H, H-10^{o}), 1.45 – 1.52 (m, 4H, H-10^{n} and H-10^{p}), 2.88 (s, 6H, H-10^{l}), 3.17 (t, 2H, *J* = 6.8 Hz, H-10^{q}), 3.68 (t, 2H, *J* = 6.9 Hz, H-10^{m}), 3.90 (s, 3H, H-7^{b}), 7.13 – 7.18 (m, 3H, H-9 and H-11 and H-10^{f}), 7.36 – 7.44 (m, 2H, H-10^{e} and H-10^{j}), 7.90 (d, 2H, *J* = 7.9 Hz, H-8 and H-12), 8.06 – 8.08 (m, 2H, H-10^{k} and H-10^{d}); ^{13}C NMR δ (100.6 MHz, $CDCl_3$) 23.7, 28.0, 28.4, 45.6, 50.2, 51.3, 52.3, 115.4, 119.8, 123.2, 128.1, 128.5, 129.2, 130.1, 130.3, 130.5, 130.9, 131.1, 134.2, 143.5, 151.9, 166.5. LC/MS (ES) *m/z*: $[M + H]^+$ Calcd for $C_{25}H_{30}N_5O_4S$ 496.2; Found 496.1. IR 2954, 2094, 1722, 1262, 1096 cm^{-1}.

4-{[*N*-(5-Azidopentyl)-5-(dimethylamino)naphthalene]-1-sulfonamido}benzoic acid (15)

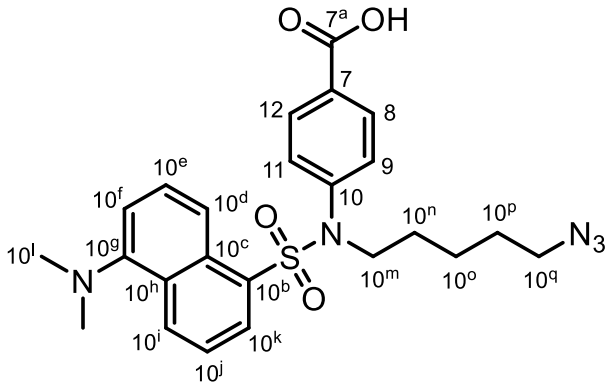

Compound **14** (0.180 g, 0.363 mmol) was dissolved in acetone (1.5 mL) and stirred at rt. A 2M NaOH solution (1.3 mL) was then added in a dropwise fashion and the resulting reaction allowed to stir for 4 hours. The acetone was removed *in vacuo* and to the residue was added water (5 mL) and 1M HCl to achieve a pH of 2. The resulting solution was extracted with EtOAc (3 x 5 mL) and washed with brine (10 mL) followed by water (10 mL) before the organic extracts were dried over $MgSO_4$. The dried organic extract was filtered to remove solids and reduced *in vacuo* to yield **15** as a yellow oil (0.175 mg, 100%). ^{1}H NMR δ (600 MHz, $CDCl_3$) 1.34 – 1.39 (m, 2H, H-10^{o}), 1.46 – 1.53 (m, 4H, H-10^{n} and H-10^{p}), 2.88 (s, 6H, H-10^{l}), 3.18 (t, 2H, *J* = 6.8 Hz, H-10^{q}), 3.69 (t, 2H, *J* = 7.0 Hz, H-10^{m}), 7.15 (d, 1H, *J* = 7.5 Hz, H-10^{f}), 7.22 (d, 2H, *J* = 8.6 Hz, H-9 and H-11), 7.39 (t, 1H, *J* = 7.6 Hz, H-10^{e}), 7.44 (t, 1H, *J* = 7.4 Hz, H-10^{j}), 7.98 (d, 2H, *J* = 8.5 Hz, H-8 and H-12), 8.03 (d, 1H, *J* = 8.7 Hz, H-10^{k}), 8.09 (d, 1H, *J* = 7.3 Hz, H-10^{d}), 8.52 (d, 1H, *J* = 8.5 Hz, H-10^{i}); ^{13}C NMR δ (151 MHz, $CDCl_3$) 23.7, 28.0, 28.4, 45.6, 50.1 51.3, 115.4, 119.7, 123.2, 128.1, 128.2, 128.5, 130.1, 130.3, 131.0, 131.1, 131.1, 134.0, 144.3,

151.9, 170.4. LC/MS (ES) *m/z*: $[M + H]^+$ Calcd for $C_{24}H_{28}N_5O_4S$ 482.2; Found 482.0. IR 3296, 2935, 2094, 1705, 1246, 1102 cm^{-1}.

4-{[(2-Amino-9*H*-purin-6-yl)oxy]methyl}-*N*-[1-(4-{[*N*-(5-azidopentyl)-5-(dimethylamino)naphthalene]-1-sulfonamido}phenyl)-1-oxo-6,9,12-trioxa-2-azapentadecan-15-yl]benzamide (16)

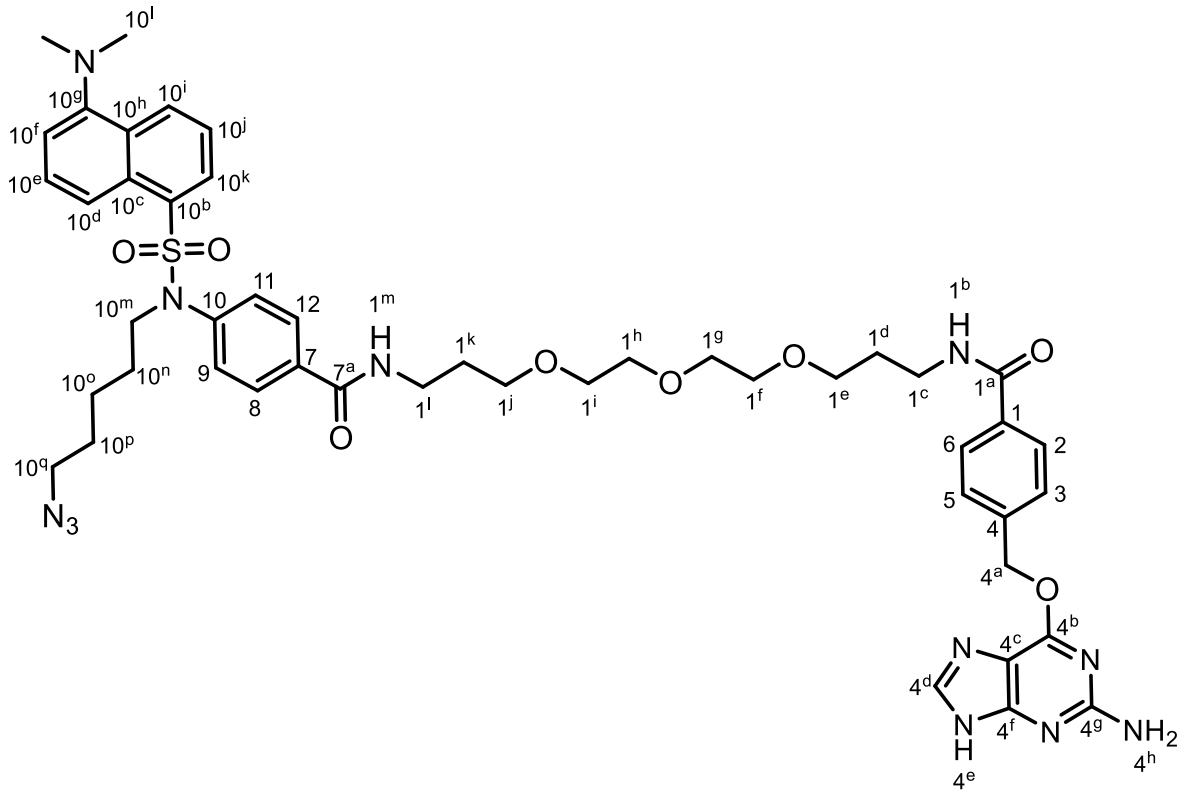

Compound **15** (0.100 g, 0.208 mmol) and EDC·HCl (0.060 g, 0.31 mmol) were taken up in anhydrous DMF (3.0 mL), under an argon atmosphere, and allowed to stir for 30 mins. With stirring, was added **10** (0.110 g, 0.224 mmol) and DMAP (0.009 g, 0.07 mmol) in anhydrous DMF (3 mL) and the reaction stirred for 36 hours at 30 °C. The DMF was subsequently removed *in vacuo* and the residue adsorbed onto silica by rotary evaporation before being subjected to column chromatography with neutralised silica (4% MeOH/DCM) to yield **16** as a yellow oil (0.114 g, 58%). ^{1}H NMR δ (600 MHz, $CDCl_3$) 1.28 – 1.32 (m, 2H, H-10^o), 1.38 – 1.46 (m, 4H, H-10^n and H-10^p), 1.77 – 1.88 (m, 4H, H-1^k and H-1^d), 2.86 (s, 6H, H-10^l), 3.13 (t, 2H, *J* = 6.8 Hz, H-10^q), 3.47 – 3.62 (m, 18H, H-10^m, H-1^c, H-1^l, H-1^e, H-1^f, H-1^g, H-1^h, H-1^i and H-1^j), 4.97 (s, 2H, H-4^h), 5.53 (s, 2H, H-4^a), 7.13 (d, 1H, *J* = 7.5 Hz, H-10^f), 7.15 (d, 2H, *J* = 8.6 Hz, H-9 and H-11), 7.31 (br s, 1H, H-1^m), 7.37 – 7.45 (m, 5H, *J* = 7.5 Hz, H-10^e, H-10^j, H-3, H-5 and H-4^d), 7.65 (br s, 1H, H-1^b), 7.70 (d, 2H, *J* = 8.6 Hz, H-8 and H-12), 7.75 (d, 2H, *J* = 8.2 Hz, H-2 and H-6), 8.05 – 8.07 (m, 2H, H-10^k and H-10^d), 8.50 (d, 1H, *J* = 8.5 Hz, H-10^i); ^{13}C NMR δ (151 MHz, $CDCl_3$) 23.6, 27.8, 28.4, 29.0, 29.0, 38.9, 39.1, 45.6, 50.3, 51.3,

67.5, 70.3, 70.5, 70.5, 70.8, 115.4, 119.7, 123.2, 127.4, 128.0, 128.1, 128.1, 128.9, 130.1, 130.2, 131.0, 131.1, 134.1, 134.7, 139.7, 141.7, 151.9, 159.5, 166.8, 167.2, 5 signals not observed in spectrum. HRMS (ES) *m/z*: $[M + H]^+$ Calcd for $C_{47}H_{59}N_{12}O_8S$ 951.4300; Found 951.4293. IR 3342, 2921, 2095, 1630, 1458, 1259, 1086, 1015 cm^{-1}.

4-{[(2-Amino-9*H*-purin-6-yl)oxy]methyl}-*N*-[1-(4-{[*N*-(5-aminopentyl)-5-(dimethylamino)naphthalene]-1-sulfonamido}phenyl)-1-oxo-6,9,12-trioxa-2-azapentadecan-15-yl]benzamide (17)

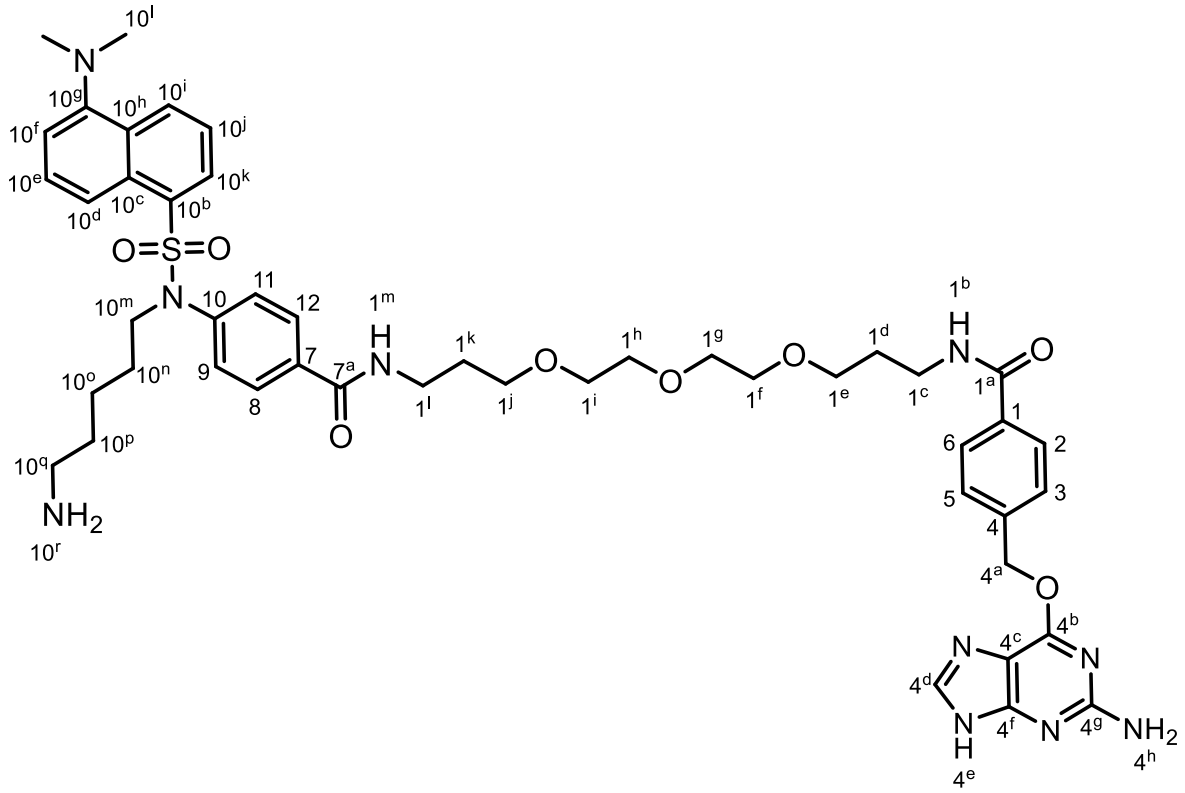

To compound **16** (0.100 g, 0.105 mmol) was added THF (1.5 mL) and water (0.15 mL) and the solution cooled to 0 °C. This was followed by the slow addition of PPh_3 (0.100 g, 0.381 mmol) and the resulting reaction was allowed to warm naturally to rt to stir for 24 hours. The resulting solution was reduced *in vacuo* onto silica and the residue purified by column chromatography (1-10% MeOH/DCM) to yield **17** as a yellow solid (0.058 g, 60%). ^{1}H NMR δ (600 MHz, $CDCl_3$) 1.29 – 1.32 (m, 2H, H-10^o), 1.38 – 1.43 (m, 4H, H-10^n and H-10^p), 1.79 – 1.87 (m, 4H, H-1^k and H-1^d), 2.60 (br s, 2H, H-10^r), 2.83 (s, 6H, H-10^l), 3.41 – 3.46 (m, 4H, H-1^c and H-10^q), 3.50 – 3.60 (m, 14H, H-1^l, H-1^e, H-1^f, H-1^g, H-1^h, H-1^i and H-1^j), 3.69 (t, 2H, *J* = 6.8 Hz, H-10^m), 5.59 (s, 2H, H-4^a), 7.16 – 7.20 (m, 3H, H-10^f, H-9 and H-11), 7.38 (t, 1H, *J* = 7.5 Hz, H-10^e), 7.48 (t, 1H, *J* = 7.5 Hz, H-10^j), 7.57 (d, 2H, *J* = 8.5 Hz, H-3 and H-5), 7.68 (d, 2H, *J* = 8.8 Hz, H-8 and H-12), 7.79 (d, 2H, *J* = 8.5 Hz, H-2 and H-6), 7.85 (s, 1H, H-4^d), 8.01 (d, 1H, *J* = 8.7 Hz, H-10^k), 8.06 (d, 1H, *J* = 7.3 Hz, H-10^d), 8.52 (d, 1H, *J* = 8.5 Hz, H-10^i); ^{13}C NMR δ (151 MHz, $CDCl_3$) 24.5,

29.0, 30.3, 30.4, 31.5, 38.8, 41.8, 45.8, 51.1, 64.4, 68.1, 70.3, 70.3, 71.2, 71.3, 71.5, 73.9, 113.6, 116.5, 120.7, 124.2, 128.4, 129.0, 129.1, 129.7, 131.2, 131.4, 131.9, 132.0, 134.9, 135.3, 135.4, 140.3, 141.7, 143.1, 153.1, 157.2, 161.2, 161.6, 169.0, 169.7. HRMS (ES) *m/z*: $[M + H]^+$ Calcd for $C_{47}H_{61}N_{10}O_8S$ 925.4395; Found 925.4420. IR 3324, 2926, 1624, 1576, 1317, 1134, 1092 cm^{-1}.

5.2.3 MMAF Derivatisation

{(2*R*,3*R*)-3-[(*S*)-1-((3*R*,4*S*,5*S*)-4-{(*S*)-2-[(*S*)-2-(Dimethylamino)-3-methylbutanamido]-*N*,3-dimethylbutanamido}-3-methoxy-5-methylheptanoyl)pyrrolidin-2-yl]-3-methoxy-2-methylpropanoyl}-*L*-phenylalanine (Auristatin-F)

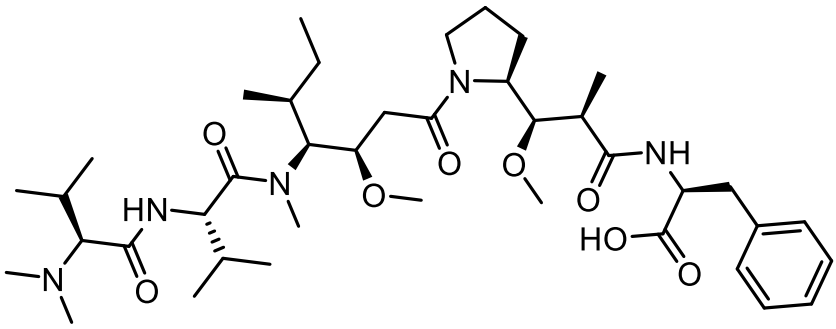

MMAF (0.050 g, 0.068 mmol) was dissolved in anhydrous MeOH (4 mL) and the solution degassed with argon before the addition of AcOH (0.20 mL, 3.5 mmol), paraformaldehyde (0.120 g, 4.00 mmol) and 10% Pd/C (0.040 g, 0.038 mmol). The resulting heterogeneous solution was enriched with H_2, by use of a balloon attached to the reaction vessel, and the reaction allowed to stir for 60 hours at rt. The reaction mixture was subsequently filtered through Celite, which was rinsed with MeOH (10 mL), and the resulting solution reduced *in vacuo* to yield auristatin-F as a colourless solid (0.050 g, 98%).

(*S*)-2-[(*S*)-2-(Dimethylamino)-3-methylbutanamido]-*N*-{(3*R*,4*S*,5*S*)-3-methoxy-1-[(*S*)-2-((1*R*,2*R*)-1-methoxy-2-methyl-3-oxo-3-{[(*S*)-1-oxo-3-phenyl-1-(prop-2-yn-1-ylamino)propan-2-yl]amino}propyl)pyrrolidin-1-yl]-5-methyl-1-oxoheptan-4-yl}-*N*,3-dimethylbutanamide (18)

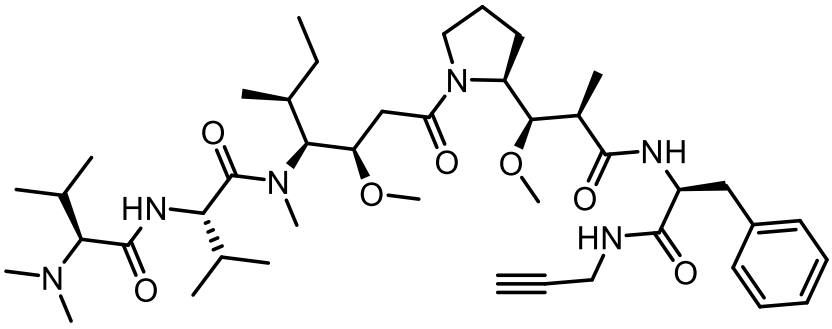

To a solution of auristatin-F (0.030 g, 0.040 mmol) and EDC (0.010 g, 0.052 mmol) in anhydrous DMF (0.5 mL), at 0 °C, was added propargylamine (0.008 mL, 0.1 mmol) and HOBt (0.001 g, 0.007 mmol) and the resulting solution warmed to 30 °C. The reaction was allowed to stir for 36 hours after which point the DMF was removed *in vacuo*. The residue adsorbed to silica, for purification by column chromatography (2-4% MeOH/DCM, elution gradient), to yield **18** as a colourless solid (0.018 g, 57%). HRMS (ES) *m/z*: $[M + H]^+$ Calcd for $C_{43}H_{71}N_6O_7$ 783.5384; Found 783.5384.

5.2.4 ADC-precursor Synthesis

4-{[(2-Amino-9*H*-purin-6-yl)oxy]methyl}-*N*-(3-{2-[2-(3-{4-[((*S*)-2-{(2*R*,3*R*)-3-[(*S*)-1-((3*R*,4*S*,5*S*)-4-{(*S*)-2-[(*S*)-2-(dimethylamino)-3-methylbutanamido]-*N*,3-dimethylbutanamido}-3-methoxy-5-methylheptanoyl)pyrrolidin-2-yl]-3-methoxy-2-methylpropanamido}-3-phenylpropanamido)methyl]-1*H*-1,2,3-triazol-1-yl}propoxy)ethoxy]ethoxy}propyl)benzamide (19)

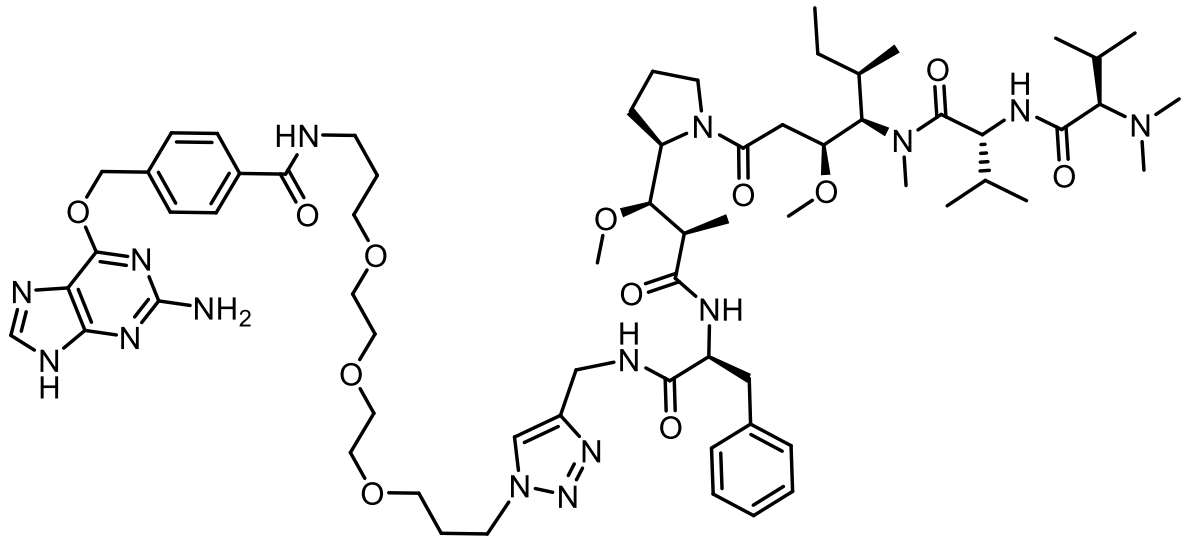

Compound **18** (0.018 g, 0.023 mmol) and compound **9** (0.011 g, 0.021 mmol) were dissolved in t-BuOH (0.5 mL) and allowed to stir. An aqueous solution (0.5 mL) of $Cu_2SO_4 \cdot 5H_2O$ (0.0015 g, 0.0060 mmol) and THPTA (0.003 g, 0.006 mmol) was prepared, which was allowed to complex for 5 minutes before being added to the t-BuOH solution. This was followed by the addition of sodium ascorbate (0.005 g, 0.03 mmol) and the resulting reaction allowed to stir for 60 hours before the solution was freeze dried and the residue purified directly by column chromatography (1-5% MeOH/DCM, elution gradient) to yield **19** as a colourless solid (0.0087 g, 31%). HRMS (ES) *m/z*: $[M + H]^+$ Calcd for $C_{66}H_{102}N_{15}O_{12}$ 1296.7832; Found 1296.7878.

4-{[(2-Amino-9*H*-purin-6-yl)oxy]methyl}-*N*-{1-[4-({5-(dimethylamino)-*N*-[5-((*S*)-2-{(2*R*,3*R*)-3-[(*R*)-1-((3*S*,4*R*,5*R*)-4-{(*R*)-2-[(*R*)-2-(dimethylamino)-3-methylbutanamido]-*N*,3-dimethylbutanamido}-3-methoxy-5-methylheptanoyl)pyrrolidin-2-yl]-3-methoxy-2-methylpropanamido}-3-phenylpropanamido)pentyl]naphthalene}-1-sulfonamido)phenyl]-1-oxo-6,9,12-trioxa-2-azapentadecan-15-yl}benzamide (20)

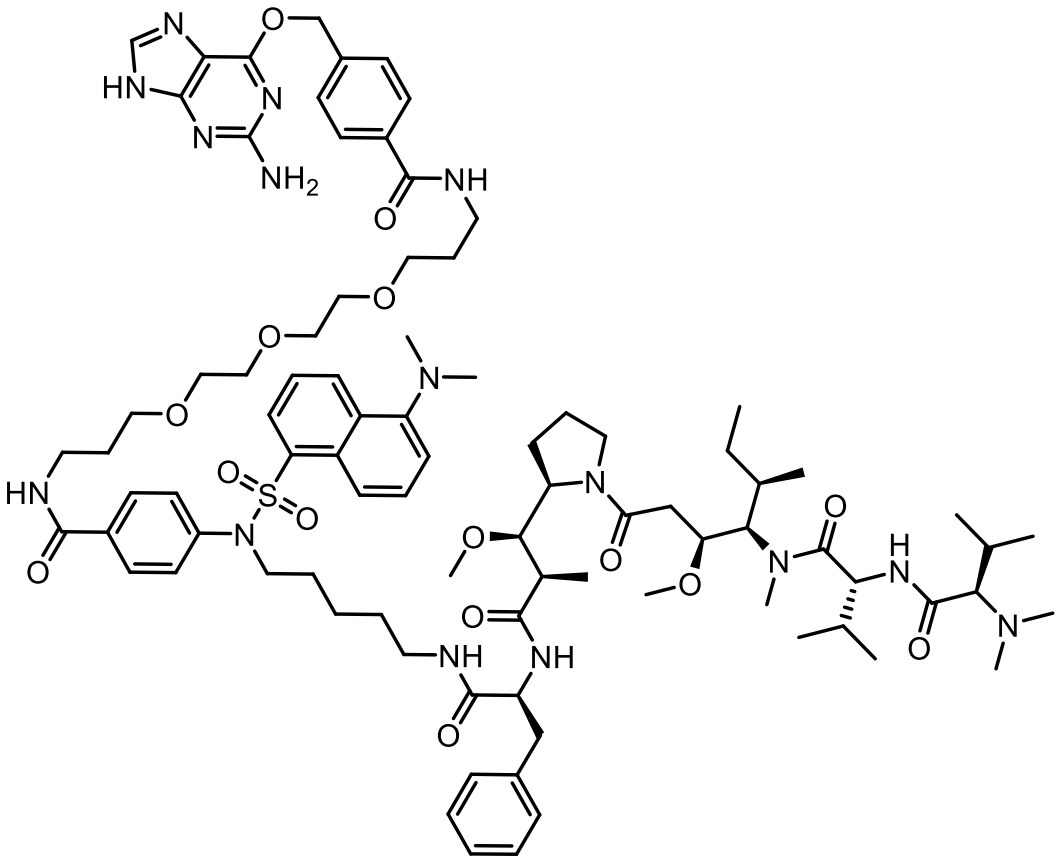

To a solution of auristatin-F (0.015 g, 0.020 mmol) and EDC (0.006 g, 0.03 mmol) in anhydrous DMF (0.4 mL) was added compound **17** (0.020 g, 0.022 mmol) and DMAP (0.001 g, 0.008 mmol), dissolved in anhydrous DMF (0.6 mL), and the reaction warmed to 30 °C. The reaction was allowed to stir for 36 hours after which point the DMF was removed *in vacuo* and the residue purified directly by column chromatography (1-5% MeOH/DCM, elution gradient) to yield **20** as a yellow solid (0.007 g, 21%). HRMS (ES) *m/z*: $[M + Na]^+$ Calcd for $C_{87}H_{125}N_{15}O_{15}SNa$ 1675.9093; Found 1675.9044.

Chapter Six: References

(1) Stiefel, M.; Shaner, A.; Schaefer, S. D. The Edwin Smith Papyrus: The Birth of Analytical Thinking in Medicine and Otolaryngology. *Laryngoscope* **2006**, *116* (2), 182–188.

(2) Hajdu, S. I. Greco-Roman Thought about Cancer. *Cancer* **2004**, *100* (10), 2048–2051.

(3) Hajdu, S. I.; Vadmal, M.; Tang, P. A Note from History: Landmarks in History of Cancer, Part 7. *Cancer* **2015**, *121* (15), 2480–2513.

(4) Jemal, A.; Bray, F.; Center, M. M.; Ferlay, J.; Ward, E.; Forman, D. Global Cancer Statistics. *Ca-Cancer J. Clin.* **2011**, *61* (2), 69–90.

(5) Ferlay, J.; Shin, H. R.; Bray, F.; Forman, D.; Mathers, C.; Parkin, D. M. Estimates of Worldwide Burden of Cancer in 2008: GLOBOCAN 2008. *Int. J. Cancer* **2010**, *127* (12), 2893–2917.

(6) Rahib, L.; Smith, B. D.; Aizenberg, R.; Rosenzweig, A. B.; Fleshman, J. M.; Matrisian, L. M. Projecting Cancer Incidence and Deaths to 2030: The Unexpected Burden of Thyroid, Liver, and Pancreas Cancers in the United States. *Cancer Res.* **2014**, *74* (11), 2913–2921.

(7) Jemal, A.; Center, M. M.; DeSantis, C.; Ward, E. M. Global Patterns of Cancer Incidence and Mortality Rates and Trends. *Cancer Epidemiol., Biomarkers Prev.* **2010**, *19* (8), 1893–1907.

(8) Thun, M. J.; DeLancey, J. O.; Center, M. M.; Jemal, A.; Ward, E. M. The Global Burden of Cancer: Priorities for Prevention. *Carcinogenesis* **2010**, *31* (1), 100–110.

(9) Doll, R.; Peto, R. The Causes of Cancer: Quantitative Estimates of Avoidable Risks of Cancer in the United States Today. *J. Natl. Cancer Inst.* **1981**, *66* (6), 1192–1308.

(10) Boffetta, P.; Jourenkova, N.; Gustavsson, P. Cancer Risk from Occupational and Environmental Exposure to Polycyclic Aromatic Hydrocarbons. *Cancer, Causes Control* **1997**, *8* (3), 444–472.

(11) Martin-Moreno, J. M.; Soerjomataram, I.; Magnusson, G. Cancer Causes and Prevention: A Condensed Appraisal in Europe in 2008. *Eur. J. Cancer* **2008**, *44* (10), 1390–1403.

(12) Robson, M. E.; Bradbury, A. R.; Arun, B.; Domchek, S. M.; Ford, J. M.; Hampel, H. L.; Lipkin, S. M.; Syngal, S.; Wollins, D. S.; Lindor, N. M. American Society of Clinical Oncology Policy Statement Update: Genetic and Genomic Testing for Cancer Susceptibility. *J. Clin. Oncol.* **2015**, *33* (31), 3660–3667.

(13) Olsen, J. H.; Andersen, A.; Dreyer, L.; Pukkala, E.; Tryggvadottir, L.; Verdier, M. G.; Winther, J. F. Summary of Avoidable Cancers in the Nordic Countries. *APMIS* **1997**, *105* (S76), 141–146.

(14) Parkin, D. M.; Pisani, P.; Lopez, A. D.; Masuyer, E. At Least One in Seven Cases of Cancer Is Caused by Smoking. Global Estimates for 1985. *Int. J. Cancer* **1994**, *59* (4), 494–504.

(15) Steinmetz, K. A.; Potter, J. D. Vegetables, Fruit, and Cancer. I. Epidemiology. *Cancer, Causes Control* **1991**, *2* (5), 325–357.

(16) Steinmetz, K. A.; Potter, J. D. Vegetables, Fruit, and Cancer. II. Mechanisms. *Cancer, Causes Control* **1991**, *2* (6), 427–442.

(17) Wolk, A.; Gridley, G.; Svensson, M.; Nyrén, O.; McLaughlin, J. K.; Fraumeni, J. F.; Adami, H. O. A Prospective Study of Obesity and Cancer Risk (Sweden). *Cancer, Causes Control* **2001**, *12*, 13–21.

(18) Moore, M. M.; Chua, W.; Charles, K. A.; Clarke, S. J. Inflammation and Cancer: Causes and Consequences. *Clin. Pharmacol. Ther.* **2010**, *87* (4), 504–508.

(19) Kumar, S.; Chan, C. J.; Coussens, L. M. Inflammation and Cancer. *Encyclopedia of Immunobiology*; Elsevier: Cambridge, 2016; Vol. 4, pp 406–415.

(20) Forbes, S. A.; Beare, D.; Boutselakis, H.; Bamford, S.; Bindal, N.; Tate, J.; Cole, C. G.; Ward, S.; Dawson, E.; Ponting, L.; Stefancsik, R.; Harsha, B.; Kok, C. Y.; Jia, M.; Jubb, H.; Sondka, Z.; Thompson, S.; De, T.; Campbell, P. J. COSMIC: Somatic Cancer Genetics at High-Resolution. *Nucleic Acids Res.* **2017**, *45* (1), 777–783.

(21) Cooper, G. M. Oncogenes. In *The cell: A molecular approach*; 2000; pp 713–723.

(22) Nasmyth, K. Viewpoint: Putting the Cell Cycle in Order. *Science* **1996**, *274* (5293), 1643–1645.

(23) Collins, I.; Garrett, M. D. Targeting the Cell Division Cycle in Cancer: CDK and Cell Cycle Checkpoint Kinase Inhibitors. *Curr. Opin. Pharmacol.* **2005**, *5* (4), 366–373.

(24) Morgan, D. O. Cyclin-Dependent Kinases: Engines, Clocks, and Microprocessors. *Annu. Rev. Cell Dev. Biol.* **1997**, *13* (1), 261–291.

(25) Elledge, S. J. Cell Cycle Checkpoints: Preventing an Identity Crisis. *Science* **1996**, *274* (5293), 1664–1672.

(26) Bartek, J.; Lukas, J. Chk1 and Chk2 Kinases in Checkpoint Control and Cancer. *Cancer Cell* **2003**, *3* (5), 421–429.

(27) Nyberg, K. A.; Michelson, R. J.; Putnam, C. W.; Weinert, T. A. Toward Maintaining

the Genome: DNA Damage and Replication Checkpoints. *Annu. Rev. Genet.* **2002**, *36* (1), 617–656.

(28) Kastan, M. B.; Lim, D. The Many Substrates and Functions of ATM. *Nat. Rev. Mol. Cell Biol.* **2000**, *1* (3), 179–186.

(29) Kastan, M. B.; Bartek, J. Cell-Cycle Checkpoints and Cancer. *Nature* **2004**, *432* (7015), 316–323.

(30) Gorbsky, G. J. The Spindle Checkpoint and Chromosome Segregation in Meiosis. *FEBS J.* **2015**, *282* (13), 2471–2487.

(31) Lane, D. P. P53, Guardian of the Genome. *Nature* **1992**, *358* (6381), 15–16.

(32) Vogelstein, B.; Lane, D.; Levine, A. J. Surfing the P53 Network. *Nature* **2000**, *408* (6810), 307–310.

(33) Cheung, T. H.; Rando, T. A. Molecular Regulation of Stem Cell Quiescence. *Nat. Rev. Mol. Cell Biol.* **2013**, *14* (6), 329–340.

(34) Roberts, P. J.; Der, C. J. Targeting the Raf-MEK-ERK Mitogen-Activated Protein Kinase Cascade for the Treatment of Cancer. *Oncogene* **2007**, *26* (22), 3291–3310.

(35) Hanahan, D.; Weinberg, R. A. Hallmarks of Cancer: The Next Generation. *Cell* **2011**, *144* (5), 646–674.

(36) Hajdu, S. I.; Darvishian, F. A Note from History: Landmarks in History of Cancer, Part 5. *Cancer* **2013**, *119* (8), 1450–1466.

(37) DeVita, V. T.; Chu, E. A History of Cancer Chemotherapy. *Cancer Res.* **2008**, *68* (21), 8643–8653.

(38) Freireich, E. J. History of Acute Leukemia. In *Neoplastic Diseases of the Blood*; Springer International Publishing: New York, NY, 2018; pp 155–159.

(39) Gehan, E. A.; Schneiderman, M. A. Historical and Methodological Developments in Clinical Trials at the National Cancer Institute. *Stat. Med.* **1990**, *9* (8), 871–880.

(40) Devita, V. T.; Canellos, G. P.; Moxley, J. H. A Decade of Combination Chemotherapy of Advanced Hodgkin's Disease. *Cancer* **1972**, *30* (6), 1495–1504.

(41) Gerber, D. E. Targeted Therapies: A New Generation of Cancer Treatments. *Am. Fam. Physician* **2008**, *77* (3), 311–319.

(42) McCubrey, J. A.; Steelman, L. S.; Chappell, W. H.; Abrams, S. L.; Wong, E. W. T.; Chang, F.; Lehmann, B.; Terrian, D. M.; Milella, M.; Tafuri, A.; Stivala, F.; Libra, M.; Basecke, J.; Evangelisti, C.; Martelli, A. M.; Franklin, R. A. Roles of the

Raf/MEK/ERK Pathway in Cell Growth, Malignant Transformation and Drug Resistance. *Biochim. Biophys. Acta, Mol. Cell Res.* **2007**, *1773* (8), 1263–1284.

(43) Santarpia, L.; Lippman, S. M.; El-Naggar, A. K. Targeting the MAPK–RAS–RAF Signaling Pathway in Cancer Therapy. *Expert Opin. Ther. Targets* **2012**, *16* (1), 103–119.

(44) Di Gennaro, E.; Barbarino, M.; Bruzzese, F.; De Lorenzo, S.; Caraglia, M.; Abbruzzese, A.; Avallone, A.; Comella, P.; Caponigro, F.; Pepe, S.; Budillon, A. Critical Role of Both P27KIP1 and P21CIP1/WAF1 in the Antiproliferative Effect of ZD1839 ('Iressa'), an Epidermal Growth Factor Receptor Tyrosine Kinase Inhibitor, in Head and Neck Squamous Carcinoma Cells. *J. Cell. Physiol.* **2003**, *195* (1), 139–150.

(45) Wyatt, P. G.; Woodhead, A. J.; Berdini, V.; Boulstridge, J. A.; Carr, M. G.; Cross, D. M.; Davis, D. J.; Devine, L. A.; Early, T. R.; Feltell, R. E.; Lewis, E. J.; McMenamin, R. L.; Navarro, E. F.; O'Brien, M. A.; O'Reilly, M.; Reule, M.; Saxty, G.; Seavers, L. C. A.; Smith, D. M.; Squires, M. S.; Trewartha, G.; Walker, M. T.; Woolford, A. J. A. Identification of N-(4-Piperidinyl)-4-(2,6-Dichlorobenzoylamino)-1H-Pyrazole-3-Carboxamide (AT7519), a Novel Cyclin Dependent Kinase Inhibitor Using Fragment-Based X-Ray Crystallography and Structure Based Drug Design. *J. Med. Chem.* **2008**, *51* (16), 4986–4999.

(46) Shi, D.; Gu, W. Dual Roles of MDM2 in the Regulation of P53: Ubiquitination Dependent and Ubiquitination Independent Mechanisms of MDM2 Repression of P53 Activity. *Genes Cancer* **2012**, *3* (3–4), 240–248.

(47) Vassilev, L. T. MDM2 Inhibitors for Cancer Therapy. *Trends Mol. Med.* **2007**, *13* (1), 23–31.

(48) Jordan, V. C. Tamoxifen (ICI46,474) as a Targeted Therapy to Treat and Prevent Breast Cancer. *Br. J. Pharmacol.* **2009**, *147* (S1), 269–276.

(49) Plati, J.; Bucur, O.; Khosravi-Far, R. Apoptotic Cell Signaling in Cancer Progression and Therapy. *Integr. Biol.* **2011**, *3* (4), 279–296.

(50) Strome, S. E.; Sausville, E. A.; Mann, D. A Mechanistic Perspective of Monoclonal Antibodies in Cancer Therapy Beyond Target-Related Effects. *Oncologist* **2007**, *12* (9), 1084–1095.

(51) Scott, A. M.; Wolchok, J. D.; Old, L. J. Antibody Therapy of Cancer. *Nat. Rev. Cancer* **2012**, *12* (4), 278–287.

(52) Cohen, P. Protein Kinases - The Major Drug Targets of the Twenty-First Century? *Nat. Rev. Drug Discovery* **2002**, *1* (4), 309–315.

(53) Hodi, F. S.; O'Day, S. J.; McDermott, D. F.; Weber, R. W.; Sosman, J. A.; Haanen, J. B.; Gonzalez, R.; Robert, C.; Schadendorf, D.; Hassel, J. C.; Akerley, W.; van den

Eertwegh, A. J. M.; Lutzky, J.; Lorigan, P.; Vaubel, J. M.; Linette, G. P.; Hogg, D.; Ottensmeier, C. H.; Lebbé, C.; Peschel, C.; Quirt, I.; Clark, J. I.; Wolchok, J. D.; Weber, J. S.; Tian, J.; Yellin, M. J.; Nichol, G. M.; Hoos, A.; Urba, W. J. Improved Survival with Ipilimumab in Patients with Metastatic Melanoma. *N. Engl. J. Med.* **2010**, *363* (8), 711–723.

(54) Boross, P.; Leusen, J. H. W. Mechanisms of Action of CD20 Antibodies. *Am. J. Cancer Res.* **2012**, *2* (6), 676–690.

(55) Plosker, G. L.; Figgitt, D. P. Rituximab. *Drugs* **2003**, *63* (8), 803–843.

(56) Ulahannan, S. VEGF. In *Cancer Therapeutic Targets*; Springer International Publishing: New York, NY, 2017; Vol. 1–2, pp 537–543.

(57) Buss, N. A. P. S.; Henderson, S. J.; McFarlane, M.; Shenton, J. M.; de Haan, L. Monoclonal Antibody Therapeutics: History and Future. *Curr. Opin. Pharmacol.* **2012**, *12* (5), 615–622.

(58) Morrison, S. L.; Johnson, M. J.; Herzenberg, L. A.; Oi, V. T. Chimeric Human Antibody Molecules: Mouse Antigen-Binding Domains with Human Constant Region Domains. *Proc. Natl. Acad. Sci. U. S. A.* **1984**, *81* (21 I), 6851–6855.

(59) Ghose, T.; Path, M. R. C.; Nigam, S. P. Antibody as Carrier of Chlorambucil. *Cancer* **1972**, *29* (5), 1398–1400.

(60) Panousis, C.; Pietersz, G. A. Monoclonal Antibody-Directed Cytotoxic Therapy. *Drugs Aging* **1999**, *15* (1), 1–13.

(61) Perez, H. L.; Cardarelli, P. M.; Deshpande, S.; Gangwar, S.; Schroeder, G. M.; Vite, G. D.; Borzilleri, R. M. Antibody–Drug Conjugates: Current Status and Future Directions. *Drug Discovery Today* **2014**, *19* (7), 869–881.

(62) Senter, P. D. Potent Antibody Drug Conjugates for Cancer Therapy. *Curr. Opin. Chem. Biol.* **2009**, *13* (3), 235–244.

(63) Lu, J.; Jiang, F.; Lu, A.; Zhang, G. Linkers Having a Crucial Role in Antibody–Drug Conjugates. *Int. J. Mol. Sci.* **2016**, *17* (4), 561–583.

(64) Diamantis, N.; Banerji, U. Antibody-Drug Conjugates—an Emerging Class of Cancer Treatment. *Br. J. Cancer* **2016**, *114* (4), 362–367.

(65) Kamath, A. V.; Iyer, S. Preclinical Pharmacokinetic Considerations for the Development of Antibody Drug Conjugates. *Pharm. Res.* **2015**, *32* (11), 3470–3479.

(66) Khazaeli, M. B.; Conry, R. M.; LoBuglio, A. F. Human Immune Respone to Monoclonal Antibodies. *J. Immunother.* **1994**, *15* (1), 42–52.

(67) Lippow, S. M.; Wittrup, K. D.; Tidor, B. Computational Design of Antibody-

Affinity Improvement beyond in Vivo Maturation. *Nat. Biotechnol.* **2007**, *25* (10), 1171–1176.

(68) Deonarain, M.; Yahioglu, G.; Stamati, I.; Pomowski, A.; Clarke, J.; Edwards, B.; Diez-Posada, S.; Stewart, A. Small-Format Drug Conjugates: A Viable Alternative to ADCs for Solid Tumours? *Antibodies* **2018**, *7* (2), 16–34.

(69) Richards, D. A. Exploring Alternative Antibody Scaffolds: Antibody Fragments and Antibody Mimics for Targeted Drug Delivery. *Drug Discovery Today Technol.* **2018**, *30*, 35–46.

(70) Kijanka, M.; Dorresteijn, B.; Oliveira, S.; van Bergen en Henegouwen, P. M. Nanobody-Based Cancer Therapy of Solid Tumors. *Nanomedicine* **2015**, *10* (1), 161–174.

(71) Ahmad, Z. A.; Yeap, S. K.; Ali, A. M.; Ho, W. Y.; Alitheen, N. B. M.; Hamid, M. ScFv Antibody: Principles and Clinical Application. *Clin. Dev. Immunol.* **2012**, *2012*, 1–15.

(72) Hinman, L. M.; Hamann, P. R.; Wallace, R.; Menendez, A. T.; Durr, F. E.; Upeslacis, J. Preparation and Characterization of Monoclonal Antibody Conjugates of the Calicheamicins: A Novel and Potent Family of Antitumor Antibiotics. *Cancer Res.* **1993**, *53* (14), 3336–3342.

(73) Walker, S.; Landovitz, R.; Wei Dong Ding; Ellestad, G. A.; Kahne, D. Cleavage Behavior of Calicheamicin Gamma 1 and Calicheamicin T. *Proc. Natl. Acad. Sci. U. S. A.* **1992**, *89* (10), 4608–4612.

(74) Elgersma, R. C.; Coumans, R. G. E.; Huijbregts, T.; Menge, W. M. P. B.; Joosten, J. A. F.; Spijker, H. J.; de Groot, F. M. H.; van der Lee, M. M. C.; Ubink, R.; van den Dobbelsteen, D. J.; Egging, D. F.; Dokter, W. H. A.; Verheijden, G. F. M.; Lemmens, J. M.; Timmers, C. M.; Beusker, P. H. Design, Synthesis, and Evaluation of Linker-Duocarmycin Payloads: Toward Selection of HER2-Targeting Antibody–Drug Conjugate SYD985. *Mol. Pharm.* **2015**, *12* (6), 1813–1835.

(75) Boger, D. L.; Johnson, D. S. CC-1065 and the Duocarmycins: Unraveling the Keys to a New Class of Naturally Derived DNA Alkylating Agents. *Proc. Natl. Acad. Sci. U. S. A.* **1995**, *92* (9), 3642–3649.

(76) Ghosh, N.; Sheldrake, H.; Searcey, M.; Pors, K. Chemical and Biological Explorations of the Family of CC-1065 and the Duocarmycin Natural Products. *Curr. Top. Med. Chem.* **2009**, *9* (16), 1494–1524.

(77) Gewirtz, D. A Critical Evaluation of the Mechanisms of Action Proposed for the Antitumor Effects of the Anthracycline Antibiotics Adriamycin and Daunorubicin. *Biochem. Pharmacol.* **1999**, *57* (7), 727–741.

(78) Parker, A. L.; Kavallaris, M.; McCarroll, J. A. Microtubules and Their Role in Cellular Stress in Cancer. *Front. Oncol.* **2014**, *4*, 153.

(79) Drechsel, D. N.; Kirschner, M. W. The Minimum GTP Cap Required to Stabilize Microtubules. *Curr. Biol.* **1994**, *4* (12), 1053–1061.

(80) Dumontet, C.; Jordan, M. A. Microtubule-Binding Agents: A Dynamic Field of Cancer Therapeutics. *Nat. Rev. Drug Discovery* **2010**, *9* (10), 790–803.

(81) Hamel, E. Natural Products Which Interact with Tubulin in the Vinca Domain: Maytansine, Rhizoxin, Phomopsin a, Dolastatins 10 and 15 and Halichondrin B. *Pharmacol. Ther.* **1992**, *55* (1), 31–51.

(82) Pettit, G. R.; Kamano, Y.; Herald, C. L.; Tuinman, A. A.; Boettner, F. E.; Kizu, H.; Schmidt, J. M.; Baczynskyj, L.; Tomer, K. B.; Bontems, R. J. The Isolation and Structure of a Remarkable Marine Animal Antineoplastic Constituent: Dolastatin 10. *J. Am. Chem. Soc.* **1987**, *109* (22), 6883–6885.

(83) Maderna, A.; Leverett, C. A. Recent Advances in the Development of New Auristatins: Structural Modifications and Application in Antibody Drug Conjugates. *Mol. Pharm.* **2015**, *12* (6), 1798–1812.

(84) Miyazaki, K.; Kobayashi, M.; Natsume, T.; Gondo, M.; Mikami, T.; Sakakibara, K.; Tsukagoshi, S. Synthesis and Antitumor Activity of Novel Dolastatin 10 Analogs. *Chem. Pharm. Bull.* **1995**, *43* (10), 1706–1718.

(85) Doronina, S. O.; Toki, B. E.; Torgov, M. Y.; Mendelsohn, B. A.; Cerveny, C. G.; Chace, D. F.; DeBlanc, R. L.; Gearing, R. P.; Bovee, T. D.; Siegall, C. B.; Francisco, J. A.; Wahl, A. F.; Meyer, D. L.; Senter, P. D. Development of Potent Monoclonal Antibody Auristatin Conjugates for Cancer Therapy. *Nat. Biotechnol.* **2003**, *21* (7), 778–784.

(86) Chari, R. V. J.; Miller, M. L.; Widdison, W. C. Antibody-Drug Conjugates: An Emerging Concept in Cancer Therapy. *Angew. Chem., Int. Ed.* **2014**, *53* (15), 3796–3827.

(87) Singh, R.; Erickson, H. K. Antibody-Cytotoxic Agent Conjugates: Preparation and Characterization. In *Methods in molecular biology*; Humana Press: New Jersey, 2009; Vol. 525, pp 445–467.

(88) Doronina, S. O.; Mendelsohn, B. A.; Bovee, T. D.; Cerveny, C. G.; Alley, S. C.; Meyer, D. L.; Oflazoglu, E.; Toki, B. E.; Sanderson, R. J.; Zabinski, R. F.; Wahl, A. F.; Senter, P. D. Enhanced Activity of Monomethylauristatin F through Monoclonal Antibody Delivery: Effects of Linker Technology on Efficacy and Toxicity. *Bioconjug. Chem.* **2006**, *17* (1), 114–124.

(89) Jain, N.; Smith, S. W.; Ghone, S.; Tomczuk, B. Current ADC Linker Chemistry. *Pharm. Res.* **2015**, *32* (11), 3526–3540.

(90) Tsuchikama, K.; An, Z. Antibody-Drug Conjugates: Recent Advances in Conjugation and Linker Chemistries. *Protein Cell* **2018**, *9* (1), 33–46.

(91) Sapra, P.; Hooper, A. T.; O'Donnell, C. J.; Gerber, H. P. Investigational Antibody Drug Conjugates for Solid Tumors. *Expert Opin. Invest. Drugs* **2011**, *20* (8), 1131–1149.

(92) Dubowchik, G. M.; Firestone, R. A.; Padilla, L.; Willner, D.; Hofstead, S. J.; Mosure, K.; Knipe, J. O.; Lasch, S. J.; Trail, P. A. Cathepsin B-Labile Dipeptide Linkers for Lysosomal Release of Doxorubicin from Internalizing Immunoconjugates: Model Studies of Enzymatic Drug Release and Antigen-Specific In Vitro Anticancer Activity. *Bioconjug. Chem.* **2002**, *13* (4), 855–869.

(93) Nolting, B. Linker Technologies for Antibody–Drug Conjugates. In *Methods in Molecular Biology*, Humana Press: New Jersey, 2013; Vol. 1045, pp 71–100.

(94) Erickson, H. K.; Park, P. U.; Widdison, W. C.; Kovtun, Y. V.; Garrett, L. M.; Hoffman, K.; Lutz, R. J.; Goldmacher, V. S.; Blättler, W. A. Antibody-Maytansinoid Conjugates Are Activated in Targeted Cancer Cells by Lysosomal Degradation and Linker-Dependent Intracellular Processing. *Cancer Res.* **2006**, *66* (8), 4426–4433.

(95) Erickson, H. K.; Lewis Phillips, G. D.; Leipold, D. D.; Provenzano, C. A.; Mai, E.; Johnson, H. A.; Gunter, B.; Audette, C. A.; Gupta, M.; Pinkas, J.; Tibbitts, J. The Effect of Different Linkers on Target Cell Catabolism and Pharmacokinetics/Pharmacodynamics of Trastuzumab Maytansinoid Conjugates. *Mol. Cancer Ther.* **2012**, *11* (5), 1133–1142.

(96) Bouchard, H.; Viskov, C.; Garcia-Echeverria, C. Antibody–Drug Conjugates—A New Wave of Cancer Drugs. *Bioorg. Med. Chem. Lett.* **2014**, *24* (23), 5357–5363.

(97) Ramchandren, R. Advances in the Treatment of Relapsed or Refractory Hodgkin's Lymphoma. *Oncologist* **2012**, *17* (3), 367–376.

(98) Lambert, J. M.; Morris, C. Q. Antibody–Drug Conjugates (ADCs) for Personalized Treatment of Solid Tumors: A Review. *Adv. Ther.* **2017**, *34* (5), 1015–1035.

(99) Mukherjee, A.; Waters, A. K.; Babic, I.; Nurmemmedov, E.; Glassy, M. C.; Kesari, S.; Yenugonda, V. M. Antibody Drug Conjugates: Progress, Pitfalls, and Promises. *Hum. Antibodies* **2018**, *27* (1), 53–62.

(100) Senter, P. D.; Sievers, E. L. The Discovery and Development of Brentuximab Vedotin for Use in Relapsed Hodgkin Lymphoma and Systemic Anaplastic Large Cell Lymphoma. *Nat. Biotechnol.* **2012**, *30* (7), 631–637.

(101) Girish, S.; Gupta, M.; Wang, B.; Lu, D.; Krop, I. E.; Vogel, C. L.; Burris III, H. A.; LoRusso, P. M.; Yi, J.-H.; Saad, O.; Tong, B.; Chu, Y.-W.; Holden, S.; Joshi, A.

Clinical Pharmacology of Trastuzumab Emtansine (T-DM1): An Antibody–Drug Conjugate in Development for the Treatment of HER2-Positive Cancer. *Cancer Chemother. Pharmacol.* **2012**, *69* (5), 1229–1240.

(102) Widdison, W. C.; Wilhelm, S. D.; Cavanagh, E. E.; Whiteman, K. R.; Leece, B. A.; Kovtun, Y.; Goldmacher, V. S.; Xie, H.; Steeves, R. M.; Lutz, R. J.; Zhao, R.; Wang, L.; Blättler, W. A.; Chari, R. V. J. Semisynthetic Maytansine Analogues for the Targeted Treatment of Cancer. *J. Med. Chem.* **2006**, *49* (14), 4392–4408.

(103) Leung, D.; Wurst, J. M.; Liu, T.; Martinez, R. M.; Datta-Mannan, A.; Feng, Y. Antibody Conjugates-Recent Advances and Future Innovations. *Antibodies* **2020**, *9* (1), 2–28.

(104) Chau, C. H.; Steeg, P. S.; Figg, W. D. Antibody–Drug Conjugates for Cancer. *Lancet* **2019**, *394* (10200), 793–804.

(105) Lanieri, L.; Boule, S.; Dong, L.; Drake, T.; Laleau, R.; Lee, J.; Liu, F.; Qiu, Q.; Kohli, N.; Ponte, J.; Setiady, Y.; Gregory, R. Abstract 753: Development of an in Vivo Model System to Assess the Interplay between the Various Drivers of Antibody-Drug Conjugate (ADC) Activity. In *Experimental and Molecular Therapeutics*; American Association for Cancer Research: Chicago, 2018; pp 753–753.

(106) Junutula, J. R.; Raab, H.; Clark, S.; Bhakta, S.; Leipold, D. D.; Weir, S.; Chen, Y.; Simpson, M.; Tsai, S. P.; Dennis, M. S.; Lu, Y.; Meng, Y. G.; Ng, C.; Yang, J.; Lee, C. C.; Duenas, E.; Gorrell, J.; Katta, V.; Kim, A.; McDorman, K.; Flagella, K.; Venook, R.; Ross, S.; Spencer, S. D.; Lee Wong, W.; Lowman, H. B.; Vandlen, R.; Sliwkowski, M. X.; Scheller, R. H.; Polakis, P.; Mallet, W. Site-Specific Conjugation of a Cytotoxic Drug to an Antibody Improves the Therapeutic Index. *Nat. Biotechnol.* **2008**, *26* (8), 925–932.

(107) Behrens, C. R.; Liu, B. Methods for Site-Specific Drug Conjugation to Antibodies. *MAbs* **2014**, *6* (1), 46–53.

(108) Dennler, P.; Chiotellis, A.; Fischer, E.; Brégeon, D.; Belmant, C.; Gauthier, L.; Lhospice, F.; Romagne, F.; Schibli, R. Transglutaminase-Based Chemo-Enzymatic Conjugation Approach Yields Homogeneous Antibody–Drug Conjugates. *Bioconjugate Chem.* **2014**, *25* (3), 569–578.

(109) Damoiseaux, R.; Keppler, A.; Johnsson, K. Synthesis and Applications of Chemical Probes for Human O6-Alkylguanine-DNA Alkyltransferase. *ChemBioChem* **2001**, *2* (4), 285–287.

(110) Pegg, A. E. Repair of O6-Alkylguanine by Alkyltransferases. *Mutat. Res., Rev. Mutat. Res.* **2000**, *462* (2–3), 83–100.

(111) Juillerat, A.; Gronemeyer, T.; Keppler, A.; Gendreizig, S.; Pick, H.; Vogel, H.;

Johnsson, K. Directed Evolution of O6-Alkylguanine-DNA Alkyltransferase for Efficient Labeling of Fusion Proteins with Small Molecules In Vivo. *Chem. Biol.* **2003**, *10* (4), 313–317.

(112) Mollwitz, B.; Brunk, E.; Schmitt, S.; Pojer, F.; Bannwarth, M.; Schiltz, M.; Rothlisberger, U.; Johnsson, K. Directed Evolution of the Suicide Protein O6-Alkylguanine-DNA Alkyltransferase for Increased Reactivity Results in an Alkylated Protein with Exceptional Stability. *Biochemistry* **2012**, *51* (5), 986–994.

(113) Crivat, G.; Taraska, J. W. Imaging Proteins inside Cells with Fluorescent Tags. *Trends Biotechnol.* **2012**, *30* (1), 8–16.

(114) Bodor, D. L.; Rodríguez, M. G.; Moreno, N.; Jansen, L. E. T. Analysis of Protein Turnover by Quantitative SNAP-Based Pulse-Chase Imaging. *Curr. Protoc. Cell Biol.* **2012**, *55* (1), 1–34.

(115) Chidley, C.; Haruki, H.; Pedersen, M. G.; Muller, E.; Johnsson, K. A Yeast-Based Screen Reveals That Sulfasalazine Inhibits Tetrahydrobiopterin Biosynthesis. *Nat. Chem. Biol.* **2011**, *7* (6), 375–383.

(116) Hussain, A.; Amoury, M.; Barth, S. SNAP-Tag Technology: A Powerful Tool for Site Specific Conjugation of Therapeutic and Imaging Agents. *Curr. Pharm. Des.* **2013**, *19* (30), 5437–5442.

(117) Woitok, M.; Klose, D.; Niesen, J.; Richter, W.; Abbas, M.; Stein, C.; Fendel, R.; Bialon, M.; Püttmann, C.; Fischer, R.; Barth, S.; Kolberg, K. The Efficient Elimination of Solid Tumor Cells by EGFR-Specific and HER2-Specific ScFv-SNAP Fusion Proteins Conjugated to Benzylguanine-Modified Auristatin F. *Cancer Lett.* **2016**, *381* (2), 323–330.

(118) Woitok, M.; Klose, D.; Di Fiore, S.; Richter, W.; Stein, C.; Gresch, G.; Grieger, E.; Barth, S.; Fischer, R.; Kolberg, K.; Niesen, J. Comparison of a Mouse and a Novel Human ScFv-SNAP-Auristatin F Drug Conjugate with Potent Activity against EGFR-Overexpressing Human Solid Tumor Cells. *OncoTargets Ther.* **2017**, *10*, 3313–3327.

(119) Padayachee, E. R.; Adeola, H. A.; Van Wyk, J. C.; Nsole Biteghe, F. A.; Chetty, S.; Khumalo, N. P.; Barth, S. Applications of SNAP-Tag Technology in Skin Cancer Therapy. *Health Sci. Rep.* **2019**, *2* (2), 103–111.

(120) von Felbert, V.; Bauerschlag, D.; Maass, N.; Bräutigam, K.; Meinhold-Heerlein, I.; Woitok, M.; Barth, S.; Hussain, A. F. A Specific Photoimmunotheranostics Agent to Detect and Eliminate Skin Cancer Cells Expressing EGFR. *J. Cancer Res. Clin. Oncol.* **2016**, *142* (5), 1003–1011.

(121) Padayachee, E. R.; Biteghe, F. A. N.; Malindi, Z.; Bauerschlag, D.; Barth, S. Human Antibody Fusion Proteins/Antibody Drug Conjugates in Breast and Ovarian

Cancer. *Transfus. Med. Hemotherapy* **2017**, *44* (5), 303–310.

(122) Hussain, A. F.; Kampmeier, F.; von Felbert, V.; Merk, H.-F.; Tur, M. K.; Barth, S. SNAP-Tag Technology Mediates Site Specific Conjugation of Antibody Fragments with a Photosensitizer and Improves Target Specific Phototoxicity in Tumor Cells. *Bioconjug. Chem.* **2011**, *22* (12), 2487–2495.

(123) Knowles, D. B.; Shkel, I. A.; Phan, N. M.; Sternke, M.; Lingeman, E.; Cheng, X.; Cheng, L.; O'Connor, K.; Record, M. T. Chemical Interactions of Polyethylene Glycols (PEGs) and Glycerol with Protein Functional Groups: Applications to Effects of PEG and Glycerol on Protein Processes. *Biochemistry* **2015**, *54* (22), 3528–3542.

(124) Kolb, H. C.; Sharpless, K. B. The Growing Impact of Click Chemistry on Drug Discovery. *Drug Discovery Today* **2003**, *8* (24), 1128–1137.

(125) Moses, J. E.; Moorhouse, A. D. The Growing Applications of Click Chemistry. *Chem. Soc. Rev.* **2007**, *36* (8), 1249–1262.

(126) Rostovtsev, V. V.; Green, L. G.; Fokin, V. V.; Sharpless, K. B. A Stepwise Huisgen Cycloaddition Process: Copper(I)-Catalyzed Regioselective "Ligation" of Azides and Terminal Alkynes. *Angew. Chem., Int. Ed.* **2002**, *41* (14), 2596–2599.

(127) Liang, L.; Astruc, D. The Copper(I)-Catalyzed Alkyne-Azide Cycloaddition (CuAAC) "Click" Reaction and Its Applications. An Overview. *Coord. Chem. Rev.* **2011**, *255* (23–24), 2933–2945.

(128) Ohta, Y.; Kamijyo, Y.; Fujii, S.; Yokoyama, A.; Yokozawa, T. Synthesis and Properties of a Variety of Well-Defined Hyperbranched N-Alkyl and N-H Polyamides by Chain-Growth Condensation Polymerization of AB 2 Monomers. *Macromolecules* **2011**, *44* (13), 5112–5122.

(129) Smith, M.; Moffatt, J. G.; Khorana, H. G. Carbodiimides. VIII. Observations on the Reactions of Carbodiimides with Acids and Some New Applications in the Synthesis of Phosphoric Acid Esters. *J. Am. Chem. Soc.* **1958**, *80* (23), 6204–6212.

(130) Wang, T.; Wu, Y.; Kuan, S. L.; Dumele, O.; Lamla, M.; Ng, D. Y. W.; Arzt, M.; Thomas, J.; Mueller, J. O.; Barner-Kowollik, C.; Weil, T. A Disulfide Intercalator Toolbox for the Site-Directed Modification of Polypeptides. *Chem. - Eur. J.* **2015**, *21* (1), 228–238.

(131) Titz, A.; Radic, Z.; Schwardt, O.; Ernst, B. A Safe and Convenient Method for the Preparation of Triflyl Azide, and Its Use in Diazo Transfer Reactions to Primary Amines. *Tetrahedron Lett.* **2006**, *47* (14), 2383–2385.

(132) Nyffeler, P. T.; Liang, C.-H.; Koeller, K. M.; Wong, C.-H. The Chemistry of Amine−Azide Interconversion: Catalytic Diazotransfer and Regioselective Azide

Reduction. *J. Am. Chem. Soc.* **2002**, *124* (36), 10773–10778.

(133) Cegielska, B.; Kacprzak, K. M. Simple and Convenient Protocol for Staining of Organic Azides on TLC Plates by Ninhydrin. A New Application of an Old Reagent. *Chem. Anal.* **2009**, *54* (4), 807–812.

(134) Kindermann, M.; George, N.; Johnsson, N.; Johnsson, K. Covalent and Selective Immobilization of Fusion Proteins. *J. Am. Chem. Soc.* **2003**, *125* (26), 7810–7811.

(135) Johansson, M. P.; Maaheimo, H.; Ekholm, F. S. New Insight on the Structural Features of the Cytotoxic Auristatins MMAE and MMAF Revealed by Combined NMR Spectroscopy and Quantum Chemical Modelling. *Sci. Rep.* **2017**, *7* (1), 15920–15929.

(136) Hong, V.; Presolski, S. I.; Ma, C.; Finn, M. â. G. Analysis and Optimization of Copper-Catalyzed Azide-Alkyne Cycloaddition for Bioconjugation. *Angew. Chem., Int. Ed.* **2009**, *48* (52), 9879–9883.

(137) Nudelman, A.; Bechor, Y.; Falb, E.; Fischer, B.; Wexler, B. A.; Nudelman, A. Acetyl Chloride-Methanol as a Convenient Reagent for: A) Quantitative Formation of Amine Hydrochlorides B) Carboxylate Ester Formation C) Mild Removal of N-t-Boc-Protective Group. *Synth. Commun.* **1998**, *28* (3), 471–474.

(138) Hinsberger, S.; de Jong, J. C.; Groh, M.; Haupenthal, J.; Hartmann, R. W. Benzamidobenzoic Acids as Potent PqsD Inhibitors for the Treatment of Pseudomonas Aeruginosa Infections. *Eur. J. Med. Chem.* **2014**, *76*, 343–351.

(139) Arifuzzaman, M.; Zhao, Y. Water-Soluble Molecularly Imprinted Nanoparticle Receptors with Hydrogen-Bond-Assisted Hydrophobic Binding. *J. Org. Chem.* **2016**, *81* (17), 7518–7526.

(140) Mushtaq, S.; Jeon, J.; Kang, J. A.; Nam, Y. R.; Jang, B. S.; Park, S. H. Radiosynthesis and Preliminary Biological Evaluation of 99mTc-Labeled 2-Methyl-2-Pentylmalonic Acid as an Apoptosis Imaging Agent. *J. Radioanal. Nucl. Chem.* **2017**, *313* (1), 207–215.

(141) Hughes, D. L. Progress in the Mitsunobu Reaction. A Review. *Org. Prep. Proced. Int.* **1996**, *28* (2), 127–164.

(142) Meguro, T.; Yoshida, S.; Hosoya, T. Aromatic Azido-Selective Reduction via the Staudinger Reaction Using Tri- n -Butylphosphonium Tetrafluoroborate with Triethylamine. *Chem. Lett.* **2017**, *46* (4), 473–476.

(143) Tjernberg, A.; Markova, N.; Griffiths, W. J.; Hallén, D. DMSO-Related Effects in Protein Characterization. *J. Biomol. Screening* **2006**, *11* (2), 131–137.

(144) Arakawa, T.; Kita, Y.; Timasheff, S. N. Protein Precipitation and Denaturation by

Dimethyl Sulfoxide. *Biophys. Chem.* **2007**, *131* (1–3), 62–70.

(145) Burg, M. B.; Ferraris, J. D. Intracellular Organic Osmolytes: Function and Regulation. *J. Biol. Chem.* **2008**, *283* (12), 7309–7313.

(146) Timasheff, S. N. Protein-Solvent Preferential Interactions, Protein Hydration, and the Modulation of Biochemical Reactions by Solvent Components. *Proc. Natl. Acad. Sci. U. S. A.* **2002**, *99* (15), 9721–9726.